PLATFORMS AND MOLECULAR MECHANISMS FOR IMPROVING SIGNAL TRANSDUCTION AND SIGNAL ENHANCEMENT IN MULTI-STEP POINT-OF-CARE DIAGNOSTICS

by

Kaleb Miles Byers

A Dissertation

Submitted to the Faculty of Purdue University

In Partial Fulfillment of the Requirements for the degree of

Doctor of Philosophy

Weldon School of Biomedical Engineering

West Lafayette, Indiana

August 2021

THE PURDUE UNIVERSITY GRADUATE SCHOOL

STATEMENT OF COMMITTEE APPROVAL

Dr. Jaqueline C. Linnes, Chair

Weldon School of Biomedical Engineering

Dr. Luis Solorio

Weldon School of Biomedical Engineering

Dr. Ramses Martinez

Weldon School of Biomedical Engineering

Dr. HyunDae Cho

Crosslife Technologies Inc., CEO

Approved by:

Dr. Andrew O. Brightman

Dedicated to…

My parents, for their unwavering support and encouragement; and my late grandfather Jimmy Frank Byers whose legacy I am proud to continue as a scientist and engineer.

&

To those whose circumstances did not lift them above the advantages they deserved, for any persistent and free-thinking student should be given the many resources and chances needed to reach the end of this climb.

ACKNOWLEDGMENTS

This work would not have been possible without the support of my committee, the many brilliant scientists in the Linnes Lab and our collaborators. Resources and funding generously provided by the NSF Small Business Innovation Research (SBIR) (Grant 1720900), Purdue Global Engineering's Innovation for International Development (I2D) Lab, Purdue Institute for Inflammation, Immunology and Infectious Disease (PI4D), Bill and Melinda Gates Grand Challenges Explorations program grant OPP1150806, Birck Nanotechnology Center, Purdue University's Women in Engineering Program (WIEP), the Purdue College of Engineering (Ross Fellowship) and the Weldon School were all key to the success of these projects as well as the travel opportunities I was afforded to showcase my work at several conferences. The Weldon School administration has also been extremely supportive and encouraging, and I credit the staff's culture and competence in BME with making this journey habitable. I cannot express the gratitude I feel for the endless support Dr. Jacqueline Linnes provided from the moment I accepted her offer to join the lab. She is keenly aware that pursuing a PhD is a transformative experience in both intellectual and emotional dexterity; and she applies a great deal of compassion towards her students while supplying resources for us to self-manage many obstacles. While this final year has been uniquely isolating due to the COVID-19 pandemic, I previously enjoyed a deep sense of comradery with my roommates, lab mates, and other BME students. Special acknowledgments to Elizabeth Phillips, Carmen Gondhalekar, Rachel Morrison, Andrea Acuña, Divya Tankasala, Taylor Moehling, and Kelsey Bayer – thank you for laughing and lamenting with me through our research woes. Thank you to my parents, Margie and Kelly Byers for their unyielding love, interest, and encouragement in all my endeavors. To my partner in life and crime, Jessica Joneson – your love, support, and patience has meant the world to me. Finally, I would be remiss if I did not mention the incredible community I have found in Lafayette. The relationships I have formed outside of the university have enriched my worldview and given me so much joy. I am honored to continue to work and live amongst so many wonderful people after completing this degree.

TABLE OF CONTENTS

LIST OF TABLES

LIST OF FIGURES

LIST OF ABBREVIATIONS

ASSURED	device criteria by WHO: affordable, sensitive, specific, user-friendly, rapid and robust, equipment-free and deliverable to end-users
AuNP	gold nanoparticle
DAB	diaminobenzidine
dsDNA	double-stranded DNA, produce via hybridization of two ssDNAs
ELISA	enzyme-linked immunosorbent assay
FAM	6-carboxyfluorescein (single isomer of fluorescent dye fluorescein)
HRP	horseradish peroxidase
LAMP	loop-mediated isothermal amplification
LFA	Lateral flow assay, typically run while laying flat on a surface and applying sample/wash buffers
FLD	Lateral flow dipstick, typically run by placing unit upright in a sample tube that also contains buffer
LFIA	lateral flow immunoassay
LOD	limit of detection
NA	nucleic acid
NTC	no template control
PCR	polymerase chain reaction
PES	polyethersulfone
PID	proportional integral differential
PNA	peptide nucleic acid
POC	point-of-care
POCT	point-of-care test
RPA	recombinase polymerase amplification
RT-RPA	reverse transcription recombinase polymerase amplification
SA-HRP	streptavidin-bound horseradish peroxidase
SA-HRP-AuNP	gold nanoparticles conjugated to streptavidin-horseradish peroxidase molecules
SD-probe	short single stranded DNA displaced from primer during toehold-mediated strand displacement
ssDNA	single stranded DNA oligomer
WHO	world health organization

ABSTRACT

Swift recognition of disease-causing pathogens at the point-of-care enables life-saving treatment and infection control. However, current rapid diagnostic devices often fail to detect the low concentrations of pathogens present in the early stages of infection, causing delayed and even incorrect treatments. Rapid diagnostics that require multiple steps and/or elevated temperatures to perform have a number of barriers to use at the point-of-care and in the field, and despite efforts to simplify these platforms for ease of use, many still require diagnostic-specific training for the healthcare professionals who use them. Most nucleic acid amplification assays require hours to perform in a sterile laboratory setting that may be still more hours from a patient's bedside or not at all feasible for transport in remote or low-resourced areas. The cold-chain storage of reagents, multistep sample preparation, and costly instrumentation required to analyze samples has prohibited many nucleic acid detection and antibody-based assays from reaching the point-of-care. There remains a critical need to bring rapid and accessible pathogen identification technologies that determine disease status and ensure effective treatment out of the laboratory.

Paper-based diagnostics have emerged as a portable platform for antigen and nucleic acid detection of pathogens but are often limited by their imperfect control of reagent incubation, multiple complex steps, and inconsistent false positive results. Here, I have developed mechanisms to economically improve thermal incubations, automate dried reagent flow for multistep assays, and specifically detect pathogenic antigens while improving final output sensitivity on paper-based devices. First, I characterize miniaturized inkjet printed joule-heaters (microheaters) that enable thermal control for pathogen lysis and nucleic acid amplification incubation on a low-cost paper-based device. Next, I explore 2-Dimensional Paper Networks as a means to automate multistep visual enhancement reactions with dried reagents to increase the sensitivity and readability of nucleic acid detection with paper-based devices. Lastly, I aim to create a novel Reverse-Transcription Recombinase Polymerase Reaction mechanism to amplify and detect a specific region of the Spike protein domain of SARS-CoV-2. This will allow the rapid detection of SARS-CoV-2 infections to aid in managing the current COVID-19 pandemic. In the future, these tools could be integrated into a rapid diagnostic test for SARS-CoV-2 and other pathogens, ultimately improving the accessibility and sensitivity of rapid diagnostics on multiple fronts.

1. INTRODUCTION

1.1 The need for point-of-care diagnostics

1.1.1 Global impacts of infectious diseases

Despite incredible efforts in advancing healthcare and medical access, treatable infectious diseases are still a deadly specter in developing countries. Despite progress on specific, well-known global health issues such as malaria, HIV, and tuberculosis, about 4.3 million of global deaths were caused by these and other neglected tropical diseases in 2014 with only marginal improvements made each year since.[1] Similarly preventable deaths in these areas are caused by nutritional deficiencies, maternal/childbirth complications, and other treatable infections. The barrier to reducing these issues is primarily due to monetary and infrastructure deficits. Low-income countries often impacted by colonialism and inequality often lack the resources to provide necessary care to patients most in need.[2] Meanwhile, the United States is currently experiencing its own healthcare crisis with bloated prices and bureaucracy causing reduced access to care for many patients.[3] Both situations produce deadly outcomes for the sick and contribute to the continued spread of these pathogenic diseases worldwide.

In resource-limited areas of both high- and low-income countries, there can be a lack of modern diagnostic laboratory equipment, sterile supplies, consistent electrical services, clean water, and trained technical personnel. The few available healthcare providers in these areas must base treatment decisions largely on clinical observations which often takes time to allow symptoms to fully present, sometimes leading to delayed treatment, misdiagnoses, and worsened health outcomes. To bypass these barriers to effective disease screening, paper-based point-of-care (POC) diagnostics have been revolutionizing global health care by improving access, accuracy, and efficiency of otherwise complex detection systems for disease-causing pathogens. Well-resourced, and high-population areas have also seen a need for low-cost, rapid testing due to the high volumes of patients seeking care. Paper-based POC platforms are known to be easy to safely dispose of via incineration and can ease the financial, temporal, and physical burden that traditional pathogen testing typically presents.[4] It has been repeatedly demonstrated in the case of the rapidly spreading viral pathogens causing the 2015 MERs-CoV outbreak in South Korea and the middle east, and

the recently identified SARS-CoV-2 originating from the Hubei Province of China, that rapid treatment and quarantine of infected patients is crucial for reducing spread and minimizing deaths inflicted by the virus.[5] Time constraints and shear testing volume in these cases are a major challenge for traditional diagnosis in rural clinics and large hospitals alike, making rapid point-of-care devices more necessary than ever. The challenge of being able to test potentially infected patients while keeping them out of hospitals and away from immunocompromised people has resulted in some areas enacting self-quarantine, total lockdowns, and others, like South Korea, developing drive-through testing clinics which provide results in about a day.[6] Providing accurate, efficient, and accessible infectious disease diagnoses is a complex problem for medical systems all over the world, and one crucial part of the solution is the appropriate utilization of accurate and rapid screening with paper-based POC devices.

1.1.2 Targets for Pathogen Detection

Typically, targets used for identification of a pathogen are collected via capillary blood (finger prick), urine, or respiratory samples (nasal swab or sputum). These sampling techniques can sometimes be invasive, but adequate sampling is important for ensuring sensitive, accurate diagnostic results. These targets, or biomarkers, include a large variety of small molecules such as proteins, peptides, carbohydrates, metabolites, exosomes, and nucleic acids that have been previously verified. Proteins are the most common biomarker used in diagnostics as pathogens produce many surface antigens, and immune response antibodies can also be found in high numbers for infected patient samples. Unfortunately, the efficacy of these tests is variable with these targets due to low concentrations of circulating pathogen/biomarkers during early stages of infection, this makes false-negative results a concern.[7] Another method that has proven promising is nucleic acid amplification such as polymerase chain reactions or isothermal amplification techniques, which can produce a detectable product from very low amounts of NAs while also remaining highly specific. Nucleic acid techniques can also be used to monitor strain variations and quantify treatment resistance over time.[8] If the right combination of tools and understanding of disease pathogenesis is used, an early detection rapid diagnostic is possible for each infectious pathogen we identify.

There are a number of approaches to detecting low concentrations of disease-causing pathogens. One of the most relied-upon methods in laboratory settings is the use of nucleic acid amplification techniques such as Polymerase Chain Reaction (PCR), and isothermal amplification reactions such as Loop-Mediated Isothermal Amplification reaction (LAMP) and Recombinase Polymerase Amplification (RPA). These methods detect and amplify specific nucleic acid sequences (typically DNA or RNA) found only in specific pathogenic targets. With these methods we can quickly identify very small quantities of a pathogen, sometimes within as little as a few hours. While researchers have solved some of the issues involved in drying some reagents and created cheap, portable paper systems to detect the amplified nucleic acid products (amplicons), challenges with performing these reactions at the point of care remain. These primary challenges include fully dried reagents stable for long term room temperature storage, portable, low-cost, accurate, heating of these reactions, and user-friendly signal readouts.

1.2 Existing point-of-care diagnostics for infectious diseases

1.2.1 Commercially available and emerging platforms

While most clinical samples are still processed in traditional laboratory settings, point-of-care tests are increasingly being used for diagnosis of common infections. In addition to reducing time to diagnosis and improved treatment outcomes, access to Rapid Diagnostic Tests is also associated with reduced costs.[9] The global market value of this industry was estimated to be USD 28.5 billion in 2019 and is projected to reach a market value of US 46.7 billion by 2024.[10] The growth of this field has coincided with advances in many other areas of research and development, including biochemistry, materials science, electronics, and manufacturing. These advances enabled miniaturization of many key components allowing for portable visual readers such as those used in digital pregnancy tests which perform photometric analysis of test band intensity for users. POC diagnostics are generally marketed as either reusable platforms or fully disposable test strips like the paper-based rapid strep test. Antigen detection platforms such as these are well established in the market, but there is a considerable lack of POC assays that utilize nucleic acid amplification.

Many of the platforms on the market are updated iterations of tried-and-true single protein detection assays with little innovation in the realm of detection mechanisms. In order for these platforms to be suitable for global use, the World Health Organization (WHO) has published

ASSURED criteria which holds a high standard for new POC platforms.[11] The ASSURED criteria requires new POC platforms be Affordable, Sensitive, Specific, User-friendly, Rapid and robust, Equipment-free and Deliverable to end-users.[11] Research has shown that new mechanisms could be easily incorporated into current technologies to meet these criteria, such as several papers which have repurposed portable glucose meters to perform electrochemical pathogen detection.[12,13] New colorimetric signal enhancement mechanisms could be used with the commercial pregnancy test photometric readers, and researchers are already using smart phones for visual analysis as well.[14] Further still, new platforms themselves should be brought to market to allow integration of traditional laboratory methods that were never before done out of the lab, such as Enzyme Linked Immunoassays (ELISA)s.[15,16] There is room for both retrofitting existing platforms for new purposes, and disruptive platform innovation. The primary bottleneck to the latter is the need for new manufacturing solutions that can aid in the mass-production of low-cost devices. One considerable advantage of paper-based devices over plastic or glass lab-on-chip devices is the relative simplicity of converting roll-to-roll and pick-n-place manufacturing techniques that already exist for scaling up production.[17] In contrast, lab-on-chip devices are relatively difficult to make, require intense precision and instrumentation in order to function properly, and face many barriers to consistent mass-production.[18,19] There are currently a number of disposable paper-based devices in the research and development stage for companies around the world, but the gap between the lab and the market is still sizeable.

1.2.2 COVID-19 and its impact on the global POC testing market.

In 2020, COVID-19 revealed just how large the lab-to-market gap is and how far behind we are when it comes to being able quickly develop platforms capable of rapid and accurate nucleic acid testing at the POC. While antigen-based tests are reliable, and easy to manufacture, nucleic acid assays are more accurate for diagnosis of early infections but require additional accommodations in order to function. These hurdles are not insurmountable and with smart-phone technologies becoming more accessible rapid nucleic acid testing of viral samples is now commercially available,[20] and even viral load data in the palm of patients' hands will soon be available. There has been increased interest from the medical technology community for these platforms due to the pandemic, but much of the promising research produced in the last 10 years

was not tested out of the lab or intended to be produced at-scale. These gaps demonstrate a need for platform innovation with the capacity for mass-production of fully automated sample-to answer nucleic acid amplification-based assays.

1.3 Paper-based assays for low-cost POC diagnostics

1.3.1 Principles of paper-based biosensing and capillary flow

Traditional biosensing involves three primary steps: (1) analyte transport, (2) bio-recognition, and (3) signal transduction. Each of these steps is vital to a successful assay and I will discuss the relevant aspects of paper-based assay components and challenges associate with each of these critical steps in later sections of this document. The primary challenge for POC devices is the need to simplify the usual laboratory equipment into an integrated and automated device that reduces user steps and potential for user error. Capillary-driven microfluidic devices such as colorimetric urinalysis strips, lateral flow immunoassays (LFIAs), and 2-dimensional paper networks (2DPNs) have been developed to solve these problems by miniaturizing, automating, and simplifying the diagnostic process necessary for bacterial and viral pathogen detection.[21] While there are many ways to achieve the three steps of biosensing, for low-cost POC diagnostics, the most cost-effective method for simple non-quantitative reporting is LFIAs.

LFIAs are typically comprised of four overlapping layers of papers and porous membranes infused with assay reagents (Figure 1.1).[22] While LFIAs may appear simple, their construction involves high level engineering from the substrates and adhesives to the detection and recognition labels and highly controlled mass assembly. Precise flow control of small volume liquids (as low as ten microliters) and stability of antibodies and other agents are vital to a working LFIA. Functionally, a sample (which may or may not be processed with prior lysis or other reaction buffers) is applied to the sample pad. The liquid in the sample flows down the length of the LFIA, hydrating embedded gold nanoparticles (AuNPs) which bind to target antigens via AuNP-conjugated recognition antibodies. This complex continues toward the detection zone where antigen bound AuNPs bind and aggregate in large enough quantities visible to the naked eye via the capture antibody at the test line and excess unbound AuNPs bind at the flow-control antibody line further downstream. Finally, a highly hydrophilic absorbent waste pad at the very end of the strip absorbs the remaining liquid. This process is typically completed within 10-30 minutes and

may incorporate a wash step to aid in final signal clarity and overall transport of particles. It is easily performed and interpreted as the user simply counts the number of visible lines on the strip where 1 or 2 lines indicate a negative or positive result respectively.[22] In the case of the basic LFIA I just described, the capillary driven flow through the membranes is the analyte transport (step 1), the AuNP conjugated antibody binding to the target is the bio-recognition (step 2), and the signal transduction is the aggregation of the target-AuNP complex at the test line (step 3).

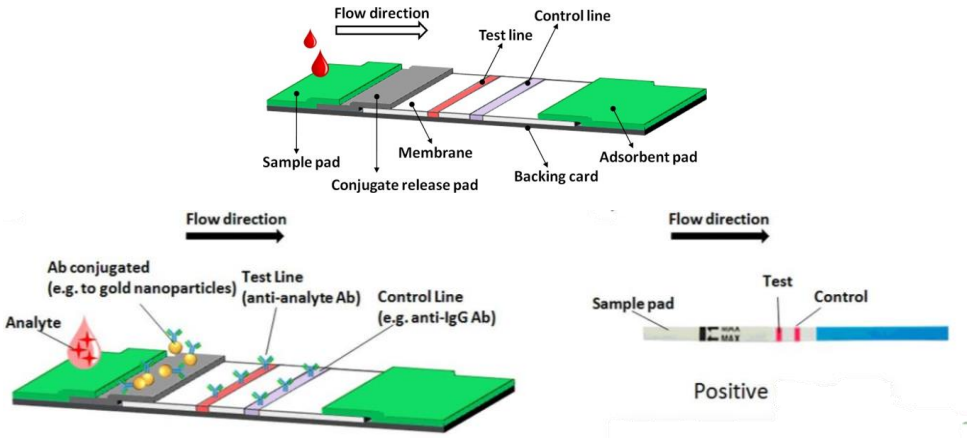

Figure 1.1. Lateral flow immunoassay platform showing primary components and readout. Figure modified from Koczula & Gallotta. *Essays Biochem* (2016) 60 (1): 111–120

1.3.2 2-Dimensional Paper Networks and Protein detection via paper-based ELISAs

In addition to translating assay outputs into simple visual readouts, another challenge to implementing POC devices is the need to simplify standard laboratory steps into integrated and automated devices that reduce user steps and potential for user error. 2-Dimensional Paper Networks (2DPNs) are paper-based platforms, which function similarly to the LFAs I previously described, but utilize multiple channels to achieve integrated automated flow of multiple reagents in order to perform more complex assays at the point-of-care. 2DPNs are one of the more promising approaches as it maintains portability, reduces cost, and can be customized in a variety of ways. Enzyme-based assays, such as 96-well plate-based enzyme-linked immunosorbent assays (ELISAs) are a common method for diagnosing viral pathogenic diseases like the Middle East respiratory syndrome coronavirus (MERS-CoV).[23] MERS-CoV has caused a number of recent epidemics and is currently monitored by the World Health Organization (WHO).[24,25] Limitations

of traditional 96-well plate ELISAs[26,27] for the detection of MERS-CoV include limited accessibility due to the need for cold chain storage of reagents[28] and lack of ease-of-use due to multiple required user steps. In contrast, the low-cost, long-term stability, and ease-of-use of LFIAs and 2DPNs make them advantageous in low resource settings for a variety of applications.[29,30] While the classic LFIA design uses only one-dimensional flow to detect a single antigen of interest by a sandwich assay, 2DPNs have shown potential for conducting multistep assays in paper with multiple flow directions and multiple functions such as performing sample preparation, amplifying nucleic acids, detecting more than one target of interest, or enhancing the visual signal at the detection zone.[31] Previous works have set a promising precedent to use 2DPNs as a platform to perform ELISAs for protein detection, which can be translated for nucleic acid (NA) samples as well.[28,15]

1.3.3 Material Properties and Principles of Fluid Flow in Porous Membranes

LFIAs and 2DPNs both utilize multiple types of paper and other similar porous materials to perform different functions within a diagnostic platform. In this work, the primary porous materials we are concerned with are cellulose, nitrocellulose, and glass fiber, which are all commonly used in lateral flow diagnostics. In this work, glass fiber is used as both the sample and conjugate release pad to absorb and then release the liquid sample and other assay components onto the nitrocellulose. Then the nitrocellulose is the membrane used to transport the complex fluids across the length of the diagnostic, and finally, cellulose is used to absorb excess fluid that has reached the end of the flow path. While cellulose and nitrocellulose are the most commonly used, there are other membranes and materials that can be used for these purposes within a paper-based diagnostic as well. Backed nitrocellulose membranes are typically produced by the controlled precipitation of nitrated cellulose evaporated from a slurry onto a semi-rigid Mylar or Polyester substrate which constitutes the backing. This process forms a semi-homogenous porous material with a specific capillary flow rate defined by the size, distribution, and morphology of the pores, as well as the porosity of the bulk material (total material space between the pores). These properties define the flow rate which generally increases linearly with porosity and pore size distribution. [32] Meaning an increase in pore size distribution (defined as the range of pore sizes present in the membrane) typically results in an increase in capillary flow rate.[32] Flow rate is a

critical component of paper-based diagnostics as it impacts both total assay time and analyte binding efficacy. Glass fiber membranes are manufactured from 100% borosilicate glass extruded into many fibers with small diameters which are suspended in water and placed over a porous screen under vacuum to produce a tightly packed mesh substrate after several rolling and drying steps. Cellulose membranes are produced in a similar fashion to glass fiber, and both are defined by total thickness and bed volume, which is the volume of air in the pores per unit surface area (e.g., $\mu L/cm^2$) which translates to total fluid volume uptake.[33] With the known fluid volume uptake of a certain pad size based on this bed volume, the volume of the AuNP conjugate pad and other diagnostic solutions can be modulated and maintained easily and consistently. These material properties are leveraged later in this work to tune various diagnostic outcomes and produce a reliable, automated, paper-based ELISA in a 2DPN format.

1.3.4 Nucleic acid amplification and detection on paper membranes

Infectious disease diagnosis can require a limit of detection as low as ≤100 copies/ml of pathogenic nucleic acids,[34] thus prompting the development and adaptation of isothermal nucleic acid amplification techniques for detecting and analyzing small quantities of target nucleic acids in point-of-care diagnostics. These isothermal amplification techniques have replaced traditional thermocycle-mediated PCR which is often too laborious and equipment-intensive to perform at the POC. A variety of isothermal amplification techniques for POC detection have been reviewed.[35–37] Of these, loop-mediated isothermal amplification (LAMP) has been popular in recent microfluidic devices. However, there are still challenges associated with this amplification method including the approximately 30-60 minutes of heating required for most LAMP assays, and high isothermal temperature requirements to initiate and maintain amplification. These reactions also suffer from sensitivities to certain chemical adhesives and paper substrates making it difficult to perform these amplification reactions on paper-based platforms without inhibiting reactions or reducing total output.[38] Complex samples containing blood or serum also inhibit these reactions somewhat, however filtration and dilution techniques performed on-paper have proven to reduce this issue significantly, and some membranes such as Polyethersulfone have proven to be suitable for isothermal polymerase-based amplification on paper as well. [38,39]

1.3.5 Recombinase Polymerase Amplification (RPA) and Toehold-mediated Strand-Displacement Primer Design for LFA Detection

Recombinase Polymerase Amplification is an isothermal nucleic acid amplification method commercialized by TwistDx Ltd (now a subsidiary of Abbot) that has been praised in recent years for its speed, precision and robustness.[40] RPA has even been proven to have a comparable limit of detection (LOD) as fluorescent quantitative PCR when using the fluorescent probe scheme in a chip-based microarray.[41] RPA runs at a much lower temperature than LAMP (37-42°C versus 60-65°C, respectively). Additionally, with an average reaction time of 20 minutes, RPA is one of the fastest molecular detection mechanisms and is typically much faster than LAMP which ranges from 30-60 minutes.[42] RPA is also commercially available as an assay development kit, with most crucial reagents fully lyophilized. RPA can include either fluorescent probes, probes suitable for lateral flow tests, and or a basic reaction which uses just one set of 2 primers (1 forward and 1 reverse primer).[42] This simple molecular detection mechanism relies on strand-exchange and recombinase/polymerase activity to achieve exponential production of amplicon duplexes. Figure 1.2 (reproduced from Kersting et al.) below, illustrates how the nfo reaction amplifies a DNA target to produce amplicons that are detectable on an LFA.[43] As you can see in panel (A), the sample is loaded into the reaction where the two forward and reverse primers form a complex with the recombinase proteins (green). These complexes then invade the target DNA at homologous sites where strand-displacement DNA polymerase (red) elongates the primer-established strand while displacing the incumbent DNA strand.[43] Simultaneously, single-strand binding proteins (SSB) (brown) stabilize the newly displaced strand until two duplexes are formed, and the process is repeated. The next stage of the reaction (panel B) relies on a portion of the amplicons produced still containing the reverse primer which carries an antigenic tag at the 5′end (purple). On these amplicons, a modified probe homologous to the center of the amplicon region invades the amplicon duplex and again replaces the incumbent strand there. This invading probe is labelled with a different antigenic tag at the 5′end and a 3′end polymerase blocking group (blue) which is cleaved by the nfo enzyme (yellow) at the tetrahydrofuran (THF) (spacer) site after fully binding to the amplicon.[43] Further polymerase activity (red) continues strand synthesis from the cleaved end of the probe until a double-labeled amplicon is fully formed in this one-pot reaction. Finally, (panel C) the dual-labeled amplicon is captured and detected at the test line as previously described

in Figure 1.1 of this thesis. (D): Positive and negative representative samples on a Millenia HybriDetect LFA show expected results for their assay.[43]

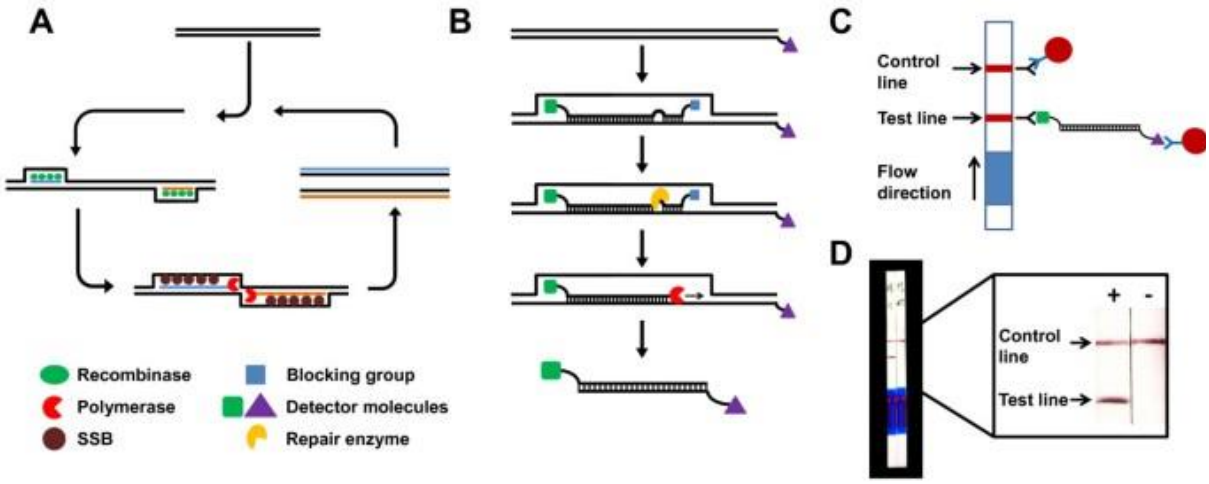

Figure 1.2 Recombinase polymerase amplification via nfo kit for lateral flow detection. Reproduced from open source publication by Kersting et al. published in *Malaria Journal*, part of Springer Nature.[43]

RPA is still a relatively new assay compared to other, more popular assays such as LAMP. The earliest publication on RPA was released in 2006 and, according to a recent review of the field, more than 250 publications have been published since.[44] Interest, knowledge, and development of RPA assays is in a critical period that may solidify it as the premiere isothermal detection method in the next 10 years.[44] Unfortunately, the nfo kit was discontinued by TwistDx in early 2020 which presents difficulties for accurately detecting amplicons via LFA at the point of care and translating these assays out of the laboratory. Much of the previous literature demonstrating RPA-LFA detection used this method, therefore alternative designs are scarce. Still, RPA is a promising reaction, and a recent publication has shown it is still possible to utilize this basic concept of an annealing probe system without the need for a THF residue or the proprietary cleaving enzyme. Research from J. Qian et al. demonstrated this in their enhanced recombinase polymerase amplification (eRPA) assay, which showed impressive sensitivity and specificity for SARS-CoV-2[45]. Other research has shown that modifying the forward and reverse primers via oligo tails is another promising method for improving signal transduction of RPA reactions which suggests molecular tags could also be promising.[46]

Toehold-mediated strand-displacement via three-way branch migration utilizes short, single-stranded oligonucleotide sequences complementary to a portion of the primer strand which are annealed to the median of the primer prior to reaction initiation. These partial duplexes leave one end of the primer open for hybridization which acts as the "toehold" for recognition of the target strand which then displaces the incumbent strand and allows for amplification to begin. This initial displacement is entirely driven by the non-enzymatic thermodynamic circumstances which dictate DNA hybridization and dissociation.[47] This relationship is described by the Gibbs free energy change (ΔG) associated with the formation of each base pair under the specified reaction conditions. In this application, the energy required to break the hydrogen bonds holding the primer-displacement probe duplex together must be low enough so as not to impede probe-target strand exchange while also remaining high enough to avoid spontaneous dissociation at elevated reaction temperatures. This toehold-mediated strand displacement mechanism is well-visualized by Simmel et al.'s diagram[47] (reproduced below in Figure 1.3) where (A) shows duplex unit *S* which has a toehold consisting of the single-stranded overhang *h** (shown in red), and a single-stranded invader strand X which contains region *h* (shown in purple) complementary to the toehold where the two strands hybridize (B). The invader strand X then displaces the incumbent strand *b* (light blue, later denoted as Y once fully displaced), with intermediate steps in the branch migration process shown in (C-E) to ultimately form the duplex L in (F).[47]

From this background, I discuss in Chapter 7 an alternative design method which utilizes both RPA primers as molecularly labeled ends and protects against false positives caused by primer-dimers by incorporating a strand-displacement probe on each primer which will impede primer self-dimerization. The combination of non-enzymatic toehold-mediated strand displacement activity with the enzymatically driven RPA reaction has not previously been studied and could prove promising after adequate parameter tuning.

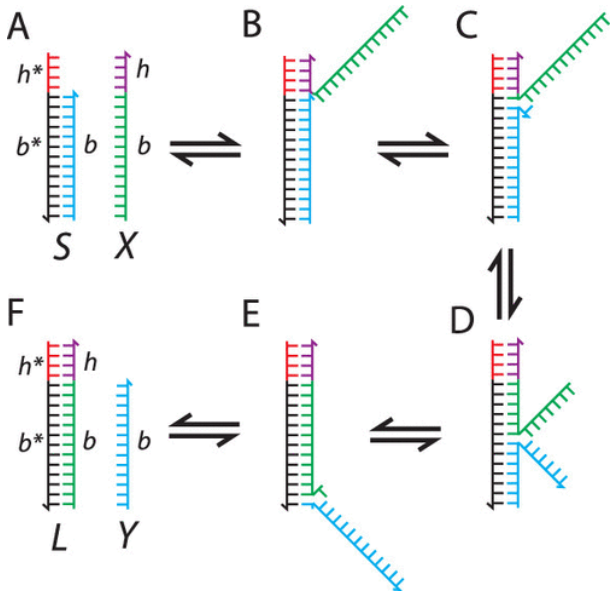

Figure 1.3 Toehold-mediated strand displacement via three-way branch migration. Reprinted with permission from *Chem. Rev.* 2019, 119, 10, 6326–6369. Copyright 2019 American Chemical Society.

1.4 Challenges for emerging platforms and proposed work

1.4.1 Heating samples at the POC

Advances in microfluidics and electronics have contributed promising devices to attempt to achieve precise, low-power, and sustained heating necessary to implement rapid diagnostic tests at the point-of-care (POC). To date, researchers have used hotplates,[48] custom printed circuit boards (PCBs),[49] coffee mugs,[50] exothermic chemically heated chips and cups,[51,52,53] thin-film polyimide heaters,[54,55] and traditional incubation ovens[56] as a heat source for POC devices with varying degrees of success.[13,14] Standard laboratory-grade incubation ovens are accurate and can incubate large volumes of samples at one time, however even a 'mini' six liter incubator requires 80 watts of consistent power that can only be obtained from a modern electrical grid or a generator.[59] Although chemical heaters do not require batteries or external power supplies, they typically rely on highly variable exothermic reactions such as magnesium iron alloy (MgFe) and saline cartridges which are single-use and are difficult to control without a phase change material (PCM) chamber to buffer the sample temperatures.[52,60,61,62] Hot plates and coffee mug-based units

are also oversized and require excess energy to heat the enclosed space. Current PCB-based heaters, while effective, require long copper traces which result in slow ramp-ups to the target temperature and excess heat and power consumption.[49] *Hwang et al.*, experienced issues with sample overheating and control of the working voltage for each heating stage of a polymerase chain reaction (PCR) to detect *Chlamydia trachomatis.*[63] These challenges remained problematic even after reducing the size of the heating pattern and utilizing a complex electronics system to perform the thermocycling.[63] Additionally, PCB manufacturing uses a lot of metal (typically copper) to make up the bulk of a single chip, making traditional PCBs a poor choice for disposable POC assay integration. Large thin-film polyimide heaters present similar overheating and power consumption issues but could be useful if successfully miniaturized. In order to effectively implement POC and in-field diagnostics in low resource settings, there is a critical need to continue improving these technologies for integration of custom, well controlled, localized heating of reactions and other components either into the disposable device itself or into a supporting reusable electronic platform. To meet this need, I developed low-cost, inkjet printed thin-film heaters for heating small regions of paper-based devices containing low volume samples for the purposes of controlling fluid flow where wax vales are used and incubating isothermal nucleic acid amplification reactions as well as other assays. This work is discussed further in Chapters 2, 3, and 4.

1.4.2 POC ELISAs: Automating Sample and Reagent Flow with 2DPNs

Design of a fully integrated 2DPN ELISA requires optimization of the reagent delivery in order to improve performance and produce reliable signal enhancement.[64] Existing 2DPN devices are categorized by the location of fluidic inputs: the "leg" design, where reagent pads are placed at the far end of the leg which then extends and intersects with the main lateral flow body (typically at a 90º angle),[65] or the "linear" design, where the reagent pads are placed directly on the main lateral flow body.[28] Capillary flow in one-dimensional and two-dimensional nitrocellulose devices are often characterized and modeled using an extension of the Lucas-Washburn and Darcy equations.[66] Previous 2DPN ELISAs required as many as five to six fluid inputs with one or more wet reagents that were prepared fresh.[15,28] By analyzing previous "linear" and "leg" designs and performing mathematical modeling of capillary flow through various nitrocellulose channel widths, I was able to design a device that utilizes a combination of the two design methods, as well as a

unique delay valve, to sequentially deliver reagents to the detection zone for a fully automated 2DPN ELISA. This will enable us to incorporate enzymatic signal amplification more effectively in the sequential flow, reduce the number and volume of washes, and reduce the volume of enzymatic reagents. Furthermore, I ensured all necessary reagents for the ELISA can be fully dried and stored in the assembled device. Rehydration and subsequent flow of those reagents were also optimized. This work is discussed in Chapters 5 and 6.

1.4.3 RPA for rapid detection of SARS-CoV-2

COVID-19 is a rapidly spreading viral infection that is caused by SARS-CoV-2 virus identified in 2019. The total impact of COVID-19 is still developing, but it is clear that as coronaviruses and other rapidly mutating pathogens infect humans there needs to be better rapid test development processes ready for the necessary global response. It is reasonable to desire a pan-coronavirus rapid assay that will identify both current infectious strains and will have a high likelihood of detecting newly identified strains in the future. However, other human coronaviruses which cause mild infections such as the common cold are also genetically similar to SARS-CoV-2.[67] The spike glycoprotein encoding gene (known as the S gene) was identified by researchers in Wuhan as the most specific region for targeting with PCR to distinguish SARS-CoV-2 from other coronavirus strains.[67,68] I propose a Reverse Transcriptase RPA assay that can be integrated onto a paper-based platform for specific rapid POC screening of SARS-CoV-2. Rapid testing that is as accurate as PCR while being as fast and convenient as a typical antigen test would drastically improve both patient outcomes and public health decisions that are based on confirmed positive cases in a given area. It is critical that this technology be properly developed for the enormous scale it is needed for both now and in the future. This research is just a small part of the necessary work needed to make this vision possible.

1.5 Thesis overview: platforms and molecular mechanisms for improving signal transduction and signal enhancement in multistep point-of-care diagnostics.

Each component of a POC test is critical to the reliability of the testing outcomes. The blocking of membranes against non-specific binding in antigen assays has become a long-abiding industry standard.[69] Similarly, future platforms will soon incorporate low-cost, high-fidelity

heating for the isothermal amplification of nucleic acids. Automating sample heating in the field and at the POC has long been a challenge, as it is a key factor in minimizing equipment and user steps. As discussed in **1.4.1 Heat ing samples at the POC** there have beein significant efforts put forward to solve this need in an elegant and economic fashion, yet each solution bares unfortunate thermal inconsistencies, requires combersome power supplies, or presents environmental issues if used as a disposable unit. To build on this literature, I proposed inkjet-printed, miniaturized heaters (microheaters) for low-cost, low-power thermal control in paper-based diagnostics. This work resolves several issues related to power requirements, reusability, cost, and accuracy of thermal regulation for POC assays. In Chapter 2, I detail the development and characterization of the inkjet-printed microheaters. Chapter 3 expands on the resulting thermal distributions produced by different serpentine designs and includes a thermal distribution analysis of samples heated by a microheater via a Multiphysics COMSOL model. In Chapter 4, I implement the microheaters into two distinct assays and report successful assay integration with a portable, cell phone-powered device developed by the Linnes Lab. In Chapters 5 and 6, I describe the design and testing of a 2DPN paper device for the detection of MERS-CoV in collaboration with Crosslife Inc. and my colleague Anna R. Bird. Chapter 5 details the microfluidic platform development via flow rate analysis and comparison studies of several design parameters. Chapter 6 utilizes this established platform in testing and optimization of a fully dried ELISA to improve nucleic acid amplicon detection. In Chapter 7, I describe strategies and demonstrate the development process for utilizing atoehold-mediated strand displacement mechanism in conjunction with molecularly labeled primers in a novel RT-RPA reaction that may improve the assay by reducing false positives in LFA outputs.

2. DEVELOPMENT AND CHARACTERIZATION OF INKJET-PRINTED MICROHEATERS FOR LOW-COST, LOW-POWER THERMAL CONTROL IN PAPER-BASED DIAGNSOTICS

Parts of this chapter are reproduced from Ref. [70] from the Open Access Journal *Analyst*, in the Royal Society of Chemistry. Contributors to this work include: Dr. Li-Kai Lin

2.1 Rationale

Heating samples efficiently and easily at the POC has been a concern of the field since its inception. As we discussed in 1.4.1 *Heating samples at the POC*, there have been a wide range of attempts in many different formats, but there has been a distinct lack of direct integration with paper-based platforms. Printed miniaturized heaters (microheaters) have promising and predictable heat transfer properties.[71,72,73] These printed heaters rely on joule heating (also referred to as resistive/ohmic heating) wherein the energy of an electric current is converted into heat as it flows through a conductive material of known resistivity.[71] Many materials-based and biosensing publications have demonstrated that ink-jet printed silver traces providing conductive lines on various substrates can be fabricated with acceptable consistency, conductivity, and reliably mass-produced via roll-to-roll manufacturing.[74,75,76] These, and other research efforts present a number of promising methods for producing highly accurate and robust conductive traces for heating small samples. By leveraging the precision and scalability of inkjet printing and rapid curing methods, we can develop versatile, robust, and sustained heating for various biological reactions used in POC assays.

Resistive heating (also known as "Joule Heating") is the process where the energy of an electric current is converted into heat as it flows through a material of known resistivity (ρ).[71] By changing the inherent resistance of the conductive printed trace by using different serpentine designs, it is possible to control the amount of heat-energy that is produced by the trace in a given area. The overall resistance of the trace is determined by calculating the area of the perpendicular face of the trace and the path length of the trace (represented by Equation 1 below).

$$R = \rho \frac{L}{A} \qquad \text{Equation 1}$$

Where R is measured resistance (Ohms) of the printed trace, ρ is resistivity, A is cross-sectional area (m^2) and L is the path length (m) of the printed trace.[77] Cross-sectional area and

length of the trace are the factors most easily tuned by simply changing the design of the trace before printing.

Low-cost, inkjet-printed resistive microheaters are needed to provide rapid and sustained low-power thermal control of biological reactions at localized regions in paper-based assays. By tuning the printing parameters, I will produce miniaturized joule heaters able to precisely control local temperatures during incubation of biological samples on paper membranes for POC assays. I aim to produce robust methods for producing, evaluating, and integrating these heaters at the research level, while setting the stage for reliable production at-scale. To my knowledge this is the most in-depth investigation of printed conductive traces used specifically for fully integrated and automated heating of microfluidic samples on paper membranes at the POC.

2.2 Materials and Methods

2.2.1 Ink and deposition method selection

Several inks and deposition methods were tested, including syringe deposition on backed nitrocellulose. However, none of these early efforts could produce accurate, consistent conductive traces at the resolution needed for small paper devices. Inkjet printing, which could be easily switched to high-resolution-roll-to-roll printing in the future, was then chosen for its accuracy and speed of production on a large scale. A Silver ink was chosen over copper or carbon due to copper's high reactivity to environmental factors which could ultimately change the resistance of the microheater, affecting its consistency and carbon ink high resistivity. The Novacentrix ink used here is water based and has a viscosity of 8-12 cP with a surface tension of 28-32 mN/m. The Kapton substrate surface energy is also 28-32 mN/m and was chosen for its durability and high thermal stability after testing several other substrates including HP Photopaper (glossy), Novele ™ substrate (from NovaCentrix), and others.

2.2.2 Geometry and path design

Designs were created in Adobe Illustrator (Adobe Systems Incorporated, San Jose, CA) with variable path lengths (L), line widths (w). The number of printed layers determined the z-height and cross-sectional area which determined the total resistance of the trace (Figure 2.1). A

simplified approach was taken for these designs with the hope that others can easily replicate and adjust for their own needs using any simple line or path tool found in most vector editing software.

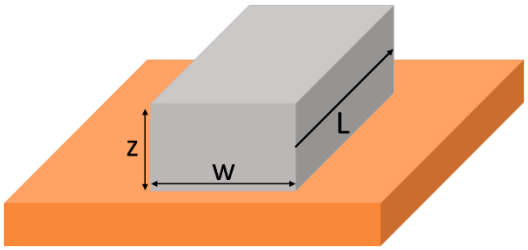

Figure 2.1. Schematic of conductive trace measurements.

2.2.3 Inkjet printing and curing

The resistive microheaters were printed using a Dimatix printer (DMP-2850, Fujifilm) which uses piezoelectric inkjet technology to deposit path designs (traces). Nanosilver Ink (JS-B40G, Novacentrix) containing 40% silver by weight was applied by the Dimatix onto a Kapton substrate (Kapton HN Semi-Clear Amber Film, 5 mil 125 µm, DuPont,). The Nanosilver ink was filtered through 0.2 µm filter (Whatman® Puradisc 13 syringe filters made of 0.2 µm, PTFE,) to remove large aggregates, and a 10pL nozzle cartridge (Fujifilm) was used. Design files were exported from Adobe Illustrator to a Bitmap file type with resolution 725.71 dpi. The waveform file directing recommended jetting voltages specific to JS-B40G ink was provided by Novacentrix Inc. and adjusted for each jet using the Drop Watcher function prior to printing. Print settings included a sabre angle manually adjusted to 7.9° according to the user manual, and 35µm drop spacing at room temperature with platen vacuum on and platen temperature set to 50°C. The printed traces were heat cured via baking at 400°C for 10 mins directly after printing. These printing and curing methods were used for all heating characterization and application studies. For long term storage, Kapton tape (3M 5413 Dupont, DuPont,) was applied to the print-side of the trace over the heating sections of the designs and left on during experimentation, this reduced oxidation of the printed trace over long periods of idle storage.

2.2.4 Micro and Macro analysis of microheaters to characterize printing and curing.

Individual traces were measured post-curing with a handheld multimeter (AM-510, Amprobe) to determine initial resistance and re-measured before each use. The resistance of printed lines was determined by the two-point probe method. These measurements were then compared with predicted resistance calculations based on path length versus cross sectional width ratio as it relates to overall microheater resistance. Profilometry measurements and SEM images of heat-cured and non-heat-cured samples (SEM samples were sputtered with platinum) were also established for a range of samples.

2.2.5 Durability Testing

A representative sample of Design A (1.8 cm in total length) was used to perform a simplified test similar to Cordill *et al.*'s methods[78] for strain testing of thin films on polymer substrates. This included first measuring the initial total length (L_o) of the sample and initial resistance (R_1) of the trace using the two-point probe method with a multimeter (AM-510, Amprobe, Everett, WA). The sample was then subjected to bending between two gloved fingertips in both the convex and concave conformations at which point the change in length (ΔL) was manually measured and recorded. The resistance of the sample was again measured (R_2) and the change in resistance ($\Delta R=R_1-R_2$) and strain ($\varepsilon = \Delta L/L_o$) were calculated. Another representative sample of Design A was placed in distilled water for 3 days with pre- and post- treatment resistance measurements recorded with the two-point probe method. Another series of these tests were performed on Design 1_1.

2.3 Results and Discussion

2.3.1 Early inkjet printing results

The JS-B25HV Nanosilver Ink produced conductive traces when left to dry at room temperature without additional curing when printed on HP Photo paper (**Figure A. 1**) as well as with the Novacentrix "Novelle" substrate. However, when I captured an SEM of an untreated trace (no sintering or oven-curing) on the Novelle substrate, it was clear that the silver nanoparticles were not producing a single unified trace of bulk silver but were in fact just touching enough as

aggregated particles for conductivity to be possible (Figure 3). This brought up concerns around reliability of this method as well as the long-term stability of these traces given the greater oxidative potential of such a porous trace. Additionally, using the microheaters to produce heat on both the HP photopaper and the Novacentrix "Novelle" substrate, caused melting/burning and deformation of the substrates due to low heat-tolerance. These substrates also did not tolerate low-temperature oven curing (65°C) when I attempted to improve the nanoparticle coalescence of these samples. When using the Kapton substrate, traces did not become conductive until after oven-curing due to the need to evaporate the ink solvent fully and quickly.

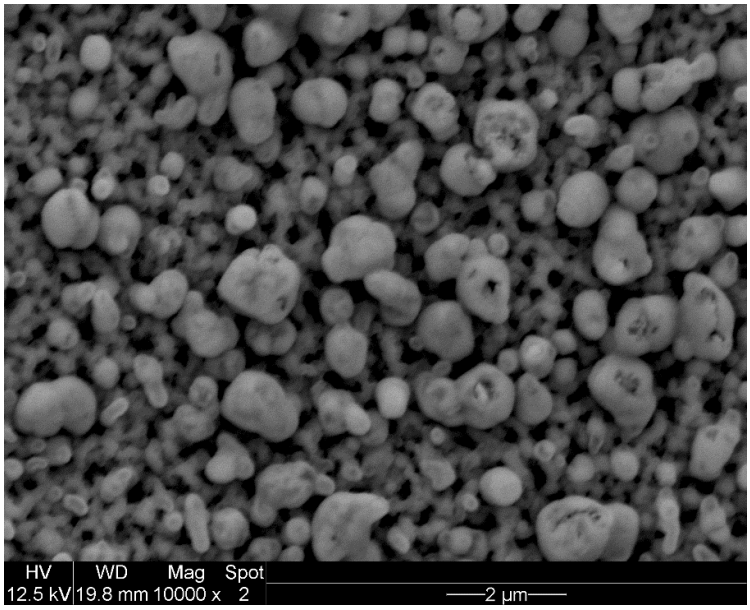

Figure 2.2. SEM of untreated JS-B25HV Nanosilver Ink printed on Novelle Substrate.

Exceptionally thin designs (in terms of path-width) under all printing conditions resulted in highly inconsistent printed traces. Printing consistency within early batches was a concern because during a particularly long print job, the individual jets would sometimes clog, which resulted in unusable or abnormally high resistance traces. If a trace was still conductive, but had an abnormally high resistance, a sintering process could be applied to further coalesce the silver nanoparticles. This sintering process involved treating each individual microheater with a high voltage (~2 volts depending on the resistance of the microheater) and resulted in greatly reduced resistance by several Ohms (**Figure A. 2**) for traces printed on HP Photopaper without damaging

the substrate. However, due to this process being arduous and potentially introducing greater variability in microheater performance both in short-term and long-term use, this practice was discontinued. Another method I tested was flash-sintering[79], which when automated, could be applied to roll-to-roll printed samples quite easily in order to avoid high temperature baking during mass-produciton[80]. However, on this small scale and under my manual use, flash sintering did not prove as consistent of a method as I had hoped. This motivated me to improve overall printing consistency, which was optimized by adjusting the number of nozzles jetting for a particular print job, and careful selection and jetting voltage of each jetting nozzle before printing. This sintering method could still be of interest to extend the life of individual or batched microheaters after long periods of storage. The final printing and oven-curing process described previously in the materials and methods section of this chapter were established with help from my colleague, Dr. Li-Kai Lin, without whom optimizing this work would have been much more difficult.

2.3.2 Imaging and profilometry analysis of printed traces

From the SEM image shown in Figure 2.3, it is clear that the Kapton substrate and silver ink with high-temperature oven baking resulted in a semisolid layer of conductive bulk silver when compared to literature[81,77] and our previous results. This curing method simply involves the evaporation of solvent leaving the remaining 40% bulk silver on the surface of the substrate[77]. Although average particle size in the liquid ink we used is 60-80 nm,[82] the curing process clearly resulted in nanoparticle coalescence creating a semisolid film. Grain formation appears to have occurred with average grain size being 250-500 nm and larger aggregates up to 800 nm to 1 µm in diameter. This grain formation is a well-known phenomenon and previous microstructural characterization has revealed differences in conductivity for small versus large grains.[77] A

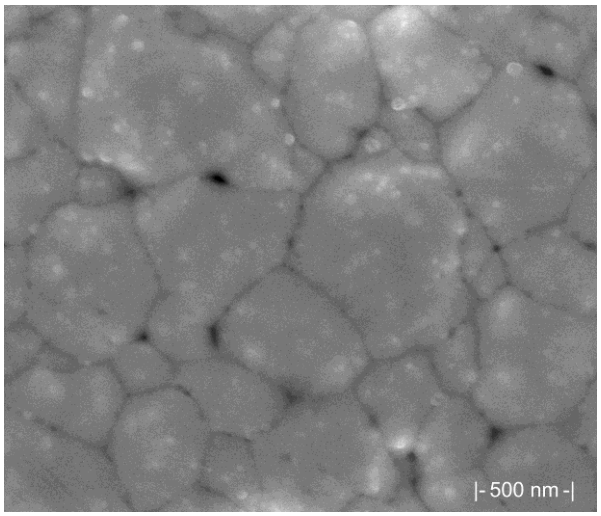

Figure 2.3. SEM of printed trace on Kapton film, post-oven curing showing a semi-solid layer of highly coalesced nanoparticles forming large grains suggesting high conductivity.

curing treatment protocol by *Shen et al.* with 25wt% nanosilver ink produced a semi solid layer similar to ours but with more gaps between particles and smaller coalesced grains.[81] Results by Saraf *et al.*[83] showed an increase in conductivity for higher curing temperatures compared to lower temperatures for microparticle based inks. The depression of melting temperature for silver nanoparticles, known as the "scaling law",[84] is well documented in nanoscale literature. Surface defects such as small gaps between grains are common for these methods but are not of great concern for the application of heating.

The profilometry results of oven-cured traces revealed inconsistencies in printed z height between designs of varying trace thicknesses (print width). Specifically, Design 1_1 (Figure 5) with 0.53 mm path-width had a z height of 600-800 nm while Design 1_2 with 0.35 mm path-width had an average z height of 1000 nm (Figure A.3). This data suggests that wider trace widths produce a more rounded and even trace while thinner traces are more jagged and supports earlier results that thicker path-widths produce more consistent printed traces. From these results, I have determined that, to ensure a consistent z-height across a trace, the designed width/thickness should not be less than 10x the set drop-spacing and care should be taken to ensure the optimum number of print heads are activated and not clogged. The effect of drop spacing on inkjet-printed thickness has been investigated previously, and shows that this largely depends on the viscosity and surface tension properties of the ink and substrate interactions.[85] The profilometry data allowed us to gather an average z height of the traces to predict the resistance of new designs. The first set of designs were averaged and an average resistance from each batch was calculated and compared (contains all dimensions and resistance details for these and other designs discussed in this chapter).

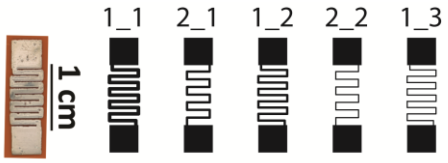

Figure 2.4. Initial resistor designs with calculated resistances of 5.4, 5.7, 8.0, 11.3, 16.1 Ohms from left to right.

2.3.3 Resistivity analysis

The general resistivity of the printed traces resulting from these methods is 43.0 μΩ*mm. This converts to 2.3×10^7 S/m, while bulk silver has electrical conductivity of 6.16×10^7 S/m. This is an acceptable conductivity as it is expected that bulk silver would be more conductive than the printed traces, which are known to have surface defects and printing inconsistencies. After this, I used the resistivity to quickly calculate a predicted resistance of an entirely new set of traces (Design A, B, C, D with heating regions 11.9 x 9.2 mm to 23.7 x 18.3 mm, Figure 5). Means and standard deviations of the resistances of each printed trace design were compared with a minimum of 25 prints for each design.

By maintaining a single print layer for all batches, I optimized the width of the printed design and the path length of the trace for each heating area. Although there are slight differences between individual microheater resistances, these differences are incurred by the printing process and do not greatly affect the functioning of the microheaters, nor does it drastically affect the power consumption. Having characterized the first set of simple serpentine designs (Figure 5), I was able to quickly move to more complex designs (Figure 6. A, B, C, D) covering a larger heating area by applying Equation 1. The predicted resistances of the printed traces closely matched the final average resistance of each design. Some deviation from estimated resistance was expected due to the variation induced by the printing and sintering processes, however I was able to predict the resistance of a trace within 20% of the average for all traces. Average resistances of printed microheaters were all less than the predicted resistance. I assumed an average z height of 700 nm for remaining designs A, B, C, and D, which proved accurate for Design A, which had a z-height of ~700 nm. This predictive method is useful as a guideline for new designs until measurements from a large batch of printed microheaters can be made. It may be worthwhile to simply make predictions of maximum and minimum expected resistances based on a given design by using the minimum and maximum expected z heights resulting from a single layer of the inkjet-printed ink. The print analysis for designs C and D in Figure 2.5 suggest that the variability of the measured resistances may seem to scale with the size of the traces. In any case designs C and D are so large and the heating elements so spread out that they would not make adequate heaters for POC applications, and commercial polyimide thin film heaters would be more feasible at that size

anyway. These designs were included to test the limits of this fabrication and resistance prediction process.

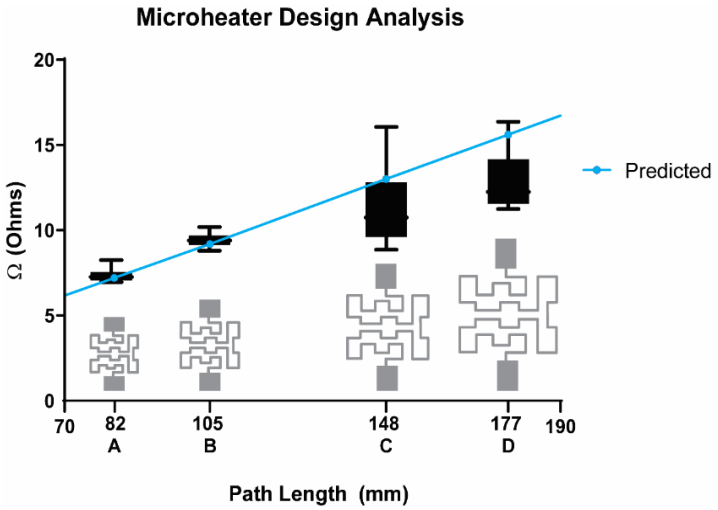

Figure 2.5. Design analysis of printed versus predicted resistance of new heater design. Design shapes in grey. As path length increases, resistance of the traces increases also increases proportionately. Box plots of printed resistances (n=25, N=4 batches) in black with error bars representing max and min values. Predicted resistances shown in blue are 7.2, 9.2, 13.0 and 15.6 Ohms and average printed resistances were 7.4, 9.5, 12, and 15.3 Ohms for designs A, B, C, D respectively. This method was accurate within 1 Ohm for larger print designs when printed in 4 batches of 25 microheaters per design.

These fabrication and resistance prediction methods have proven to be reliable for generating new heating designs not previously tested. It stands to reason that traces with resistances above the maximum predicted values would suggest a clogged print head, poorly mixed or filtered ink, or unsuccessful curing. Traces below estimated resistance values benefit from the particle coalescence discussed previously. Table 1 summarizes both sets of designs I have investigated in this chapter and supports the claim that this method makes these microheaters incredibly tunable to specific needs for any small volume POC paper-based assay when an appropriate trace thickness is used in the initial design.

Table 1. Microheater design average printed resistance details (n=25, N=4 print batches) and resistance calculations given ink resistivity of 4.3E-5 Ohms*mm and printed trace height of 700 nm.

Design	**1_1**	**2_1**	**1_2**	**2_2**	**1_3**	**A**	**B**	**C**	**D**
Path length (mm)	46.14	32.45	46.14	32.45	46.14	82.03	105.19	147.82	177.38
Stroke/width (mm)	0.53	0.35	0.35	0.18	0.18	0.70	0.70	0.70	0.70
Heating Area (mm x mm)	4.8 x 8.75	3.8 x 8.75	4.6 x 8.75	3.6 x 8.75	4.4 x 8.75	11.9 x 9.2	14.5 x 11.3	20.1 x 15.4	23.7 x 18.3
Calculated Resistance (Ohms)	5.4	5.7	8.0	11.3	16.1	7.2	9.2	13.0	15.6
Measured Avg. Resistance (Ohms)	4.8	5.0	7.6	10.5	15.3	7.4	9.5	12.0	15.3

Ultimately, printing variability issues with respect to microheater size and design would change in the event of scale-up production via roll-to-roll printing and optimization of that process has been as source of many other investigations.[74] In fact, linewidths of 1 μm have been shown to be achievable with a combination of certain roll-to-roll and inkjet printing methods with silver ink.[86] Meanwhile, a more traditional roll-to-roll system reached a linewidth of 20 μm by adjusting the force applied between the rollers involved in ink application.[87] This suggests that scaled-up production of these microheaters could be possible and the prediction of certain microheater designs via Equation 1 could aid in the optimization of that printing process as well as in the creation of new designs for many more uses than I have investigated presently.

2.3.4 Durability assessment and cost analysis

While these microheaters are not expected to be exposed to the variable stresses experienced by wearable sensors or implantable devices, resistance stability is a vital factor. The microheaters were found to have only a 0.1 Ohm (or 1.3 percent) change in resistance and did not retain any visible deformation after being subjected to both concave and convex bending, resulting in a strain of $\varepsilon = 0.16$ for a Design A microheater covered in Kapton tape. A series of more aggressive bending on a single Design 1_1 microheater (covered in Kapton tape) showed excellent durability despite creasing of the Kapton substrate (results summarized in Figure A.1). After this

creasing in one direction, the change in resistance was 0.2 Ohms. Creasing in the other direction resulted in an additional 0.3 Ohm increase. This aggressive treatment resulted in a total resistance change of only 0.5 Ohms (9.3 percent difference) and did not otherwise affect the performance of the microheater. The microheaters can withstand submersion in distilled water for 3 days without measurable change in resistance, indicating these microheaters are compatible with wet samples and can be used in the field. Further, the microheaters maintain a stable resistance over a three-month time-period at room temperature. Resistance changes due to oxidation of silver nanosurfaces can be halted by covering the printed traces with Kapton tape or storing the microheaters in an oxygen reduced environment. When covered with Kapton tape the microheater resistances remain stable over 6 months and could likely remain stable for much longer. The cost of the printed microheaters is significantly less than that of commercial thin-film heaters. The smallest commercial polyimide heaters available from Omega are 1 x 1 inches and are sold for $87.75 each.[88] Meanwhile, our microheaters have an estimated material cost of $0.17 for Design 1_1 and $0.58 for Design D which was the largest design printed (Table A.2) and can be designed to reach resistances as low as 2 Ohms (**Figure A. 5.** Low resistance microheaters are possible to create using the technique described in the main text. The design here has fewer serpentine turns resulting in a shorter path length. Specs: trace width: 0.529mm, path length: 24.264 mm, total heating area: 4 mm x 8.8 mm.).

2.4 Conclusions & Future Directions

I identified several tuning parameters for these inkjet-printed microheaters including conductive trace width, height, geometry, curing and sintering methods, as well as substrate materials. While these designs and their fabrication methods are successful in this limited analysis, further investigation of drop-spacing and other print settings can decrease variability of printed traces and give rise to optimized roll-to-roll settings which need to be tested at-scale. This need for scalable testing and integration into a multi-component device via a pick-and-place machine cannot be overstated. Additionally, other design tools that ensure perfect symmetry may be desirable and other serpentine or spiral path designs could prove useful depending on the needs presented by platform integration. To my knowledge, this work is unique in terms of its focused

depth and application on thermal control for POC diagnostics but could prove useful to other areas of low-cost electrochemical sensing.

3. THERMAL ANALYSIS AND MODELING OF MICROHEATERS AND POROUS MEMBRANES CONTAINING LIQUID SAMPLES

Parts of this chapter are reproduced from Ref. [70] from the Open Access Journal *Analyst*, in the Royal Society of Chemistry.

3.1 Rationale

Thermal consistency is a key factor in managing reaction kinetics for isothermal nucleic acid amplification, bacterial growth, and other aspects of POC assays. Many scientists apply great detail to optimizing of their reaction conditions in real-time PCR machines.[89] However there has been some data showing that, at least for low-cost rapid diagnostics using a lateral flow readout, the lack of resolution of this readout causes temperature to be less of a factor on overall assay sensitivity compared to other reaction factors such as incubation time.[90] From a practical standpoint, it makes sense to weigh the conditions necessary for an assay to perform optimally against its usefulness at the POC, if meeting those conditions becomes too cumbersome. With this in mind, it makes sense to expect some thermal irregularity from such small samples and simple heaters, depending on their intended use. When applied to bacterial growth assays and paper-based antibiograms[56], cell culture temperatures, while optimal at 37°C, can still survive and grow anywhere between 35 and 42°C. Similarly, as long as critical enzymes are not degraded, nucleic acid amplification reactions also have a range of acceptable temperatures (most efficiently between 65 and 72 °C for LAMP).[91,92] However, wax valves must reach a minimum temperature (80°C) relatively quickly to ensure adequate phase change, and uneven heating across the width of the wax valve could result in undesirable flow outcomes.[55,93] It is for this reason the importance of appropriate trace design for the intended use cannot be overstated. In this chapter I investigate thermal profiles for two of my microheater designs produced by both experimental heating sessions and COMSOL Multiphysics models to aid in my assessment of these microheaters as tools for POC thermal control.

3.2 Materials and Methods

3.2.1 Heating Assessments

An infrared (IR) thermal imaging camera (A300 Series, FLIR Systems, Sweden) and a 1550 DC Power Supply (BK Precision, Yorba Linda, CA) were used to characterize the initial and long-term heating of the microheaters. The initial characterizations with non-insulated samples provided benchmark power settings which were then adjusted for sample needs (specified in later sections). A heating consistency test was done to assess reusability wherein a 5 Ohm microheater (design 1_1) was heated 10 times for 15–20 minutes each using 220 mW.

3.2.2 COMSOL Modeling

In order to confirm my temperature sampling methods during the pathogen detection experiments and further characterize the heating distribution throughout samples heated by the different microheater designs, I created a physics-based software model. Evaluations of the heating profiles produced by the microheaters (through the sample chips) were performed in COMSOL (Multiphysics v5.4, COMSOL Inc., Burlington, MA) using the Heat Transfer and AC/DC Module licenses. These models were built based on the early characterization and experimental IR imaging data. A convective heat flux with ambient air (20 °C) was the primary source of heat loss on the external surface of the sample and heater assembly. Radiation Effects were not included in the final model as they were found to be negligible. Using experimental data of the sheet resistance resulting from the printing/sintering methods and known parameters of other materials, a simple model was used to confirm and estimate heating of the microheater/sample experiments performed in this work. A solid pyramid was used to simplify the many portions of the "paper chip assembly" and conform to the approximate shape of the wetted paper membrane and plastic chips used in experiments to contain samples (paper chip construction described in detail in the following chapter). A volume of water was placed inside the modified pyramid to represent the true liquid samples in experiments. Measurements of size and thickness were estimated for some materials used in the model (details in Table 2. COMSOL Model Variables Inputs & Outputs, below) but every effort was made to match real materials and conditions. Temperature-dependent resistance changes were not modeled because no resistance changes were measured during heating to relevant

temperatures in experiments. The model designates the conductive trace as a surface element and uses a "shells" method to define the conductivity of the trace based on inputs of conductivity and thickness – both of which had been previously measured during characterization. Designs were imported from their original Adobe Illustrator design files into COMSOL.

Table 2. COMSOL Model Variables Inputs & Outputs

Model Input	Source	Design 1_1	Design A
Simulation Time	-	30 min	5 hours
Terminal voltage (V)	-	1.2	1.2
Ambient Heat Flux W/(m^2K)	Manually Tuned	33	35
Trace Thickness -Shell (nm)	Experimental Data	1000	600
Trace Conductivity (S/m)	Experimental Data	2.3×10^7	2.3×10^7
Sample Dimensions (mm)	Manually Measured	7x7	10 x 10
Total Chip Dimensions (mm)	Manually Measured	15 x 15	25 x 25
Microheater Heating Region Dimensions (mm)	Manually Measured	5 x 9	12 x 10
Model Output			
Resistance (Ω)		6.6	8.5
Terminal current (A)	-	0.18	0.14
Bottom of Chip Max Temperature (°C)	-	71	43
Top of Chip Max Temperature (°C)	-	63	35
Max Sample Temperature (°C)	-	67	37
Average Sample Volume Temperature (°C)	-	63	35

3.2.3 Governing Equations

I began my model by coupling Heat Transfer in Solids with a stationary study of Electric Currents, using Single Layer Shell option in the AC/DC Module using the electric potential (V, volts) as the dependent variable, where we can solve for the electric potential on 2D surfaces in a 3D geometry. This was chosen as a more accurate method for future studies where 3D heat transfer will vary over time and space and allows for accurate modeling of the incredibly small thickness of the conductive traces (z-height of printed samples). First, the assumption of current conservation from one node to another is applied, which when combined with Maxwell's equations and our applied boundary conditions allows for discrete calculations of current density (***J*).**

The primary equations used here were then, using a stationary coordinate system and the point form of Ohm's Law:

$$\mathbf{J} = \sigma\mathbf{E} + \mathbf{J}_e \qquad \text{Equation 2}$$

where σ is the electrical conductivity (S/m) and $\mathbf{J}_e$ is an externally generated current density (SI unit: A/m^2). The electric field intensity (**E**) is defined by the relationship:

$$\mathbf{E} = -\nabla_t V \qquad \text{Equation 3}$$

Where ∇_t represents the tangential derivative along the shell, and V is electric potential.
And finally,

$$\nabla_t \cdot (d_s \mathbf{J}) = d_s Q_{j,v} \qquad \text{Equation 4}$$

Where the ∇_t represents the tangential derivative along the shell and d_s is the shell thickness, which I initially set at 1000 nm based on my Imaging and profilometry analysis of printed traces data from the previous chapter. ***J*** is the previously found current density and current source, $Q_{j,v}$ (SI unit: A/m^3) is a boundary feature at one end of the conductive trace. This current density calculation was coupled with a boundary heat source (Q_b) function which was applied to the conductive trace domain at the junction between it and the Kapton Substrate shown in Figure 3.1 below. A convective heat flux with ambient air was applied to the outer boundaries of the model components, specifically the top of all edges of the sample chip construction and the exposed top portions of the microheater on the upper left panel in the figure below.

Heat transfer between solids was applied to all appropriate contacts within the model assembly and assumes undisturbed contact between those surfaces. An insulation rule on the bottom edge where the microheater would typically be contacting a glass slide was not used as it greatly complicated the model and building an additional assembly representing the glass slide crashed the model consistently. The primary equation for heat transfer between solids in this model is:

$$\rho C_p \frac{\partial T}{\partial t} + \rho C_p \mathbf{u} \cdot \nabla T + \nabla \cdot \mathbf{q} = Q + Q_{\text{ted}} \qquad \text{Equation 5}$$

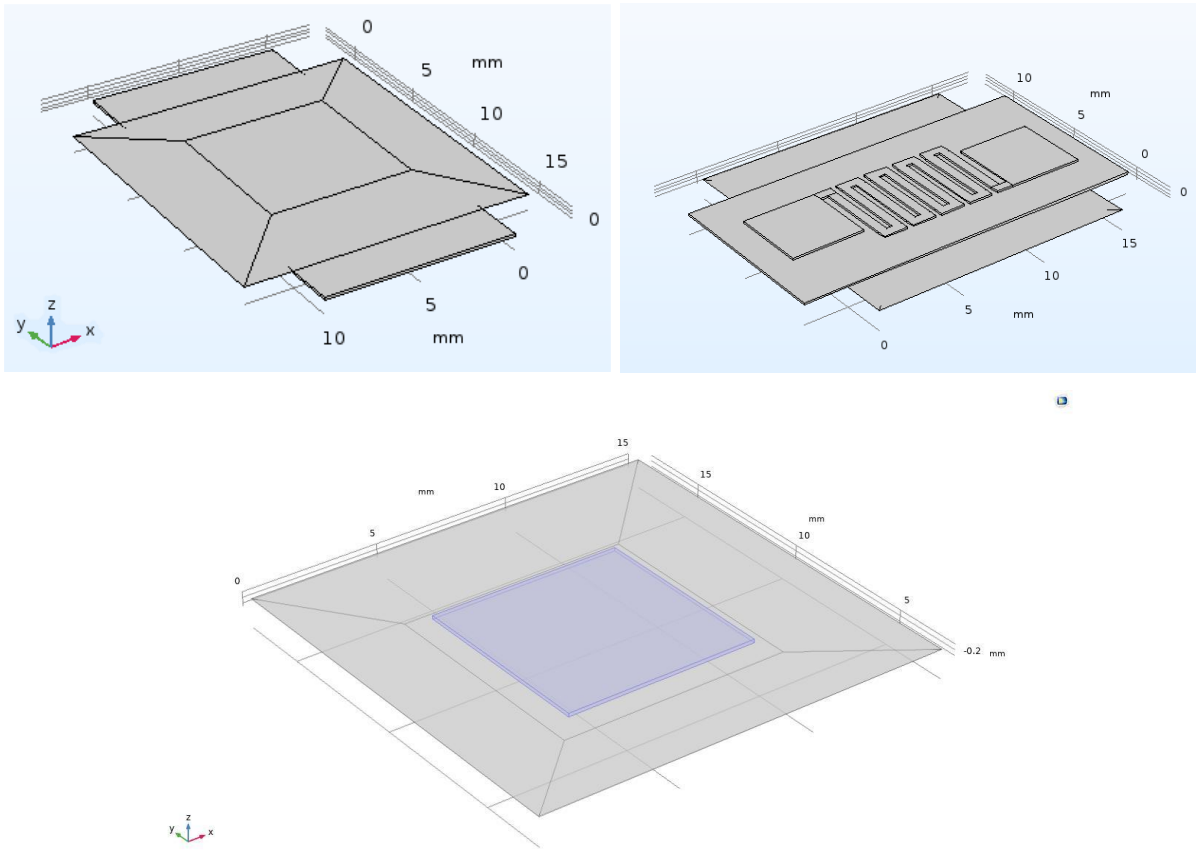

Figure 3.1. Upper Panels: Model construction of a microheater + sample chip assembly, where the conductive trace is printed on the bottom edge of the assembly. Lower: 3D construction showing liquid sample in the center of the paper chip

Where ρ is the density, Cp is the specific heat capacity at constant stress, u is the velocity vector (which applies in non-stationary models), T is the absolute temperature, ∇T is the Temperature differential and Q contains additional heat sources, (such as the coupled thermoelectric energy provided by the conductive trace), Q_{ted} is thermoelastic damping and accounts for thermoelastic effects in solids, and $\boldsymbol{q}$ is the heat flux vector by conduction – which is also described below.

$$\boldsymbol{q} = -k\nabla T \qquad \text{Equation 6}$$

where k describes the thermal conductivity, and ∇T is the Temperature differential. Because there was also a fluid component which I labeled Sample, I also included heat transfer in fluids at the interfaces appropriate within the model.

3.3 Results and Discussion

3.3.1 IR Imaging to evaluate heating consistency over time and sample area

I characterized the IR heating profiles for several power inputs in relation to overall microheater performance of the two microheater designs used in subsequent application-based experiments. Figure 3.2 (A & C) shows the average temperature over the designed heating region over time for each power input. Figure 3.2 (B & D) shows representative IR profiles of the 0.8 V input, which reveal an even heating profile along the printed traces without hotspots. This suggests that a sample in contact with this microheater would experience a diffused but even heating. The average temperature of the rectangular heating region (outlined in blue in Figure 3.2 B & D) has an average temperature of 62.7°C (max 67.2°C, min 53.0, STD 3.27) for B and an average temperature of 42.0°C (max 49.1°C, min 34.5°C, STD 3.21) for D. Because of heat dissipation through the Kapton film which has a coefficient of thermal conductivity of (0.12 W/mK)[94] and heat transfer into varying sample sizes, higher power settings may be required for a sample to reach the same temperatures shown in this IR thermal analysis. The full IR imaging results from these experiments are shown in **Figure B. 1**. These results represent the minimum power requirements for a given microheater design to reach each temperature. Based on these results, a Design 1_1 microheater with a resistance of about 5 Ohms can successfully heat a LAMP reaction using only 0.8-1.2 V when considering heat dissipation into the sample.

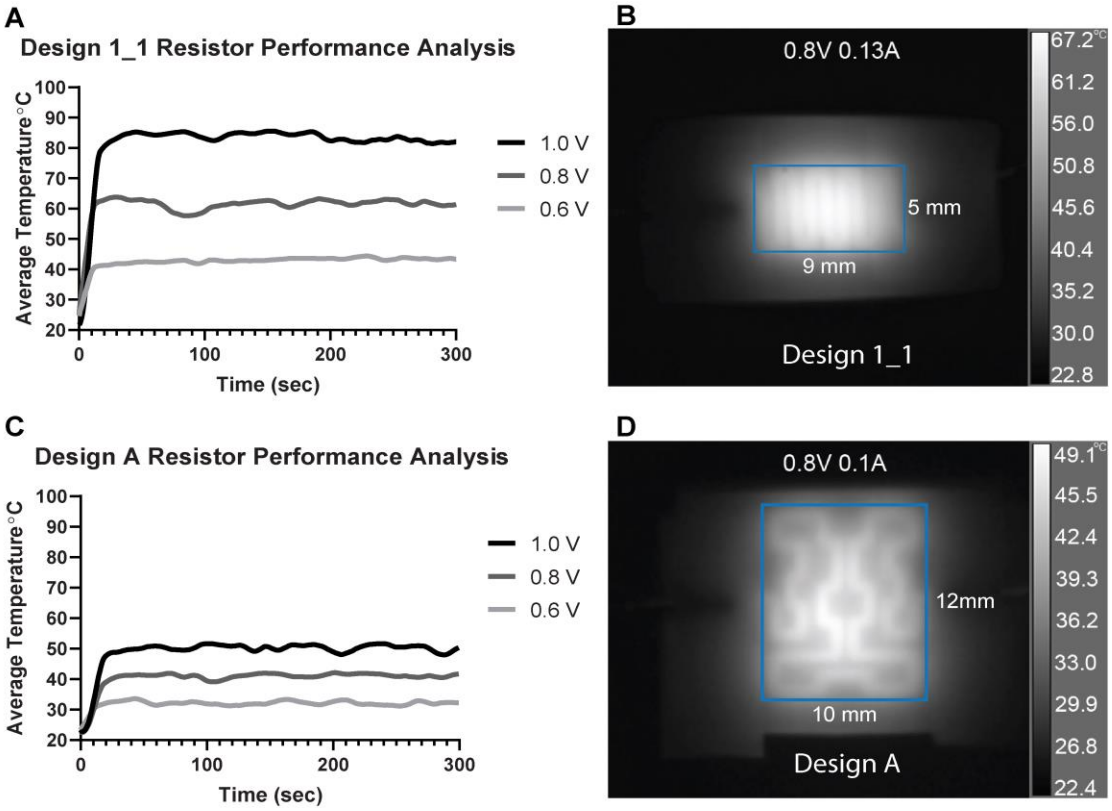

Figure 3.2. Analysis of individual microheaters Design 1_1 (5 Ohms) and Design A (8 Ohms). (A & C) Microheater temperatures over time at various voltage inputs (averaged over square heating area outlined in blue in IR images to right). (B & D) IR images of microheaters at 300 seconds of heating with higher temperatures represented as lighter and lower temperatures represented as darker greyscale intensities.

A resistance drift was not observed during IR heating tests, which was indicated by the lack of change in current draw from the initial contact with the power source during heating. Because there is no significant resistance drift associated with temperature for these resistors, I can easily maintain both temperature and power settings. Additionally, these results show that for different voltage inputs (0.6 to 1.0 volts) lower resistance microheaters produce a wider range of temperatures compared to higher resistance microheaters (Figure 3.2 A and C). In this work, a single 5.5 Ohm microheater was heated repeatedly for ten trials (15 minutes/trial) and produced heat curves with no significant difference between heating trials and standard deviations between 4.3 and 4.9 within the trials (Figure 3.3). The summary and full analysis of this data is shown in **Table B. 1** and

Table B. 2. Another important result to note is that this microheater was able to repeatedly reach an average temperature of 65°C over the 9 x 5 mm heating area within less than 1 minute of initiation and maintain 65-70°C using steady power settings of only 220 mW (1.1 V, 200 mA). This is critical to sample heating at the POC because time is one of the primary factors clinicians use to asses diagnostic usability.[95] During these IR imaging sessions, the conductive traces would quickly heat up as soon as electrical contact was initiated but the Kapton substrate, being a thermal insulator slows the time for heat dissipation slightly. Overall, these results show that the microheaters are highly consistent between heating trials, are reusable with no resistance shift resulting from the microheaters being heated, and can rapidly reach high temperatures needed to operate POC diagnostics.

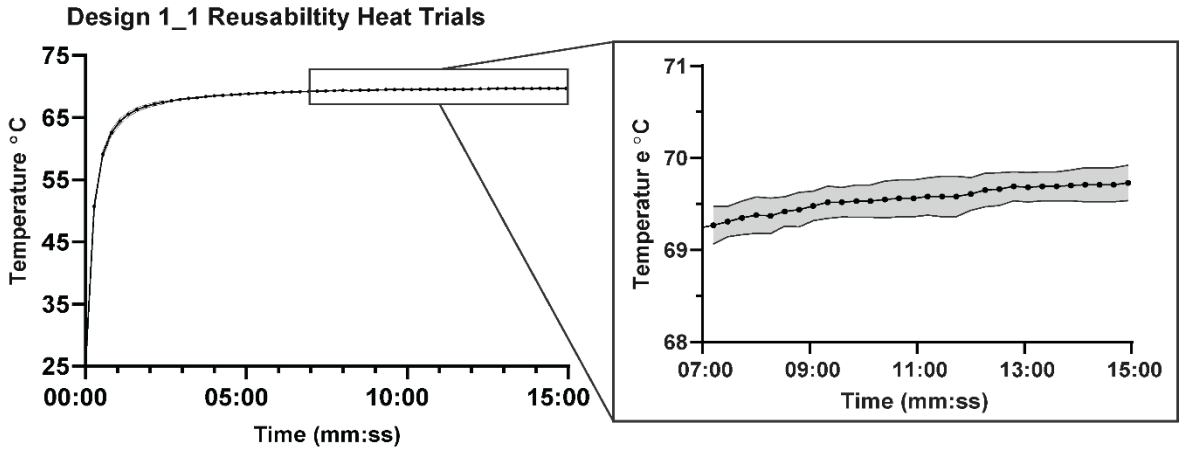

Figure 3.3. Average of 10 trials of repeated heating of a single 5.5 Ohm microheater from Design 1_1 (left) and detailed view (right) grey shaded region represents variability (SD).

3.3.2 COMSOL Multiphysics Modeling of Microheaters Compared to IR Imaging Results

I performed heat transfer modeling evaluations in COMSOL to test the heating profiles of the microheaters to ensure my model would subsequently be accurate when I later modeled the sample chips used in the subsequent application experiments discussed in Chapter 4. I first established congruency between the model and the IR imaging we just discussed, focusing only on the heat output of the conductive trace and its heating of the Kapton substrate. I tested the model with the same voltage inputs used in the initial IR heating experiments and confirmed that the model produced comparable outputs under the modeled conditions I established (which included

modeling time of 300s to match the IR experiment). As you can see in Figure 3.4, the temperature gradient and overall profile of both heat maps are incredibly similar and show maximum temperature values within 0.6°C. Most importantly, the average temperature of both 9 x 5 mm heating zone in the COMSOL model was 63.5°C which is very close to the measured 62.7°C average temperature from the IR imaging. Unfortunately, in the image on the left the "tails" on either side of the heater are obscured by electrical tape holding the electrodes and heater in place which may have slightly dissipated some of the heat while the model clearly shows these. It does not appear that the ends of the heaters are of great concern as the majority of samples will be experiencing heat transfer from the center and so long as there are no print defects, the highest temperatures do appear to occur in the centermost serpentine turns in either the IR imaging or the model. I ran the model under these conditions for both Design 1_1 and Design A microheaters, each at the three voltage settings I used in the IR experiments. The results for each of the model runs were all congruent within less than 3°C (not shown) and showed that the model very closely matched my experimental data. Based on these model results I decided to accept this model and begin modeling paper chip samples containing liquid volumes.

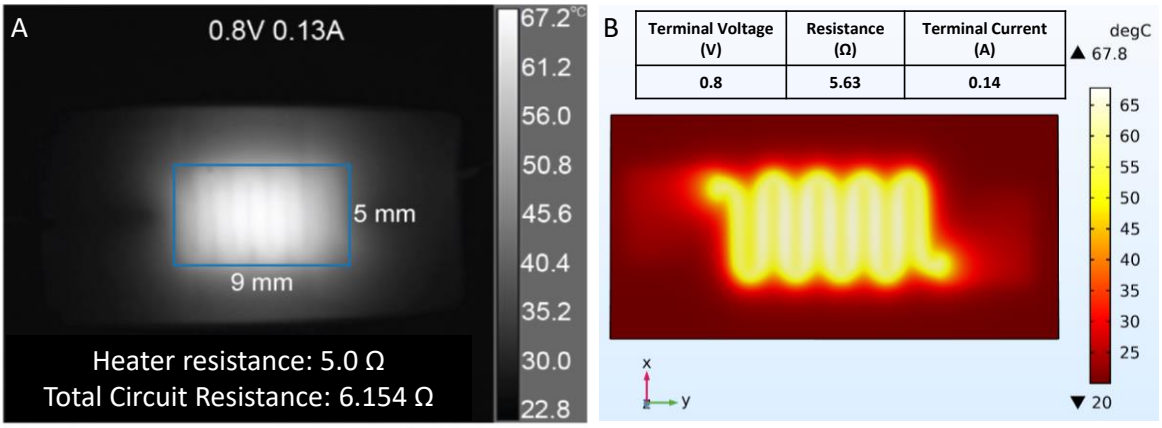

Figure 3.4. COMSOL Model results compared to IR imaging show acceptable congruency for continued modeling of sample chips.

3.3.3 Modeling of experimental samples

I anticipated that with heat loss and dissipation through the sample, the true temperature of each heater would need to be slightly higher than the desired sample temperature. With this in

mind I decided to investigate what temperatures the microheaters would need to be in order to achieve the desired sample temperature and what voltage input that would require. After tuning the model, I found that a voltage input of 1.2V and the resulting 0.18A current would produce results closest to what would be needed to incubate a LAMP assay for 30 minutes. The results of these model inputs are shown in Figure 3.5 below.

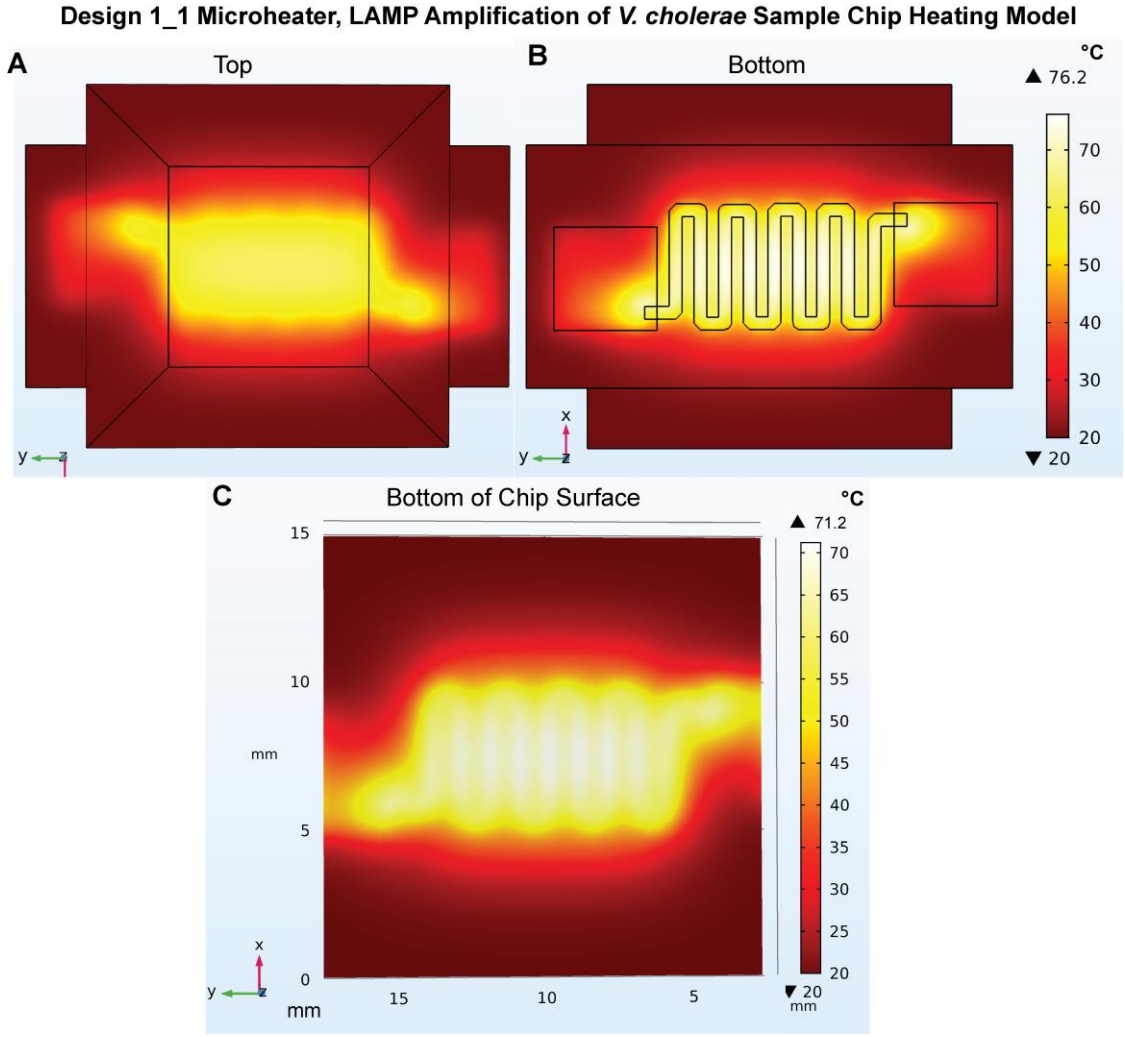

Figure 3.5. COMSOL Model of Design 1_1 Microheater and LAMP sample assembly, showing heat distributions for the entire outer surface (A and B), the bottom surface of the sample chip (in contact with the heater) (C). Each figure intensity (color gradient) is specific to the temperature scale to the right of each evaluation, please note that the scales are different for each.

As you can see, if the desired temperature for the sample is 65-70°C, it might be concerning to see a maximum microheater temperature as high as 76.2°C (Figure 3.5B). However, when we focus in on just the liquid volume portion of the sample chip shown in Figure 3.6, we see that the liquid sample at the center of the chip has an average volume temperature of 63°C, with a maximum surface temperature of 67 °C. Similarly, when I modeled Design A heating an *E.coli* sample (Figure B.2), the temperature of the microheater surface had a maximum of 43 °C, the surface of the sample chip in contact with the microheater was 40.6°C (maximum), but the liquid sample at the center of the chip (Figure 3.6. C & D) had temperatures ranging from 28.1 °C (at top outer edge) to 37.2 °C (at lower outer edge), with an average volume temperature of only 35 °C.

These models demonstrate the range of temperatures produced within the liquid samples using microheater designs A and 1_1 as shown in Figure 3.6. These results show that the heat distribution through the liquid volume is largely uniform for the portions where the sample is within the bounds of the heating zone when heating with Design 1_1, with the majority of the volume being within the desired temperature range. These results also suggest that a slightly wider design with a heating zone to accommodate the 7 mm x 7 mm PES sample could produce more accurate results. However, while Design A covers the larger 10 × 10 mm area more effectively, the inconsistencies of the trace distribution may cause unnecessary temperature inconsistencies. My colleague, Dr. Elizabeth Phillips performed IR analysis of wax valves heated with a commercial polyimide thin film heater and found that because of the distance between the heating elements in these heaters, the orientation of the wax valve relative to the patterned direction of the heating elements, the fluid flow produced inconsistent heating across the wax valve if the orientation was not parallel to the valve. [96] The thermal-spatial concern is of course application dependent, but with such a high resolution printing method it is probable that an adequate design can be achieved for high-fidelity heating if necessary.

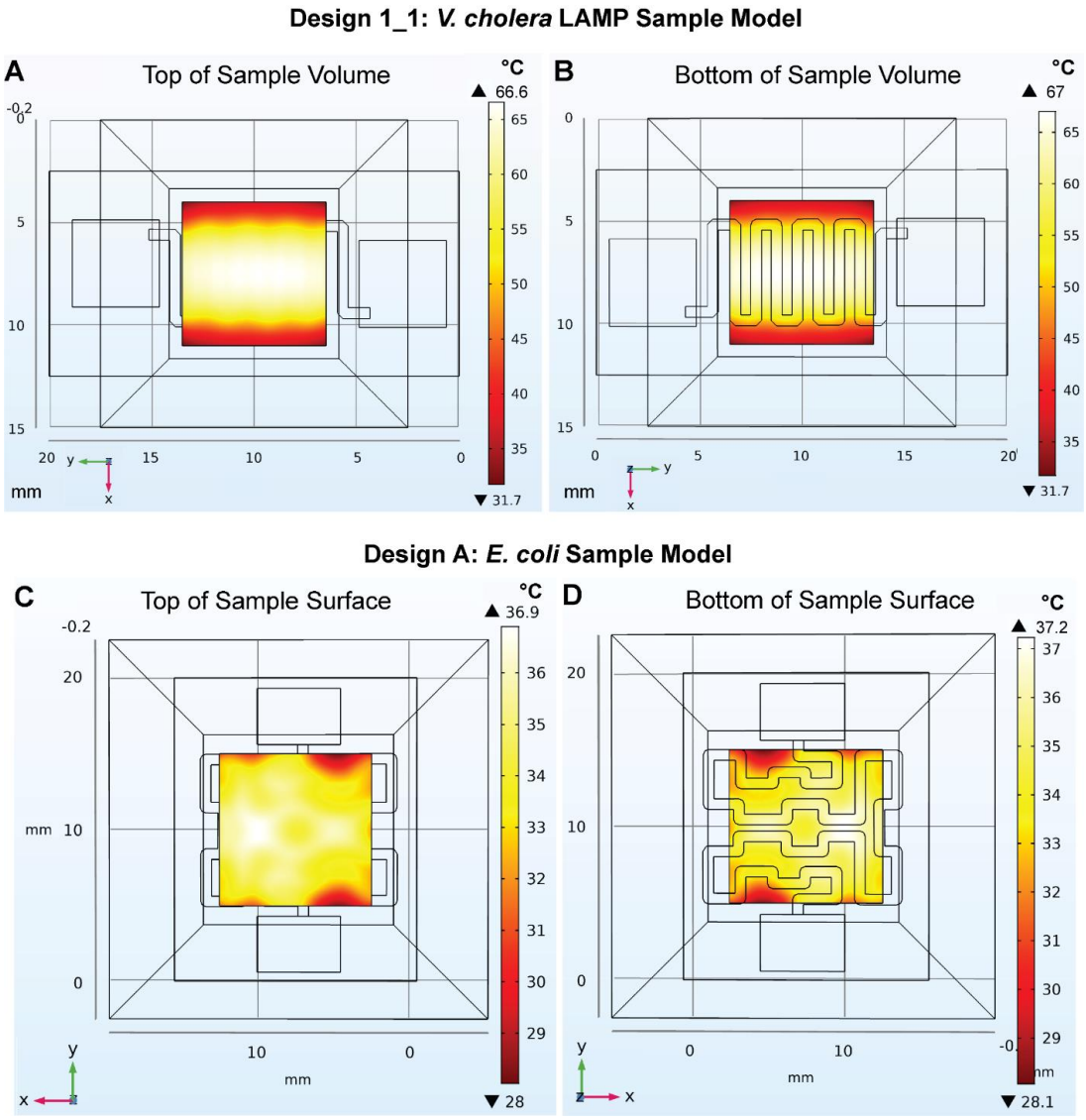

Figure 3.6. COMSOL Model results of liquid sample temperature distributions. A and B represent the top and bottom of the sample heated by design 1_1 in the V. cholera LAMP experiments while C and D represent design A heating the *E. coli* sample.

3.3.4 Conclusions and Future Directions

This computational investigation was a valuable tool that showed Design A produced a much less consistent heating area than Design 1_1. While this reduction in uniformity was expected given the inconsistent spacing between the traces in Design A, the extent to which the model showed this could affect the sample was more extreme than anticipated. This model could

be useful for evaluating future designs prior to the printing stage, especially when testing trade-offs between low-resistance designs and large surface area needs. The model does not address heat build-up that may have occurred in the enclosed case format used in later experiments. However, during experiments there is imperfect contact between the sample chip and the microheaters due to thermistors used to record temperatures on the top and bottom of the sample chip. With all limitations considered this model is a good representative of best-case heat transfer between the microheater and sample chip and does show that monitoring the temperature of top and bottom sample chip surfaces would be an acceptable method for estimating the temperature of the liquid reaction during proof-of-concept experiments or during device integration. While it might at first make sense to create designs conforming to the *exact* dimensions of the intended samples, the best practice for future work could include a tolerance factor where the size of the heating zone is slightly larger than the sample size to allow for misalignments during actual use. In the case of enclosed heating where buildup is highly likely, microheater temperatures should be kept closer to ideal sample temperatures and increased incubation time may be necessary to allow for heat dissipation into the sample. Further modeling of these dynamics could improve microheater implementation at the POC and aid in device integration.

4. INTEGRATING INKJET PRINTED MICROHEATERS FACILITATE IMPROVED POINT-OF-CARE ISOTHERMAL SAMPLE INCUBATION FOR RAPID DIAGNOSTIC PLATFORMS

Parts of this chapter are reproduced from Ref. [70] from the Open Access Journal *Analyst*, and Ref [39] from the Open Access Journal *Lab on a Chip*, both published by the Royal Society of Chemistry.

4.1 Rationale

Fully integrated rapid assays that are suitable for POC use have been touted as the solution to a growing need for both low-resource and personalized health care options all over the world. Highly efficient microheaters would enable miniaturization of devices for more economic and effective heating with high temperatures and sustained incubation. To determine if my microheaters can meet their intended uses, I performed several proof-of-concept experiments to test the practical use and limitations of microheater integration into a portable, battery-powered platform. Here, I demonstrate both bacterial culture at 37°C, and isothermal nucleic acid amplification at 65°C using these microheaters and a simple, constant power source. For these experiments, I chose to establish a range of both surface and interstitial temperatures that would be acceptable based on the COMSOL Models previously discussed and early experimental results. I also discuss and analyze the integration and performance of my microheaters in a sample-to-answer device (Microfluidic Rapid and Autonomous Analysis Device (microRAAD)) for detection of HIV viral nucleic acid amplicons, which was developed in collaboration with many other members of the Linnes lab. This integrated platform demonstrates a critical turning point in this work because it can realistically be used at the POC due to being both fully automated and powered by a common cell phone.

4.2 Materials and Methods

4.2.1 Thermal Sensing during sample incubation

A 1550 DC Power Supply (BK Precision, Yorba Linda, CA) each experiment while a K-type temperature sensor read by an RDXL4SD Thermometer (Omega Engineering Inc., Norwalk, CT) taped to the top edge of the center of the microheater which was then covered with Styrofoam

and enclosed in the plastic box. When paper chip-based samples were introduced for *E. coli* and V. cholerae LAMP incubations, the thermocouples were taped to the top and bottom edges of the samples to assess the sample temperature more accurately.

4.2.2 Incubation and Detection of *E. coli* via Resazurin Colorimetric Growth Assay

E. coli samples were grown in LB in an incubator shaker at 200 rpm at 37 °C overnight. Cultures were diluted in LB media to an OD600 of 1, (Ultrospec 10, Biochrom, Cambourne, UK) representing 8×10^8 cells per mL of *E. coli* as determined by counting colony forming units of serially diluted samples. 5 µL of 10X PrestoBlue™ was added to 45 µL samples of serial dilutions of *E. coli* in LB. 50 µL samples were placed on 10 × 10 mm glass fiber pads and the devices were sealed with 25 × 25 mm clear adhesive laminating sheets. One set of dilutions was kept at room temperature (protected from light exposure) and another placed in a microbiology incubator at 37 °C. Negative controls containing 45 µL of LB and 5 µL PrestoBlue™ were included in each batch.

A 10^4 colony-forming unit (CFU) per mL sample was prepared as above (final concentration 9 CFU μL^{-1}) and individually incubated with our "design A" microheater (dimensions: 1x1 cm, discussed in previous chapter) heated by the 1550 DC power supply for 16 hours (two identical controls were also placed in the lab-grade incubator and left covered at room temperature. Two K-type temperature sensors read by were placed on the top and bottom faces of the sample chip and covered with tape to provide better sampling of the paper chip temperature. In later experiments, an opaque box, a battery and glass slide were secured and the Styrofoam insulation for the sample was cut to match the size of our incubation chips (schematic shown in Figure 4.1).

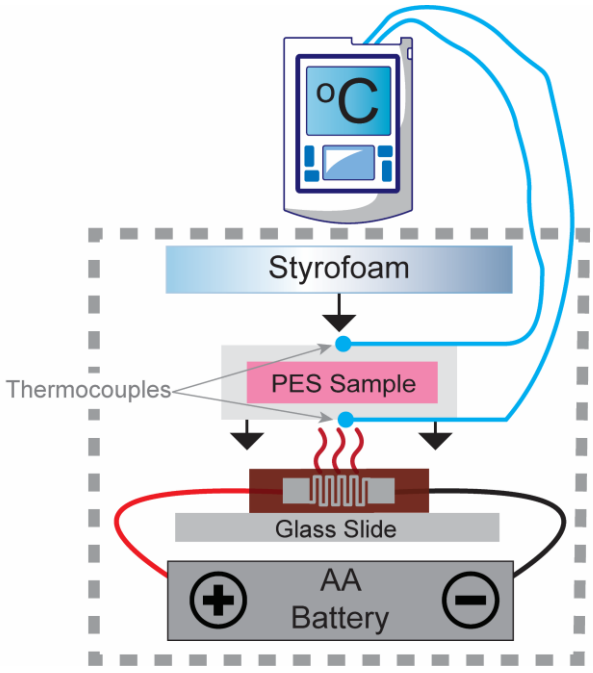

Figure 4.1 Schematic of sample incubation

An additional test was done with a 10^6 CFU mL^{-1} sample of *E. coli* prepared as above (final concentration 900 CFU μL−1). A single rechargeable AA battery (AA 2600 mA h 1.2 V NiMH) powered the microheater setup inside an opaque plastic container for 6 hours. This higher concentration was used for simplicity of the repeat and is comparable to other publications showing proof-of-concept detection with resazurin.3 Following incubation, all samples were scanned with an Epson V850 Pro Scanner (Model J221B, Epson America Inc., Long Beach, CA) with the same scan settings. The Red and Blue channel average intensity color values of all samples were measured using a MATLAB script[97] which were then used to calculate the ΔRedBlue (ΔRB) value detailed in $\mathbf{\Delta RB} = \sqrt{(\boldsymbol{R_1} - \boldsymbol{R_2})^2 + (\boldsymbol{B_1} - \boldsymbol{B_2})^2}$ Equation 7. These values were then graphed and compared.

$$\mathbf{\Delta RB} = \sqrt{(\boldsymbol{R_1} - \boldsymbol{R_2})^2 + (\boldsymbol{B_1} - \boldsymbol{B_2})^2} \quad \text{Equation 7}$$

4.2.3 Nucleic Acid Amplification in Paper Methods

V. cholerae cultures were grown in LB media overnight at 37°C using a miniature incubating shaker at 300 rpm (Thermo Fisher, Waltham, MA). Cultures were diluted in LB media to an OD_{600} of 1, (Ultrospec 10, Biochrom, Cambourne, UK) representing 6 x 10^8 cells/mL of *V. cholerae* as determined by counting colony forming units of serially diluted samples. A LAMP assay developed by Dr. Taylor Moehling was performed to amplify DNA from *V. cholerae* at a concentration of 4 x 10^5 cells/mL (~10^4 cells/reaction, where 1 reaction is 25 uL). LAMP samples were incubated in 7 mm x 7 mm PES membranes with 0.22 μm pores, covered on both sides with 10 mm x 10 mm PET film, and sealed with 15 mm x 15 mm adhesive laminating sheets to prevent evaporation during heating. The no template negative control consisted of molecular biology grade water rather than template (Thermo Fisher Scientific, Waltham, MA). All samples were incubated at 65°C on top of a single resistive microheater (Design 1_1) and insulated with a thin Styrofoam square for the 30-minute amplification assay (Figure C.1). The entire circuit and sample were enclosed in a plastic box to limit heat loss via convection. Positive and negative control samples were amplified in an Applied Biosystems 7500 Real-Time PCR System (Foster City, CA) for 30 minutes at 65°C as gold standard heating controls. The negative sample was incubated the same way as the positive samples but was done separately to avoid contamination. Power was supplied

to the microheater via a freshly charged battery (AA 2600 mAh 1.2 V NiMH, Tenergy, Fremont, CA). This same battery was used for subsequent heating sessions, providing power for four ~30-minute heating sessions after one charge session.

The temperature of the sample was monitored for the entirety of the assay to ensure that the sample remained in the temperature range of 60-70°C in which the *Bst* 2.0 polymerase has 100% activity.[91] Two K-Type temperature sensors read by an RDXL4SD Thermometer (Omega Engineering Inc., Norwalk, CT) were placed on the top and bottom faces of the sample chip. Each LAMP reaction was heated for 30 minutes, starting when the bottom face of the sample chip reached 65°C, and was continuously monitored for overheating. The microheater was in use for approximately 35 minutes for each session. The PES membranes were place in microfuge tubes and centrifuged at 2.0 rpm for 60 seconds to release the amplicons from the PES membrane. After centrifugation, 5 µL of amplicons were added to a commercial lateral flow immunoassay (LFIA) (Ustar Biotechnologies, Hangzhou, China) for analysis. The LFIAs were scanned at least 30 minutes after initial sample addition using an Epson V850 Pro Scanner. The test band was quantified using a custom MATLAB script that averages the grey-scale pixel intensity of the test band and subtracts the average background pixel intensity 25 pixels below the test band[97].

4.2.4 Selected Methods from Whole Platform Development Microfluidic Rapid and Autonomous Analytical Device (microRAAD) to Detect HIV from Whole Blood Samples

My colleague, Dr. Orlando Hoilett, designed a microcontroller that we programmed to initiate and monitor each heating occurrence using a proportional integral differential (PID) algorithm for maintaining temperature of the heating zones within the user-specified set points (65°C for the LAMP amplification and 80°C for each wax valve), based on the microfluidic design established by Dr. Elizabeth Phillips. We integrated Design 1_1 microheaters, printed in triplicate on a single sheet of Kapton film, with an exact separation distance of 10mm from center to center, adhered to the backside of the µPAD, aligned with the two valves and amplification zone, and faced such that the silver traces would contact the pogo pins of the temperature control circuit inside the plastic housing. Two plastic brackets were slid over the acrylic lid and plastic housing to ensure proper contact within microRAAD. Additional details for experiments can be found in Ref [39].

4.3 Results and Discussion

4.3.1 Microheater Incubation of *E. coli* via Resazurin Colorimetric Growth Assay

During cell growth, *E. coli* produce nicotinamide adenine dinucleotide (NADH). NADH catalyzes the reduction of Resazurin (the active compound in PrestoBlue™) to Resorufin, resulting in an easily identifiable color shift from blue to pink[98]. This well-known phenomenon was used to indicate and assess the incubation of *E. coli* in trials of DC and battery-powered incubations with microheater Design A. No resistance drift was observed for the entirety of the 16-hour incubation, indicated by the consistent current given by the DC power source. Figure 4.2A shows the consistent temperature profile which also demonstrates that the sample reached 37°C within 10 minutes of initiation. Based on this experiment, it was estimated a single rechargeable AA NiMH battery (2600 mAh, ~1.2 V) would be able to comfortably power an 8.5 Ohm microheater, consuming 120 mA for about 17 hours and is expected to use 80% of the total battery capacity. A 6-hour incubation was selected to enable detection of 10^6 CFU/mL *E. coli* in one afternoon using the fully charged AA battery and 8 Ohm Design A microheater. This higher concentration was used for simplicity of the repeat and is comparable to other publications showing proof-of-concept detection with Resazurin[56]. This experiment produced a similarly consistent

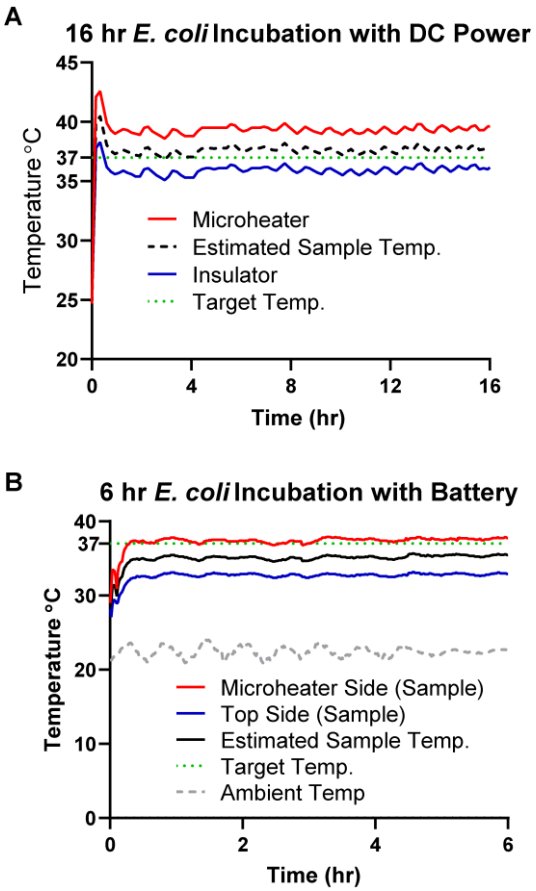

Figure 4.2. *E. coli* microheater incubations. (A) 16-hour constant incubation of *E. coli* with 1550 DC Power Supply with 8.5 Ohm microheater. The power settings were initially set to 143 mW and then was reduced to 120 mW and maintained for the entire 16 hours, using ~1920 mWh (milliwatt hours) for the entire incubation. (B) The E.coli incubation was successfully heated with Design A (8 Ohms) powered by a single rechargeable NiMH AA battery supplying an average current of 145 mA (1.2 V, power~174 mW), using an estimated 1044 mWh (milliwatt hours) for the 6 hour incubation period.

temperature profile (Figure 4.2B) to the DC-powered incubation. Even without adjustable battery power, the microheater maintained an average temperature of 37.4°C and average estimated sample temperature of 35°C for the entire 6-hour incubation period.

As seen in **Figure 4.3**A, the 10^6 and 10^4 CFU/mL (final concentrations 900 CFU/µL and 9 CFU/µL) sample pads were all uniformly pink after microheater incubation, indicating reduction of Resazurin throughout the sample. In contrast, samples left at room temperature and all negative controls remained visibly dark blue. This proof-of-concept experiment suggests that many other novel designs and heating profiles could be quickly produced using our methods. The quantitative colorimetric analysis shown in Figure 4.3B revealed that the microheater incubations produced comparable bacterial growth to the lab-grade incubator results, meanwhile the samples left at room temperature had very little growth. This indicates that the microheaters are able to effectively heat the samples to efficiently grow bacterial samples for culture-based diagnostics. For regions with inconsistent power grids and areas remote from specialized laboratories, portable culture devices could be incubated by these microheaters and could allow for the assessment of food and water quality. These microheaters could be easily combined for existing culture devices, such as those by Deiss *et al.* and Elavarasan *et al.* as well as assessment of antibiotic resistance for the characterization of infectious diseases in these regions[56,99].

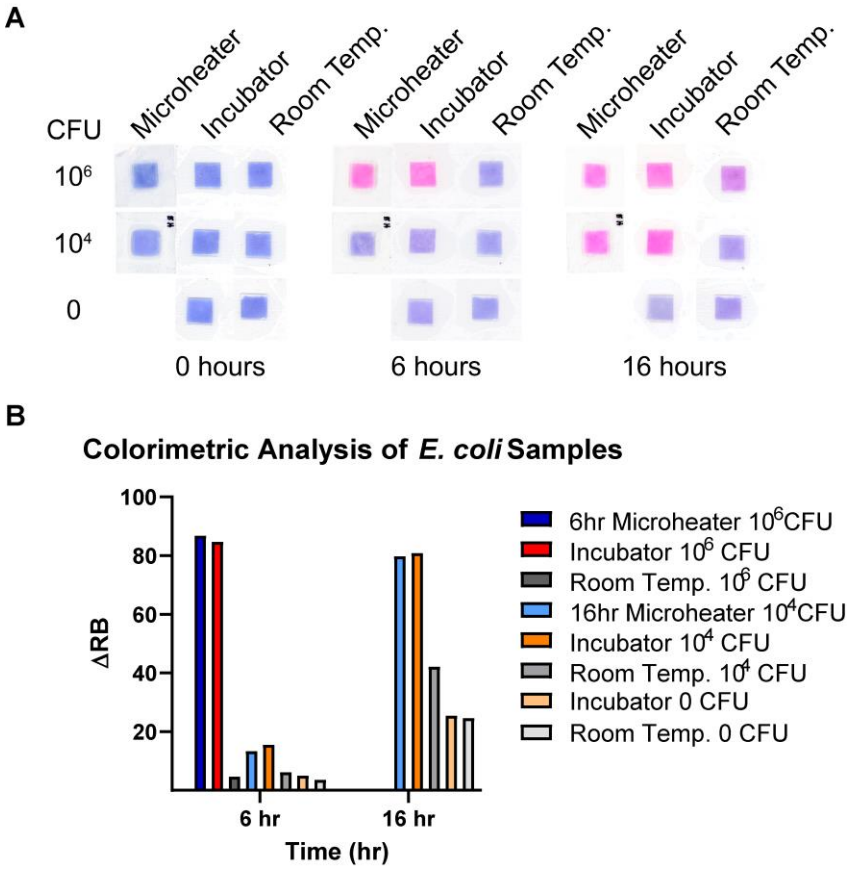

Figure 4.3. (A) Colorimetric analysis of the red and blue channel intensities at different time points were summarized into ΔRB values (intensity change from Time=0) to assess the growth of the incubated samples for both the 6- and 16-hour microheater trials. (B) Samples from controls and trials showing intense color change from Resazurin reduction. **Figure C. 2.** Detection of serial dilutions of *E. coli* using PrestoBlue™. LOD of 37°C after 6 hours is 105 colony-forming unit (CFU). After 16 hours limit of detection (LOD) of 37°C is 101 CFU. LOD of room temperature samples was 106 CFU after 16 hours. Design A microheater (8 Ohms) was used for these trials. Color change for microheater incubations closely match incubator results while room temperature samples did not. Incubator and microheater performance data suggest the microheater incubation could have a similarly low LOD of 101 CFU.shows all control concentrations.

4.3.2 Microheater Incubation for the detection of V. cholerae via LAMP Amplification

The entire circuit and sample assembly was enclosed in a plastic box to limit heat loss via convection. Positive and negative samples were amplified in an Applied Biosystems 7500 Real-Time PCR System for 30 minutes at 65°C as gold standard heating controls. The NTC was incubated the same way as the positive samples but was done separately to avoid contamination.

Power was supplied to the microheater via a freshly charged battery (AA 2600 mAh 1.2 V NiMH, Tenergy, Fremont, CA). This same battery was used for subsequent heating sessions, providing power for four ~30-minute heating sessions.

The temperature of the sample was monitored for the entirety of the assay to ensure that the sample remained in the temperature range of 60-70°C in which the *Bst* 2.0 polymerase has 100% activity[91]. Two K-Type temperature sensors read by an RDXL4SD Thermometer (Omega Engineering Inc.) were placed on the top and bottom faces of the sample chip. Each LAMP reaction was heated for 30 minutes, starting when the bottom face of the sample chip reached 65°C, and was continuously monitored for overheating.

With these methods, I was able to successfully amplify *V. cholerae* DNA via a LAMP assay on the PES chip heated by a 5 Ohm 1_1 Design microheater, indicated by the characteristic positive test band on the LFIAs in Figure 4.4A. The test band intensity analysis (Figure 4.4B) shows comparable signal between the positive and negative controls heated by the real time machine and the positive and negative samples heated by this microheater. The average temperature of all four incubations (Figure 4.4C) was 67°C (69°C, 67°C, 66°C, 66°C in order of negative, positive

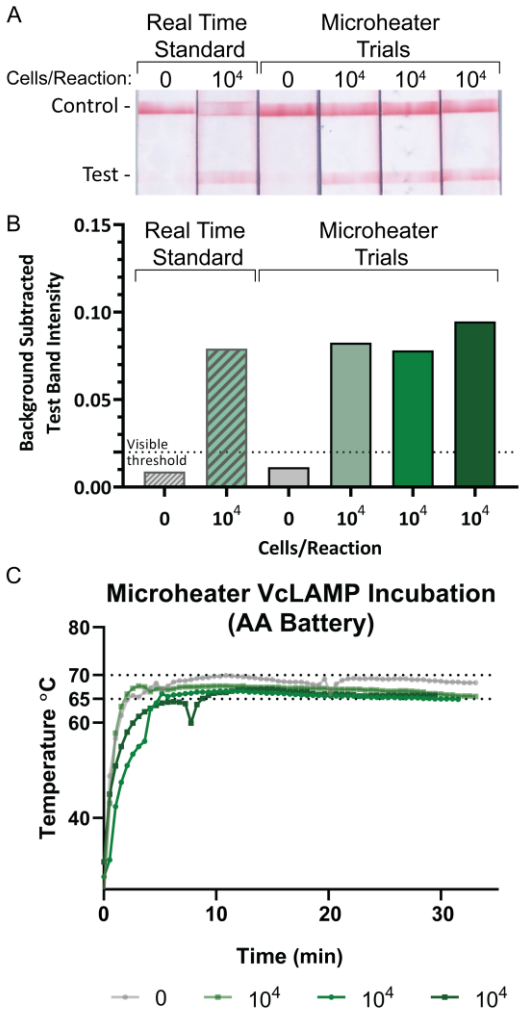

Figure 4.4. V. cholerae LAMP Sample Incubation. (A) Commercial LFIAs verifying LAMP amplification of V. cholerae DNA from whole cells with positive and negative heating controls amplified in the Real-Time machine and experimental samples amplified with a 6.4 Ohm microheater (Design 1_1). (B) Quantified background subtracted test band intensities of the LFIAs showing comparable visual signal between the heating controls and microheater samples. (C) Temperature profiles of the recorded microheater performance during each ~30-minute incubation.

1, positive 2, and positive 3, respectively) over each 30-minute assay which fell well within our target temperature range of 65-70°C. The serpentine microheater (Design 1_1) in the *V. cholerae* LAMP incubation study had a resistance of 6.4 Ohms and was heated with the same rechargeable NiMH AA battery for all four incubations. The underside of the sample (in contact with the microheater) reached 65°C within 2-5 minutes of initiation for the first three samples, and above 65°C within 9 minutes of initiation for the last sample, which had a poor contact and was manually adjusted near the 7-minute mark. After the initial ramp-up time each microheater stayed at or above 65°C and below 70°C. LAMP reactions are functional at temperatures as low as 52°C[100] but this *V. cholerae* LAMP assay is most efficient and has the fastest amplification rates at a temperature of 65°C[101]. Despite some poor electrical connections and the same rechargeable NiMH AA battery being used for all 4 experimental incubations, the microheater maintained temperatures within the 65-70°C incubation window for most of the incubation time.

4.3.3 Reporting Results from Whole Platform Development Microfluidic Rapid and Autonomous Analytical Device (microRAAD) to Detect HIV from Whole Blood Samples

Integration of microheaters into a portable, low-cost, automated platform presented many logistical challenges due to the many steps in the process that required specific timing and temperature settings to be successful. We successfully assembled and tested this fully-integrated sample-to-answer platform (Figure 4.5) that leverages paper membranes' wicking abilities and size discriminating pores to a) separate HIV viral particles from human blood cells, b) amplify RNA from the viral particles using pre-dried RT-LAMP reagents that target the highly conserved *gag* gene of HIV-1, and c) automatically transport RT-LAMP amplicons to an integrated LFIA for simple, visual interpretation of results within 90 minutes of sample application.[39]

The Design 1_1 microheaters provided even heating of the amplification zone with an average resistance of 5 Ohms and required an average of 240 mW to reach 65°C, the temperature necessary for the RT-LAMP assay. The heating elements used to actuate the wax valves also had an average resistance of 5 Ohms and heated to 80°C using an average of 440 mW. The insulation required to maintain steady heating was provided by an acrylic lid and plastic housing pictured in Figure 4.5 (A).[39] Heating integration was initially difficult to tune due to coding errors that set the initial voltage input to the microheaters too high. This caused the microheaters

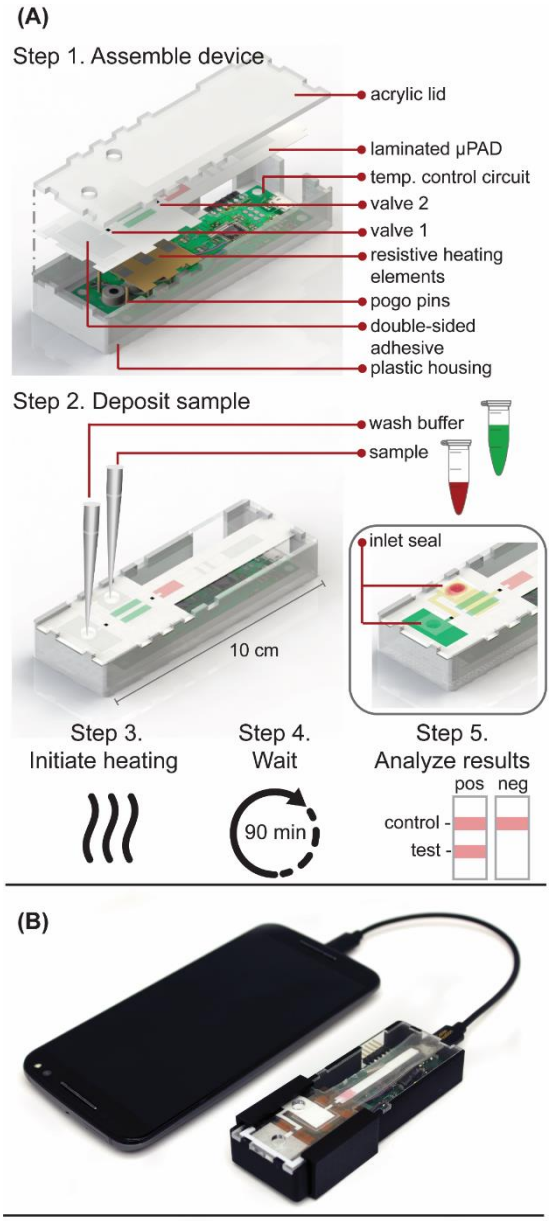

Figure 4.5. **(A)** Schematic of microRAAD for HIV testing. **(B)** Photo of microRAAD connected to phone to power the temperature control circuit.[39]

Reproduced from ***Lab Chip***, 2019,**19**, 3375-3386

to begin heating well above the temperatures for the LAMP amplification, sometimes jumping as high as 100°C. This phenomenon not only deactivated the dried LAMP reagents in the amplification region, but also occasionally caused the fluid bound by the wax valves to exceed the melting temperature of the wax, resulting in the valves opening prematurely. We corrected this problem by reducing the initial input power setting of the code and improving the proportional–integral–derivative (PID) control loop to be more responsive and able to drop to the necessary voltage more quickly. The most important factor we adjusted was the sampling frequency, which was reduced from 150 milliseconds to 50 milliseconds. This trend is observed in Figure 4.6 where, once the sample is loaded and MicroRAAD is initiated, the microheater positioned directly beneath the LAMP reaction zone is heated to 72°C by an initial voltage of 2.36V which rises to 3.2Vand then rapidly drops to less than 2 volts for the remaining incubation period. This ramp up and subsequent drop occurs within just a few seconds and is useful for ensuring any resistance differences in the microheater is accounted for by the microcontroller; making batch-to-batch resistance variations less concerning than previous experiments not aided by a microcontroller. Similarly, during the second phase of automated heating the two wax valves are both initiated simultaneously with an initial voltage of 3.28V which is held slightly longer and then dropped to an average of 1.9 volts to maintain 80°C for two minutes. It is important to not here that these temperatures represent the IR sensors detecting the temperature of the bottom surface of the microheater itself. As we saw in the COMSOL models from the previous chapter, the surface temperature of the microheater does not represent the true sample temperature which is likely both much slower to reach elevated temperatures and likely at least several degrees below the microheater temperature for quite some time before heat buildup occurs within the enclosed space. Having the microheaters briefly reach temperatures at the upper limit of our desired temperature range is intended to speed up the overall sample incubation and did not appear to negatively affect the assay outcomes once the early issues with the microcontroller were resolved.

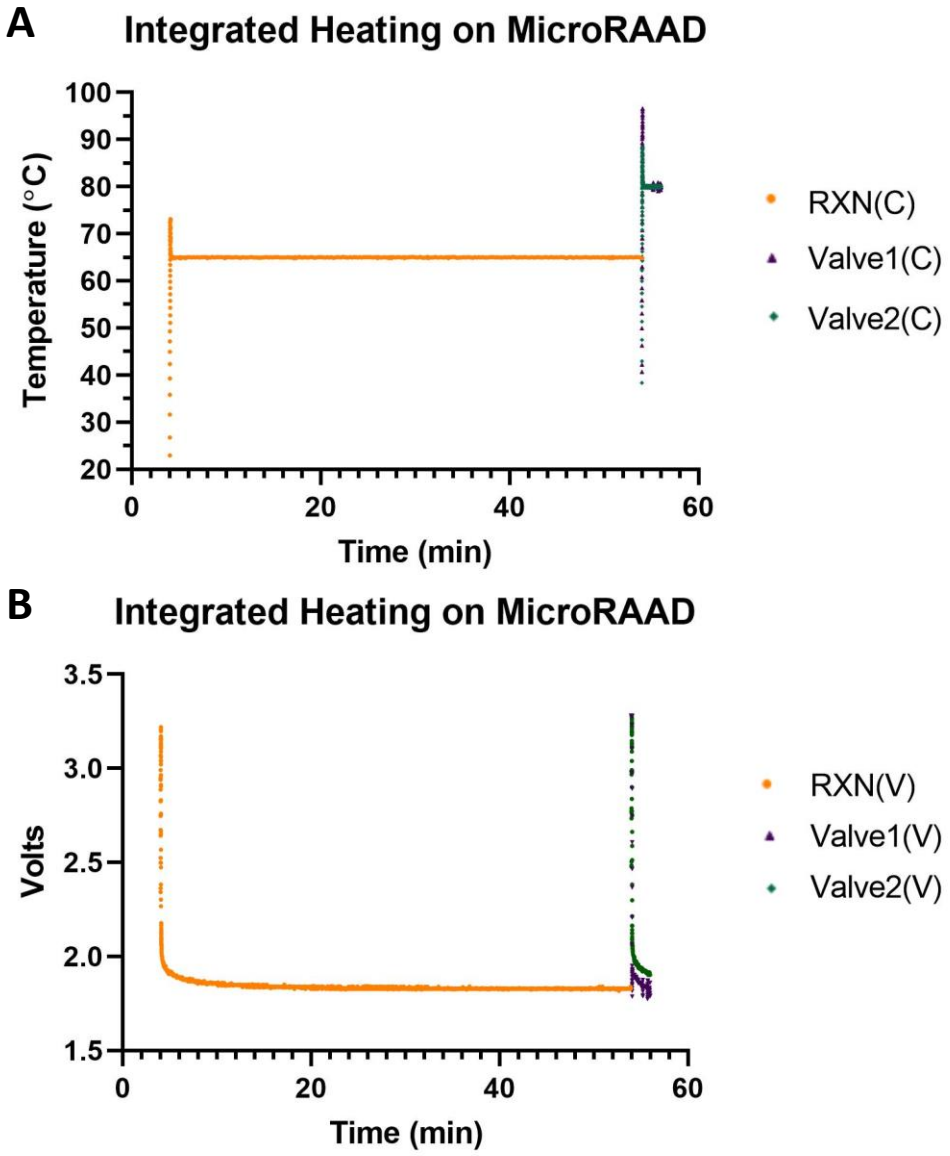

Figure 4.6 Temperature and Voltage data recorded from MicroRAAD integrated platform during experiment with dried LAMP reagents and spiked water sample, powered by computer USB for recording purposes.

When the integrated device was performing as intended, some of the fluid in the amplification region would often evaporate to the top of the laminating seal, though it did not appear to greatly affect the overall assay performance and droplets did appear to be well contained by both the laminate and the wax valves. Because both heat and liquid can degrade adhesives, it will be important to ensure adequate edge space between wetted microfluidic components and the

outer edge of the laminate to maintain the integrity of future assays and reduce the likelihood of sample evaporation, reaction inhibition due to adhesives, or some other malfunction. Additionally, Dr. Elizabeth Phillips noted that assay steps necessitating higher temperatures (such cell lysis or enzyme deactivation) may require additional modification of spacing between heating regions and wax valves to ensure platform reliability.[102] This spacing sensitivity adds strength to the necessity of proper microheater design. It would not be possible to have efficient capillary driven flow with multiple heating regions using the commercially available heaters discussed previously.

In the final implementation, the temperature control circuit was powered through a USB port using a USB On-The-Go (USB OTG) enabled cellphone (Samsung Galaxy J3 Luna, Android Version 7.0), which removed the need for a computer, increased portability, and ensured fully automated control of the integrated device without the need for user interaction. This device, for which consumable components (membranes, LFIA, adhesive, reagents) cost only $2.23 per assay, and reusable components (temperature control circuit and housing) are $70.08, is comparable in price to other rapid HIV tests developed for resource-limited settings and will decrease as scale-up the manufacturing of the device becomes possible.[39, 103] This Microfluidic Rapid and Autonomous Analysis Device (microRAAD) demonstrates the potential for simple and low-cost HIV detection at the point of care being aided by low-cost, low-power inkjet printed microheaters.

4.3.4 Supplying power at the POC.

A cheap, sustainable, and reusable power solution that does not increase waste burdens is critical for increasing accessibility of diagnostics that require heating. Solar powered chargers, while expensive, can be used to charge batteries in remote areas and areas with turbulent power grids to ensure adequate power when necessary. Paper-based batteries have also been investigated and present another alternative for cheap and discreet power for paper devices incorporating printed electronics. One such example is a paper-based battery used for powering an electrochromic display on an electrochemical sensing platform developed by Liu and Crooks[104]. They report an open circuit voltage (OCV) of 1.0 V for their zinc foil and NaCl electrolyte battery which suggests this technology could prove useful for powering microheaters like ours on paper-based assays in the future. Our use of a single rechargeable NiMH AA battery is the lowest voltage and most sustainable solution for high temperature incubations to-date. Tang *et al.*[105] and Pardy *et*

al.[106] both used two AAA alkaline batteries to produce their 3V potential necessary for heating their LAMP reactions to 65°C. NiMH batteries are known to provide a better voltage plateau (meaning more stable discharge over time) than rechargeable Alkaline batteries resulting in more consistent heating for a longer time period[106,107]. Alkaline and NiMH batteries are both considered non-hazardous waste and can be recycled if recycling is available in the region. By reducing the voltage by more than half (from 3 V to 1.2 V for experiments without a microcontroller), I enable a greater ability to incorporate these microheaters into cheap and portable cell phone powered platforms for multi-temperature and sequential heating, which was successful[39]. It is important to note that voltage is not the only factor of concern in this work. There is a delicate balance that must be understood when using batteries to power a simple circuit containing one or two microheaters. Because of their low resistance, my microheaters allow a large current (amps) to be discharged by a connected battery. If the discharge rate exceeds the recommended percentage of battery capacity (mAh), the battery itself may store less and less total mAh during the next charge. In the case of a platform that needs to be reusable to the point this could be a problem (hundreds of repeated use cycles), it is possible to increase resistance and voltage in favor a better long-term capacity plan and should be tuned to the intended resulting platform and environment. High-capacity batteries have become much more common in cell phones and cheaper to buy as single components as well. Because we did not This evidence supports the claim that this work can be built upon using our simple methods to further the potential for accessible diagnostics worldwide.

4.4 Conclusions and Future Directions

I have demonstrated both a unique yet highly reproducible and potentially scalable method for incorporating high-accuracy heating elements into paper-based POC assays suitable for a wide array of uses. I demonstrated the utility of these microheaters to maintain desired temperatures with and without the aid of a microcontroller and showed they can be simply used with a common AA battery. These demonstrations did require temperature monitoring, but overall, these results speak to a promising possibility of future microheater integration schemes that utilize minimal electronics for assay automation and thermal control needs. I also demonstrated that these microheaters can easily be incorporated into a fully portable, automated platform which successfully allowed rapid, accurate detection of HIV from whole blood.

5. DEVELOPMENT OF A 2-DIMENSIONAL PAPER NETWORK FOR AUTOMATED SEQUENTIAL FLOW CONTROL OF MULTIPLE REAGENTS

Parts of this chapter are reproduced from Ref. [16]*, an open access article from the Journal ASC Omega. Contributors to this work include undergraduate researchers Laura Stout, Haley June, and Anna Bird.*

5.1 Rationale

Previous works have set a promising precedent by using 2DPNs as a platform to perform ELISAs for protein detection. By tagging nucleic acid (NA) amplicons with proteins, ELISAs have been translated for detection of NA samples for improved signal clarity as well.[28,49,15] Recent developments in chemical ligation assays resulting in enzyme-free NA amplification and CRISPR-based diagnostics have created exciting new molecular platforms for rapid pathogenic detection at low-temperatures and have potential for improved sensitivities at the POC. However, many of these processes, including template assisted rapid assay (TARA), produce low product yields (10^2 amplicons of the initial target concentration) when compared to loop-mediated isothermal amplification (LAMP) or PCR (10^9 amplicons).[108,109] Still, the utility of a room-temperature assay for point-of-care use would put NA detection on-par with FLAIs and greatly improve NA assay implementation. To mitigate the issue of assay sensitivity, we have integrated an ELISA into a 2DPN to provide secondary signal enhancement of captured, NA amplicons in the detection zone. This enables us to maintain a high sensitivity for these low yield samples.

Design of a fully integrated 2DPN ELISA requires optimization of the reagent delivery in order to improve performance and produce reliable signal enhancement[64]. Existing 2DPN devices are categorized by the location of fluidic inputs: the "leg" design, where reagent pads are placed at the far end of the leg which then extends and intersects with the main lateral flow body (typically at a 90º angle)[65], or the "linear" design, where the reagent pads are placed directly on the main lateral flow body[28]. Previous 2DPN ELISAs required as many as five to six fluid inputs with one or more wet reagents that had to be prepared fresh[15,28]. By reviewing these "linear" and "leg" designs and performing mathematical modeling of capillary flow through various nitrocellulose channel widths, we designed a device that utilizes a combination of the "leg" and "linear" design, as well as a unique delay valve, to sequentially deliver reagents to the detection zone for a fully

automated 2DPN ELISA. This enabled us to incorporate the enzymatic signal amplification more effectively in our sequential flow, reduce the number and volume of washes, and allow the user to add only a single rehydrating buffer rather than storing and mixing refrigerated reagents in the field. The colorimetric enhancement optimization itself is discussed in Chapter 6.

5.2 Materials and Methods

5.2.1 Reagents and Materials

Reagents used throughout this work include PBST (0.05% Tween® 20, Millipore Sigma, Inc., Burlington, MA), 40 kDa polyvinylpyrrolidone (PVP40) (Millipore Sigma, Inc., Burlington, MA), fraction V bovine serum albumin (BSA) (Biotium, Fremont, CA), sucrose (IBI Scientific, Dubuque, IA), polyethylene glycol (PEG) (MW 3350 Da, 0.2% w/v), trehalose (Thermo Fisher Scientific, New Jersey), $FeSO_4$-EDTA (Fe-EDTA) (Millipore Sigma, Inc.), and molecular biology water (Thermo Fisher Scientific). DAB and urea hydrogen peroxide SigmaFast tablets (#D4168, Millipore Sigma Inc., Burlington MA) were rehydrated according product specifications for initial dried enzymatic signal testing. For long-term storage tests, hydrogen peroxide urea-adduct (#95314-250G, Millipore Sigma, Inc.,) tablets were crushed into a powder. Streptavidin poly-HRP (#21140, Pierce Biotechnology, Rockford, IL), and 40 nm gold nanoparticles (G-40-100, Cytodiagnostics Inc., Burlington ON) for streptavidin-polyHRP-AuNP conjugation (SA-HRP-AuNPs). Goat anti-rabbit biotin conjugate (#31822, Thermo Fisher Scientific) was used as the flow-control line. For the test line, monoclonal anti-FITC antibody (1F8-1E4, Invitrogen, Rockford, IL) was used for long term dry storage tests. Due to product changes and subsequent lack of binding for different lot numbers, we switched test-line antibodies and used anti-FITC antibody (20C-CR1056SP, Fitzgerald, Bath BA1 1BE, UK) for LOD dried tests and for the remainder of the investigation. All oligonucleotide probes were custom ordered from IDT (Integrated DNA Technologies, Inc., Coralville, Iowa). Food coloring for wet-out flow testing (McCormick Assorted Food Color & Egg Dye, Walmart, West Lafayette IN) was diluted in PBST.

Materials included (FF80HP) and Chr1 cellulose absorbent pad (#3001-861) from GE Healthcare Bio-Science Corp. (Pittsburgh, PA), Grafix Dura-Lar Clear Adhesive-Backed Film (Dick Blick Art Materials, Galesburg, IL), glass fiber reagent storage pads (#GFCP103000, Millipore Sigma, Inc.), and silica gel desiccant (S-3903, ULINE, Pleasant Prairie, WI).

5.2.2 Characterization of LFIA Components

The volume capacity of the nitrocellulose membrane and the glass fiber conjugate pads was calculated by determining dry mass of the membrane using a ME-T Analytical Balance (Mettler Toledo), submerging the membrane in DI water for two minutes, and then determining the wet mass of the membrane. Using the density of water, the total volume held by the membrane segment was calculated and divided by the area of the segment. The volume released from the glass fiber pads was estimated by first measuring the wet mass of the membrane. Then the membrane was placed on nitrocellulose with a 2 mm overlap and covered with adhesive. The post-flow mass was measured after leaving the wet membrane in contact with nitrocellulose for twenty minutes. The volume released is expressed as a percentage difference of post-flow mass and wet mass relative to the initial wet mass.

5.2.3 Governing Equations for Fluid Flow Analysis

The flow rate of each of the reagents was analyzed using mathematical models for capillary pressure based on the Washburn Equation derived by Berthier et al. because this derivation, with our assumptions, could be used to easily confer geometric impacts on surface tension while controlling for fluid viscosity differences. Capillary pressure (P_c) in a rectangular channel is described by the equation: $P_c = \gamma(cos(\theta_a) + cos(\theta_b))/h + \gamma(cos(\theta_c) + cos(\theta_d))/w$, where γ is surface tension, θ_i is the contact angle of fluid on each *i* surface, *h* is the height of the channel and *w* is the width of the channel[110]. If we convert this to nitrocellulose and assume a rectangular cross section of nitrocellulose and that particles are diluted in water, then $P_c = \gamma(2\cos(\theta)/h + 2\cos(\theta)/w)$, where every surface *i* is nitrocellulose and θ is the advancing contact angle of pure water on nitrocellulose. Given that our nitrocellulose membrane, FF80HP (GE Healthcare), has pore size comparable to HF135 (Millipore)[111], which can pass particles of up to 0.5 µm[112], we can assume an approximate pore size of 0.5 µm. For water on 0.45 µm pore size nitrocellulose, the advancing contact angle has been measured to be approximately 40º [113]. The capillary force is then equal to $F_{cap} = P_c * hw$. Substituting in the expression for P_c, the equation becomes $F_{cap} = \gamma\, 2\cos(\theta)\,(w + h)$. Due to the low Reynold's numbers in small capillary channels, the inertial effects can be neglected, and the capillary force can be equated to the drag force $F_{drag} = 6\mu VzC$ [66], where μ is the viscosity of the fluid, *V* is the

velocity, z is the distance traveled in the capillary channel and C is the geometric constant: $C = 2\mathrm{h}/\mathrm{w} + \mathrm{w}/\mathrm{h}$. Then, $6\mu VzC = \gamma\, 2\cos(\theta)\,(w + h)$. Then, rearranging to solve for flow velocity gives:

$$\mathrm{V} = k\frac{2\cos(\theta)(w+h)}{6zC} \qquad \text{Equation 8}$$

where nitrocellulose width (w) and height (h) is maintained and k is defined as γ/μ (surface tension over viscosity) and is determined experimentally for DAB and AuNP solutions. This resulting equation is very similar to Fu et al.'s use of Darcy's equation [114], without needing to determine or assume inaccurate parameters for permeability or ΔP. Of course, one can multiply viscosity found from doing a similar nonlinear fit using Darcy's equation to show that surface tension as it relates to geometry follows our results. Because we were focused on comparing only our own results to find the most consistent flow this was not a focal point of this work.

5.2.4 Flow Rate Analysis

One-dimensional flow studies were performed with reagents in nitrocellulose channels of varying width. Linear nitrocellulose patterns were designed in Adobe Illustrator CS6. Designs were 50 mm long with a width of either 1, 2, or 5 mm and included a fluid collection segment at the end with an area of 100 mm^2. The nitrocellulose patterns were cut from with a Silhouette Cameo 3 cutter (Silhouette America®, Inc., Lindon, Utah). The nitrocellulose was blocked with a solution of 0.25% PVP40, 2% BSA, and 5% sucrose in PBST to prevent nonspecific binding[115]. The volume used in each test was adjusted for the nitrocellulose and glass fiber pad volume capacity. The sample of conjugated AuNPs or prepared DAB was applied to the source pad. The flow was video recorded with an iPhone 6 at 30 frames per second with a 5 mm reference length in the frame until the fluid front reached the fluid collection segment. The distance and time measurements were plotted at the location of the fluid front for each frame in the video. The average velocity was calculated over five second intervals. The velocity vs. distance graphs were fit with a nonlinear curve of $\mathrm{V} = k\frac{2\cos(\theta)(w+h)}{6zC}$ Equation 8 using the least squares method to find the parameter k using GraphPad Prism v8. We assumed that dynamic viscosity (μ) is constant for each fluid. Therefore, we interpret a change in the k value as

a change in surface tension (γ), as surface tension is dependent on the surrounding environment, as well as the properties of the fluid.

5.2.5 Clean Delivery of Reagents in Nitrocellulose during 1D wetted flow

Clean delivery is defined as the sequential delivery of reagents with minimal parallel flow or mixing of discrete fluid samples[116]. The sequential delivery of fluids can be optimized by controlling the distance between the fluid sources. To determine the optimal distance between source pads, 5 mm x 100 mm FF80HP nitrocellulose strips were cut with Silhouette Studio scrapbook device. 50 µL of blocking solution (5% sucrose, 2% BSA, 0.25% PVP, and 0.05% Tween in PBS) was applied to strips and allowed to dry. 5mm x 8mm source pads were cut from Millipore glass fiber and placed at the start of the strip and varying distances from the start of the strip (10 mm, 15 mm, 20 mm). Cellulose wick was placed at the end of the nitrocellulose strip. 25 µL of SA-HRP-AuNP solution was deposited on upper source pad and 25 µL of PBS wash (with food coloring for visualization) was placed on lower source pad simultaneously. Flow timed until the front edge of the PBS reached 10 mm past the upper source pad. Lateral flow strips were imaged at time when front edge of PBS reached 10 mm past the upper source pad. The percentage of PBST fluid front coverage was calculated using ImageJ analysis.

5.2.6 2DPN Assembly

2DPN materials for fabrication and storage includes nitrocellulose (FF80HP) and Chr1 cellulose absorbent pad (#3001-861) from GE Healthcare Bio-Science Corp. (Pittsburgh, PA), Grafix Dura-Lar Clear Adhesive-Backed Film (Dick Blick Art Materials, Galesburg, IL), glass fiber reagent storage pads (#GFCP103000, Millipore Sigma, Inc.), and silica gel desiccant (S-3903, ULINE, Pleasant Prairie, WI). We created the 2DPN design in Adobe® Illustrator ® software (CS6, Adobe Inc., San Jose, California). Nitrocellulose and adhesive patterns were laser cut with VLS3.50 laser cutter (Universal Laser Systems Inc., Scottsdale, AZ). Adhesive patterns were cut from Dura-Lar Clear Adhesive. 0.2-0.4 µL of 1.3 mg/mL Goat anti-rabbit biotin conjugate was pipetted onto the nitrocellulose for the control line. 0.2-0.4 µL of 1.5 mg/mL anti-FITC antibody was pipetted onto the nitrocellulose for the test line. Glass fiber pads and the cellulose waste pad

were hand cut with a clean razor. The 2DPN components were assembled on the adhesive backing as shown in Figure 5.1 below. 2DPN storage conditions are shown in **Figure E. 1**.

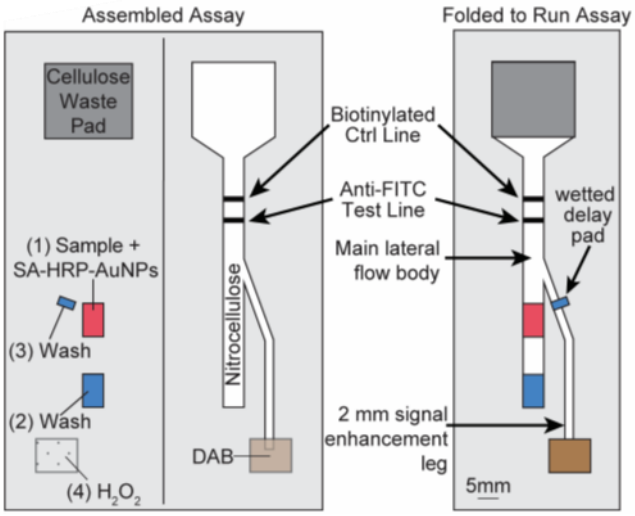

Figure 5.1 Detailed Schematic of finalized design.

5.3 Results and Discussion

5.3.1 Characterization of LFIA Components

In hollow glass capillary channels, as studied in Berthier's capillary flow resistors[117], the surface tension is primarily indicative of the physical properties of the fluid, where cohesion describes fluid interaction with the surrounding glass. Nitrocellulose, however, is a porous membrane which uses capillary pressure to pull the fluid forward perpendicular to the direction of each individual "capillary". As such, the environment surrounding the fluid varies greatly, and can change depending on the geometry of the channel, the components of the fluid, the method of cutting the membrane, and the methods used for blocking the membrane against nonspecific binding. Based on my observations from several variations of our methods, it is clear that laser cutting of backed nitrocellulose produces the most consistent edges, so long as speed and power intensities do not excessively singe the membrane itself. Previous work in our lab used a vinyl razor cutter which often produced jagged edges resulting in inconsistent pressure at the fluid front during wet-out flow (results not shown). Additionally, excessive volume, poor mixing, or use of old stocks of blocking solution impedes fluid flow on nitrocellulose and increases risks for

problems with analyte binding resulting in loss of signal (false negatives) or non-specific binding (false positives) at the detection zone. Adequate drying of blocking fluid on nitrocellulose is also critical for reliable binding and fluid flow. Sample viscosity and overall composition also greatly impacts flow speed on nitrocellulose and addition of Tween® 20 (Millipore Sigma) typically improves transport of all sample types. After establishing these methods from literature, the largest factor affecting fluid transport speed and consistency is membrane geometry – which has been an area of great interest in paper-based diagnostics for some time now. Our first objective was to characterize our membranes. FF80HP (GE Healthcare) was selected for having the capillary flow rate of (60-100 s/4cm) while being adequate for use with both water and highly viscous samples according to the manufacturer.[118] Several membranes were tested according to the methods described in **5.2.2 Characterization of LFIA Components**, in order to select the best membrane suited for use as a sample pad, conjugate pad and other pads for holding dry reagents. Additionally, we selected Grade 1 Cellulose Chromatography paper for the absorbent pad based on total saturated volume capacity and ensured it exceeded the necessary post-flow liquid waste volume. We found that 6 mm x 8 mm glassfiber pads hold an average volume of 30 μL of water when dipped in water and dabbed for excess. When these pads were applied to 1 mm, 2 mm, and 5 mm nitrocellulose strips, they released an average of 17μL water by mass with no correlated difference based on nitrocellulose width. These experiments provided average volume per area data where glassfiber membranes hold 0.85(± 0.10) μL/mm^2 and release over 50% of this volume when applied to FF80HP nitrocellulose, which only reaches saturation at an average of 0.10 μL/mm^2. These calculations allowed us to quickly scale the size of the 2DPN based on the necessary sample volume and other fluid flow changes as we needed to make.

5.3.2 Flow Rate Analysis

The wet-out flow testing results (Figure 5.2 and **Table D. 1**) demonstrate that (in nitrocellulose legs with very small widths) as the width of the channel decreases, the apparent surface tension of a solution containing DAB or AuNPs in nitrocellulose decreases. This is indicated by a channel width-dependent change in the *k* parameter for a given fluid. For example, AuNP flow testing showed a decreasing trend of k=230.3, k =126.1, and k=75.2 for 5 mm, 2 mm, and 1 mm respectively. A similar trend was seen in DAB flow testing results, which had *k* values

of 326.4, 137.2, and 52.76 for the 5 mm, 2 mm, and 1 mm channels, respectively. This surface tension shift causes changes in total flow velocity, this is illustrated in Figure 5.2 A and B below. Another observation taken from this data is that the conjugated AuNP solution is (as expected) more viscous than the DAB solution which is evident from the lower initial flow velocity and total distance traveled regardless of the channel width the solution was applied to. This indicates that the DAB solution is a better candidate for use in a secondary leg channel while the AuNP/sample transport should be prioritized in the main channel as is standard.

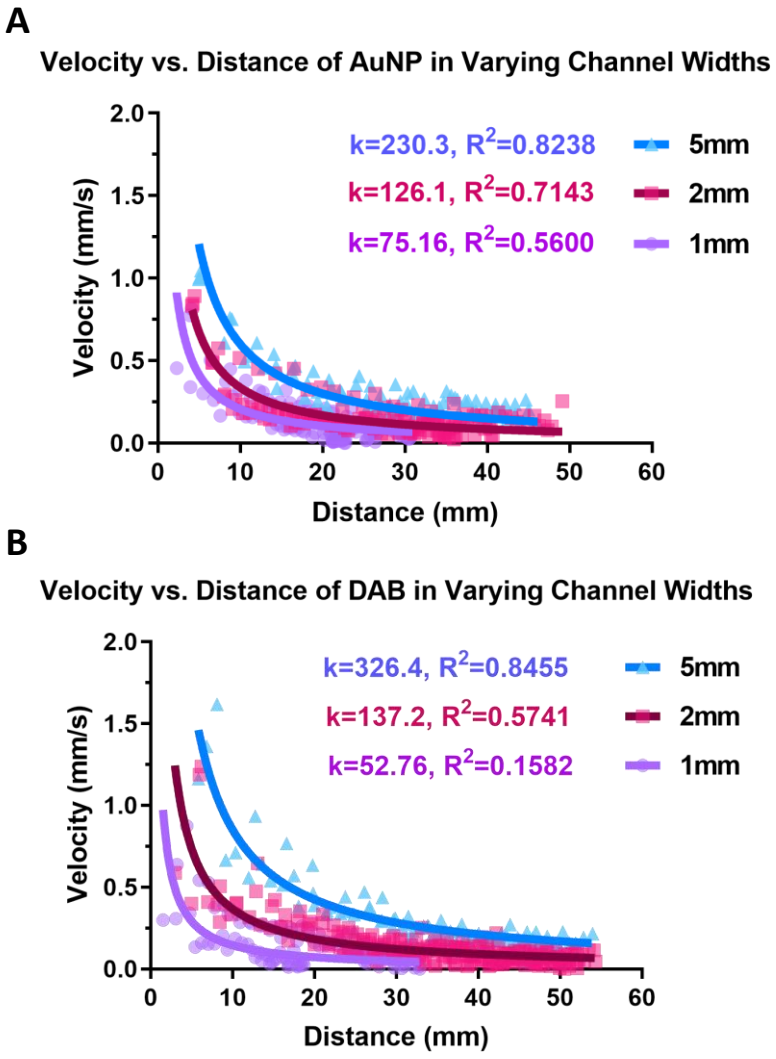

Figure 5.2. 2DPN dimensions and flow optimization. (A) and (B) show experimental data (shapes) fit with Eq. 1 (line). *k* refers to the parameter from Eq. 1 and R^2 is the coefficient of determination for the fit of Eq. 1 to the data shown. (A) AuNP solution velocity over distance in a 1-, 2-, and 5-mm wide channel; n=3 for each. (B) DAB solution velocity over distance in a 1-, 2-, and 5-mm wide channel; n=3 for each.

As the total width of the nitrocellulose channel decreases, a reduction in the surface tension at the fluid front is observed. This indicates a reduction in capillary pressure driving flow, and therefore a decrease in fluid velocity in the channel. These results predictably contradict findings from Berthier's glass channel results, but they do agree with other fluid transport models in porous membranes, including Dharmaraja *et al.*'s work which discusses decreasing channel width as a method to increase "resistance" of flow on wetted nitrocellulose when sequential flow is occurring[116]. This more closely matches our reagent delivery in the constructed 2DPN. The R^2 values for thinner channels (<5 mm) (Table D.1) indicate flow that is less consistent than in wider channels. This inconsistency was particularly prevalent in the first 15 mm of the channels. This modeling is still useful to us with the correct interpretation of results, which allowed us to select the appropriate channel widths for maximizing flow consistency and speed for each region of device.

We made design selections based on the results of our component characterizations and wet out flow tests. The width of the main lateral flow channel for the AuNP bound sample solution was chosen to be 5 mm because it produced the fastest and most consistent flow (Figure 2A). The width of the signal enhancement leg for DAB solution was set at 2 mm (Figure 2B) because the fluidic resistance of the smaller channel was designed to reduce the backflow of fluid from the main channel into the signal enhancement leg. In initial experiments, when fluid from the main channel flowed back into the enhancement leg, reaction of SA-HRP-AuNP bound sample with the DAB began before sample binding in the detection region. This resulted in reduced sample binding at the detection zone and increase smearing or background noise. We found the 2 mm channel alone was not enough to prevent backflow. Therefore, we added a 5 μL "delay valve"[102] (2 x 5 mm) near the intersection of the 2 mm channel and the 5 mm channel. The capillary pressure exerted by the saturation of the signal enhancement leg prevented backflow of sample from the main channel.

During this phase of the design process, we also considered utilizing a different method to tune reagent speed at different regions of the device based on work done by Fu et al. As you can see in Figure 5.3 below, we tested the flow rate changes in a single channel wet-out flow on nitrocellulose with the desire to understand how our fluid flow would be impacted by widening or thinning the main channel.[114] Ultimately this work confirmed that the junction between the main channel and the secondary leg should integrate so as to maintain the main channel width rather

than widening slightly which was an early design consideration. The length of the secondary leg was chosen based on distance and time results from flow testing to ensure that the DAB and H_2O_2 arrived at the detection zone after the sample and wash fluids. The volume of the DAB and H_2O_2 pads was then adjusted to compensate for the volume capacity of the nitrocellulose leg. Similarly, sample and wash volumes were adjusted for based on the volume capacity of the nitrocellulose platform (Table D.1).

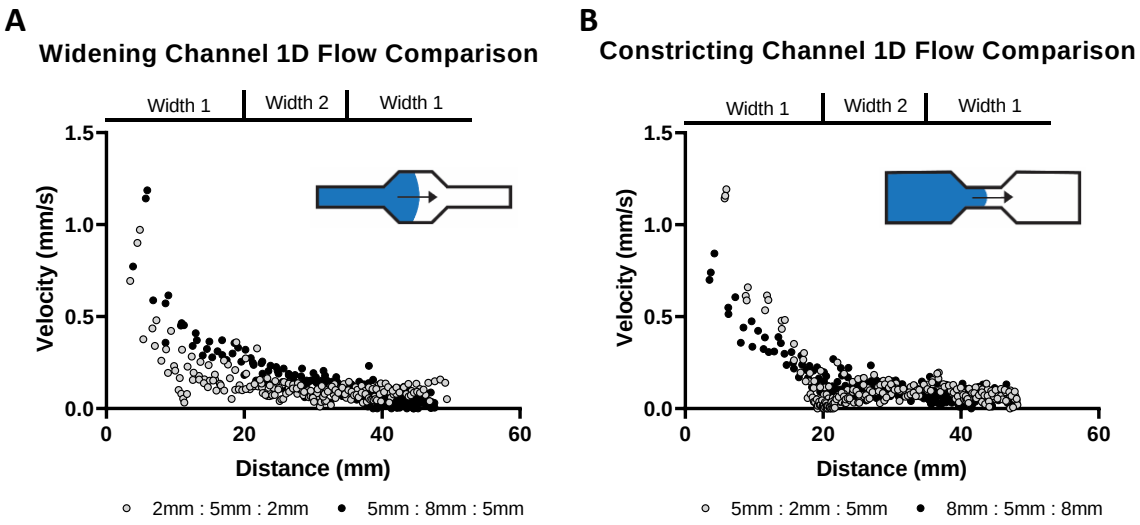

Figure 5.3 1D flow optimization in nitrocellulose with changing geometries. (A) and (B) show experimental data (circles), n=3 for each.

Using a derived capillary pressure calculation instead of Darcy's equation allowed us to use velocity as the variable of interest and calculate the velocity of the fluid in each segment of the nitrocellulose in Figure 5.3. From Figure 5.3. (A) we observe a relatively consistent decrease in fluid velocity that is similar to the flow across a channel of consistent width like in Figure 5.2. From Figure 5.3 (B) we observed that a sudden thinning of the channel predictably impeded flow and drastically reduced the velocity of the fluid front which did not recover upon reaching the widened segment. This lack of flow recovery is an important factor that suggests the pressure at the fluid front in the furthest segment is perpetually impeded by the reduced flow in the segment preceding it. This lack of flow rate recovery could also be due to a lack of excess fluid pressure at the channel inlet since the fluid front did not reach the end of the 60mm channel for any of these experiments. An improvement on this experiment would use a continuous reservoir at the inlet to

ensure even source pressure and ensure the fluid front reached the end of the channel. Overall, these experiments confirmed we could use a thinner “leg” channel which opens into a wider primary channel without drastic changes in flow rate.

5.3.3 Clean Delivery of Reagents in Nitrocellulose during 1D wetted flow

A unique aspect of this design compared to previous literature is the location of the leg-channel intersection downstream of the sample pad. Importantly, this allows us to deliver the DAB and H_2O_2 upstream from the detection zone but downstream from the sample pad in order to prevent premature signal development and high background signal at the detection zone. Additionally, the intersection is set at a 20° angle from the main channel to ensure flow in only one direction. Previously, inferior performance for leg devices was reported due to parallel reagent delivery which results in signal appearing only in the middle of the test zone[28]. To ensure this would not be a problem, we assessed “clean delivery” of each reagent. Clean delivery was defined as each model fluid (food coloring) being delivered across a minimum of 90% of the 5 mm channel width at the detection zone (

Figure 5.4). We established that the DAB leg intersection must be a minimum of 10 mm upstream of the detection zone for this clean delivery to occur.

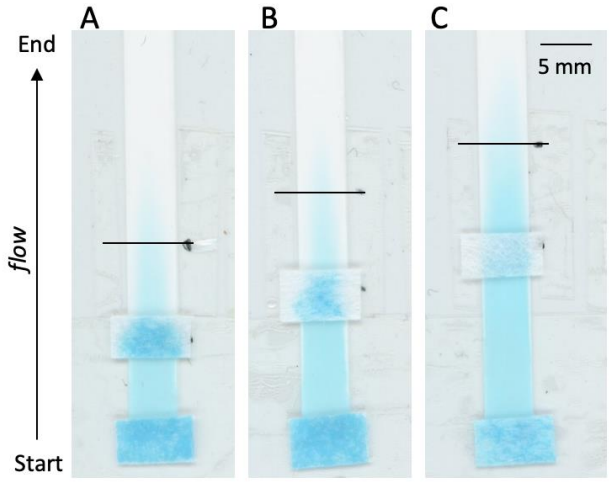

Figure 5.4 AuNP and PBST fluid interface at designated point 10 mm past the upper source pad (black line) for varying source pad separation (A) 10 mm source pad separation, PBST fluid front covers 58.18% of strip width at designated point (B) 15 mm source pad separation, PBST fluid front covers 46.15% of strip width at designated point (C) 20 mm source pad separation, PBST fluid front covers 90.00% of strip width at designated point.

5.3.4 2DPN Flow Timing

Following wet-out flow testing studies and 2DPN dimensions optimization, several food coloring timing studies were performed to ensure sequential fluid delivery in the final, fully optimized nitrocellulose design (Figure 5.5). As you can see from the left-most panel of Figure 5.5, a secondary leg length of 20mm (from the inner corner of the junction to the edge of the large sample pad) impedes and produces co-flow between the wash (yellow) and sample (red) fluids which could potentially reduce the amount of bound AuNPs in the right half of the test zone. Meanwhile the middle and right panels of the GIF with secondary leg lengths of 30mm and 35mm respectively allow a large amount of sample (red) fluid to flow before the two wash fluids (blue and yellow) follow via co-flow. In order to optimize for overall efficiency, the middle panel design was chosen and details of each fluid timing for this design is shown in the far right of Figure 5.5.

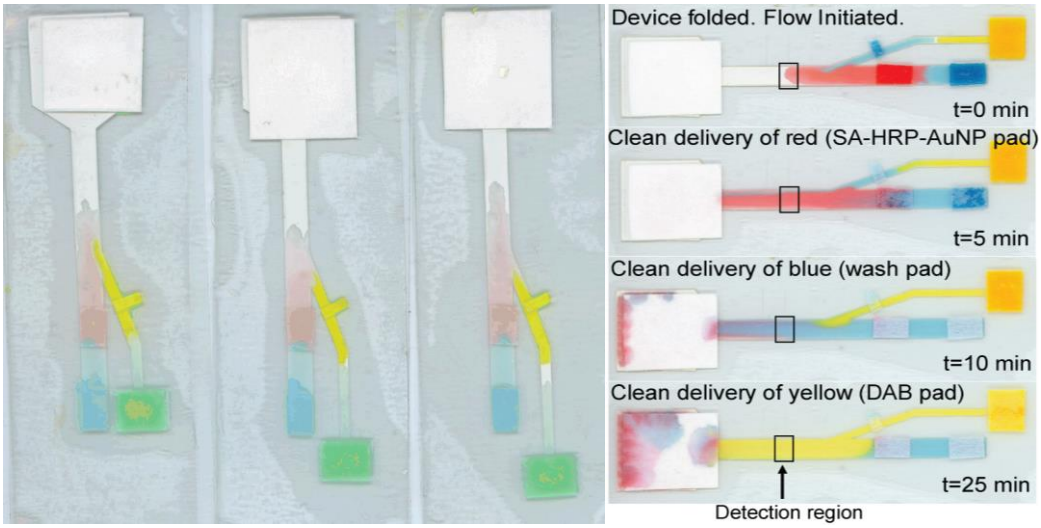

Figure 5.5 Left: GIF showing flow comparison of secondary leg length impact on fluid delivery. Right: Proof of concept 2DPN flow with labeled steps visualized with food coloring in PBST demonstrating the sequential delivery of reagents to the detection region (boxed).

Based on the results of these flow studies and flow studies with freshly prepared reagents, the SA-HRP-AuNP bound sample reached the detection zone at approximately five minutes, followed by clean delivery of the wash solution at the detection zone at ten minutes. Therefore, the pre-enhancement signal, occurring prior to DAB and H_2O_2 delivery, was defined as the signal intensity at 10 minutes, which is comparable to other commercial tests[119,120]. The DAB and H_2O_2 signal enhancement solution arrived at the detection zone at 25 minutes and produced a reliable signal increase at 40 minutes which was maintained through and past our 90-minute cut-off period. This is shown and discussed further in section 6.3.2 “Signal Enhancement Stability Over Time”. While the food coloring experiments were useful for initial flow evaluations, they did not account for the viscosity differences between the AuNP/sample fluid (most viscous, slowest flow) and the other reagents such as the PBST in the delay pad, which sometimes prematurely traveled down the main channel in a similar fashion to what is seen on the left-most design in Figure 5.5. This issue was easily managed by simply reducing the volume of PBST applied to that pad from 10 μL to 5 μL for the remaining experiments.

Reducing the total number of fluidic inputs decreases the number of user steps and changes saturated flow velocity for all fluid fronts except the sample pad (which is completely driven by

wet-out flow). We did not use a final wash upstream of the DAB because DAB does not require a "stop solution" to arrest color development, unlike most other colorimetric enhancement reactions including gold and silver enhancement, and tetramethylbenzidine (TMB)[121]. A wash buffer upstream of the DAB/H_2O_2 pads could increase the flow velocity of both solutions and potentially reduce final background staining at the detection zone. However, there is a risk that this would also ultimately dilute one or both of these reagents before they can reach the reaction zone and reduce the time available for the necessary oxidation reaction at the test and control lines. Testing this was not deemed advantageous because it would require a total redesign of the 2DPN flow with no guarantee of improvements in either signal-to-noise ratio or total assay time. Further discussion of DAB/H_2O_2 concentration on background staining in the detection zone and other variables are presented in Chapter 6.

This platform began as a tri-leg platform (Figure 5.6, left-most panel) which contained a mixing region just before the detection zone with the intention of improving the resulting signal enhancement. Early experiments not discussed in depth here showed this approach actually increased background staining while decreasing flow speed. We set about redesigning the 2DPN which resulted in increasing the total volume the platform could transport due to expected sample sizes provided by CrossLife Technologies Inc. This led us to the research I just described in this chapter which has ultimately resulted in a 2DPN with only four fluidic inputs, one initiation step and consistent flow control.

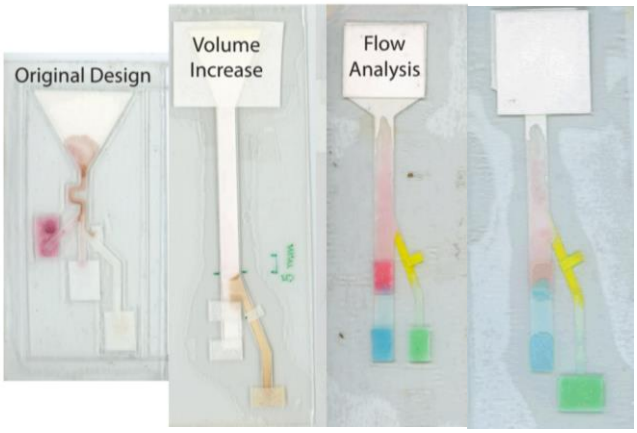

Figure 5.6. Progression of 2DPN designs for flow control from initial to semi-final design.

5.4 Conclusions and Future Directions

We successfully demonstrated methods for evaluating and implementing flow control in a 2DPN format which resulted in a platform that produces consistent sequential flow of four fluid inputs for the purpose of performing an automated ELISA. This work shows unique advancements including reducing the number of user steps with the application of one consistent fluid (PBST) to all non-sample pads compared to other platforms in the literature which required at least one additional freshly prepared reagent.[15] Furthermore, making double use of the delay pad on the leg portion of the platform as both a wash for driving AuNP flow down the main channel while also protecting against premature background staining as a result of premature SA-HRP-AuNP contact with DAB/H_2O_2 is a unique advancement.

Because total assay time is so critical for users in hospitals and clinics, the total assay time should be under 60 minutes to reduce result backlogs and patient wait times. Although the "active time" for the assay has successfully been minimized, the passive/wait time from sample to result could be improved. This could be achieved by using a faster transport membrane such as FF120 which has a capillary flow rate of 90 – 150 s/4cm, but adjustments to the 2DPN might be required to ensure reagent timing remained intact. At this point the sample viscosity and the viscosity of the rehydrated reagents were unknown variables and we remained conservative on flow speed to allow for better understanding of assay dynamics.

6. 2-DIMENSIONAL PAPER NETWORK PROVIDES CONSISTENT, AUTOMATED COLORIMETRIC ENHANCEMENT OF AMPLIFIED NUCLEIC ACID SAMPLES WITH DRIED REAGENTS, IMPROVES LIMIT OF DETECTION

Parts of this chapter are reproduced from Ref. [16]*, an open access article from the Journal ASC Omega. Contributors to this work include undergraduate researchers Laura Stout, Haley June, and Anna Bird, who is a co-author on the original publication. This work was performed in collaboration with CrossLife Technologies and Founder, President, CEO, Hyundae Cho, Ph.D.*

6.1 Rationale

As discussed in **1.3.2 2-Dimensional Paper Networks and Protein detection via paper-based ELISAs** there remains much improvement needed for rapid detection of pathogens at the POC that can be mediated by well-designed 2DPN-automated assays. The 2015 MERS-CoV outbreak was yet another indicator that rapid detection of highly infectious viruses should be a high priority for POC testing, we chose to focus on this pathogen for this reason. Isothermal amplification of viral RNA at the POC will soon be a standard in the healthcare industry, but reliable platforms to provide clear and understandable results are still needed, particularly where amplification conditions are unfavorably diminished by complex samples and poor storage conditions, or for low-threshold amplification systems such as Template Assisted Rapid Assay (TARA), which is a proprietary, enzyme-free isothermal amplification method developed by CrossLife Technologies Incorporated.[108] Because the TARA assay is enzyme-free, runs at room temperature, and contains highly stable PNA strands, it is an excellent candidate for POC NA amplification.[108,122] This work is aimed at providing a 2DPN platform that contains fully dried buffers and enzymes to reliably enhance the detection of isothermal NA amplicons produced by TARA reactions and other similar amplicons from LAMP. This platform should provide consistent results that are maintained over time, long after the instructed readout time for secondary validation if needed. Combined with POC NA amplification, this assay should simplify and reduce the total time and effort needed to diagnose a patient with MERS-CoV by providing a one-stop sample-to-answer diagnostic. The development and optimization of dried detection components should ultimately result in a platform suitable for clinical sample concentrations.

6.2 Materials and Methods

6.2.1 Reagent drying

For the dried components of the AuNP signal and subsequent enzymatic enhancement we employed specific methods proven by previous literature to maintain stability of each reagent. Streptavidin poly-HRP (SA-HRP) was added to each 1 mL of 1 optical density (OD) 40 nm AuNPs for a final SA-HRP concentration of 0.01 mg/mL. The solution was incubated on a rocker for 30 minutes at room temperature. The solution was blocked with BSA Fraction V (1% w/v) for one hour at room temperature followed by blocking with PEG (0.2% w/v) for one hour at room temperature. The AuNPs were centrifuged at 900 x g for 30 minutes. The supernatant was discarded, preserving the AuNP pellet. The pellet was resuspended in drying buffer (0.5X PBS, pH 7.4, 10% sucrose, 1% Tween 20, 0.5% BSA Fraction V, 0.2% PEG, 0.5% PVP40) and the OD was measured using a NanoDrop 2000c (Thermo Fisher Scientific). OD was adjusted by diluting conjugated AuNPs with drying buffer. Trehalose (4% w/v) and 0.01M Fe-EDTA was added prior to drying. Twenty-five (25) μL of the conjugated SA-HRP AuNP solution was then deposited on an 8 x 5 mm glass fiber pad and dried under vacuum with desiccant at room temperature overnight. To prepare dry DAB pads, one DAB tablet was rehydrated in 500 μL of PBST, for a concentration of 1.4 mg/mL. Trehalose (4% w/v) was added to the DAB solution[15]. Fifty (50) μL of DAB solution was deposited on an 8 x 10 mm glass fiber pad, then dried under vacuum at room temperature overnight. H_2O_2 tablets were crushed into a powder and 2 mg of tablet powder was affixed on the adhesive under a 50 μL capacity glass fiber pad. These dried reagent pads were incorporated into the 2DPN assembly process described previously, and then stored in vacuum sealed mylar bags (ULINE S-22818SIL) with desiccant and oxygen absorbing cards before storage at room temperature away from light. A fully assembled and sealed 2DPN is shown in Figure E.1

6.2.2 Design of Model Amplicons via DNA Probe.

To create a hybridized double-stranded DNA (dsDNA) model, 1 μL of 100 μM of 6-carboxyfluorescein (FAM) tagged ssDNA (Table E1, Probe 1), 1 μL of 100 μM of biotin tagged ssDNA (Table E.1, Probe 2), 10 μL of 10X isothermal amplification buffer I, and 88 μL DNase/RNase free water were combined in a small PCR tube. The PCR tube was placed in a

thermocycler and run on a protocol of 95ºC for 1 min followed by 25ºC for 1 minutes, for a total of 20 minutes. The concentration of the probe was determined using a NanoDrop 2000c (50 ng/μL per 1 OD). The hybridized dsDNA probe was stored in -20ºC until use. Single stranded DNA (ssDNA) tagged with both FAM and biotin (Table E.1, Probe 3), provided by IDT, was used as the ssDNA model.

6.2.3 Running samples on the automated 2DPN.

Volumes were loaded onto the 2DPN as follows: 25 μL of the NA sample onto pad (1), 25 μL PBST onto pad (2), 5 μL PBST onto pad (3), 50 μL PBST onto pad (4) (Figure 1A). Then the device was folded at the crease to initiate flow through the channels and sealed around the edges. Devices were imaged every five minutes using a flatbed scanner (V850 Pro, Epson America, Inc., Long Beach, CA) at 1200 dpi. For flow visualization, food coloring was added to PBST and deposited on the glass fiber pads. Test and control line intensities were analyzed with a custom MATLAB script[111,123]. The visible threshold (visual cutoff for interpreting a test line as positive) of the background normalized grayscale intensity was set to 0.02 for all signal analysis according to Phillips *et al.*[123].

For limit of detection (LOD) tests, dilutions of 100 μM Probe 3 solution in PBST were used. Tests were run on assembled 2DPNs stored between 1-7 days. ssDNA was used in the LOD tests because the exact concentration is provided by the manufacturer. NanoDrop measurements of dsDNA hybridized probe concentration provide an approximate concentration but cannot provide information on the amount that hybridized compared to remaining non-hybridized strands. Previous analysis of dried 2DPN results tested with comparable concentrations of ssDNA and dsDNA probes showed no significant differences in intensity (not shown). For storage tests, a dsDNA hybridized probe sample was diluted in PBST to approximate concentrations of 1E14 copies/mL and 5E12 copies/mL. The same dsDNA samples were used in all 1-day, 7-day, and 28-day storage tests. For both LOD and storage tests, replicates for any given sample concentration and device condition were performed simultaneously.

6.2.4 ELISA Standard Curve

Four-parameter logistic (4PL) models are typically used to model signal intensity as a function of sample concentration in ligand-binding assays, such as ELISAs[124]. We selected this model to evaluate our LOD produced by the DAB Enhanced Signal (Figure 6.4).

$$y = \frac{a-d}{1+10^{(c-x)b}} + d \qquad \text{Equation 9}$$

where *y* is signal intensity, *x* is log of sample concentration, *a* is the response at 0 concentration, *d* is the response at infinite concentration, *c* is the concentration that gives a signal intensity halfway between *a* and *d*, and *b* is a slope parameter typically near 1 [125]. The 4PL model was fit to the LOD data in GraphPad Prism v8 with the slope parameter (*b*) constrained to 1.

6.2.5 Template Assisted Rapid Assay (TARA).

TARA is a proprietary RNA amplification technology developed by CrossLife Technologies Inc.[108]. TARA is an enzyme-free chemical ligation assay that leverages a target RNA sequence to initiate hybridization of a peptide nucleic acid (PNA) backbone containing FAM to a second PNA strand containing biotin. This results in a single PNA strand with both markers (**Figure E. 2**). PNA probes to detect the nucleocapsid gene of MERS-CoV were designed using Applied Biosystems Primer Express™ v2 software (structure and sequence details shown in **Figure E. 3** and **Table E. 1**). Probe hybridization sequences were evaluated by the Basic Local Alignment Search Tool (BLAST) to select regions conserved across multiple transcript variants. For the initial design, target complexity and accessibility were evaluated using Visual OMP (DNA Software Inc., Ann Arbor, MI). PNAs were synthesized by PNAbio Inc. (Thousand Oaks, CA). ssRNA at an initial concentration of 2.0E11 copies/mL was purchased from IDT. TARA was performed with the ssRNA at room temperature for 15 minutes. Dilutions of final TARA products were made in PBST and applied directly to sample pads on 2DPNs that had been dried and assembled within the previous 7 days. The same diluted sample was used for all 2DPN tests. Replicates were performed simultaneously.

6.3 Results and Discussion

6.3.1 Optimizing 2DPN Detection Parameters

Effect of Streptavidin Poly-HRP conjugation concentration on LOD of ELISA Enhanced 2DPN

As expected, total amount of conjugated AuNP greatly affects the test line intensity when used with samples at or near the limit of detection. Anticipated these results, however due to the large impact the AuNPs have on the total device cost, we hoped to find the upper and lower limits of these effects. The commercial Streptavidin-poly-HRP product used to conjugate the AuNPs contained a proprietary and therefore unknown ratio of SA-HRP molecules. Our estimate was that based on the size of the 40nm AuNP and the size of Streptavidin, a minimum conjugation concentration of 0.01mg/mL would be sufficient to conjugate 1 OD AuNPS. However, we were curious about investigating the limit of detection and how it is affected by both the conjugate concentration as well as the total concentration of conjugated AuNPs. One key aspect of this is understanding that the SA-HRP concentration as well as DAB/H2O2 concentrations will impact background signal as well as LOD. This best illustrated by Figure 6.1 (below) where LOD improvement is visible in the bottom panels where despite a lower AuNP OD, the higher amount of SA-HRP caused a greater test line signal. Note, the intense background signal seen in both trials here is caused by excess DAB/H_2O_2 which was reduced from 6 mg/mL to 1.4 mg/mL in future experiments.

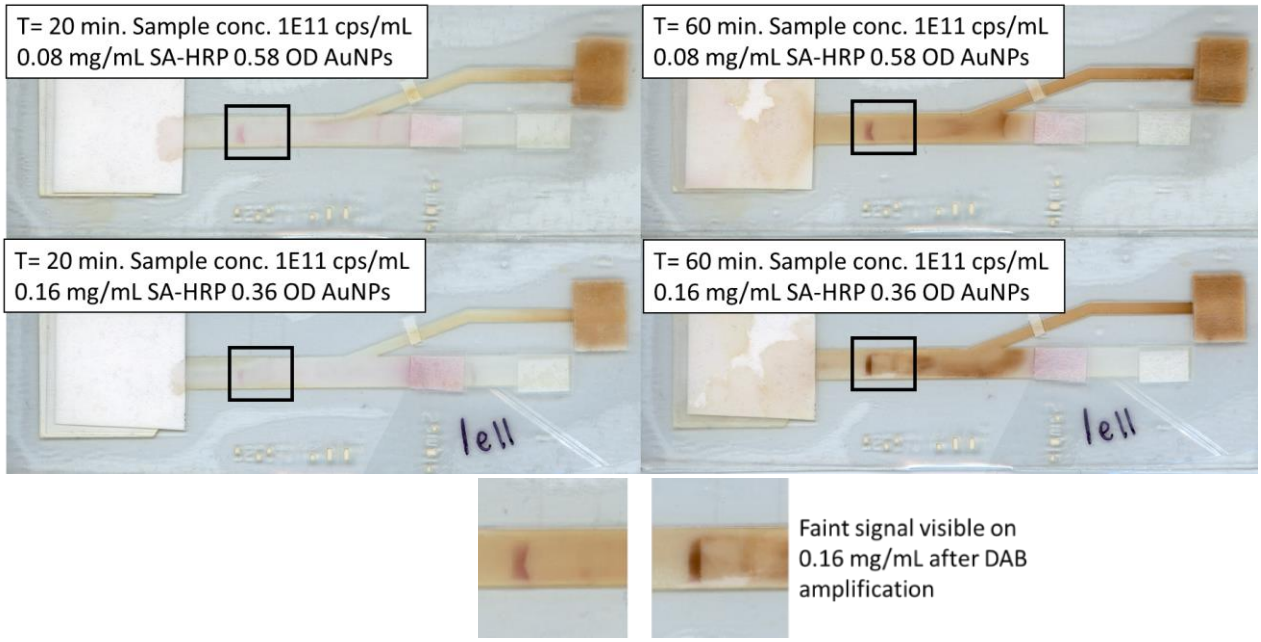

Figure 6.1 Comparison of 2DPN performance between AuNPs conjugated with more or less SA-HRP molecule. Sample concentration of 1E11 copies/mL, 6 mg/mL dry DAB (50 uL dried on pad), 6 mg/mL fresh H_2O_2 from sigma fast tablets (50 uL)

Effect of total conjugated SA-HRP-AuNP concentration on LOD of fully dried ELISA Enhanced 2DPN

We found that above 2.5 OD of conjugated SA-HRP-AuNPs there is no additional LOD improvement and above 3.5 OD causes increased background and waste from Figure 6.2 below. We also established that an OD less than 1 of conjugated SA-HRP-AuNPs produces a very faint signal. A summary of all major parameters optimized in this work is shown below in Table 3. Extensive testing was performed with both freshly prepared reagents and reagents dried under various conditions. Starting concentrations were taken from literature. After testing AuNP drying via low-temperature oven drying (with and without vacuum pressure), room temperature drying with and without vacuum pressure, and -80 freeze-drying under vacuum pressure, the results showed that drying under vacuum with desiccant at room temperature overnight was the best method. This was determined by observation of the dried pads appearance and their performance on assembled 2DPNS (data not shown)

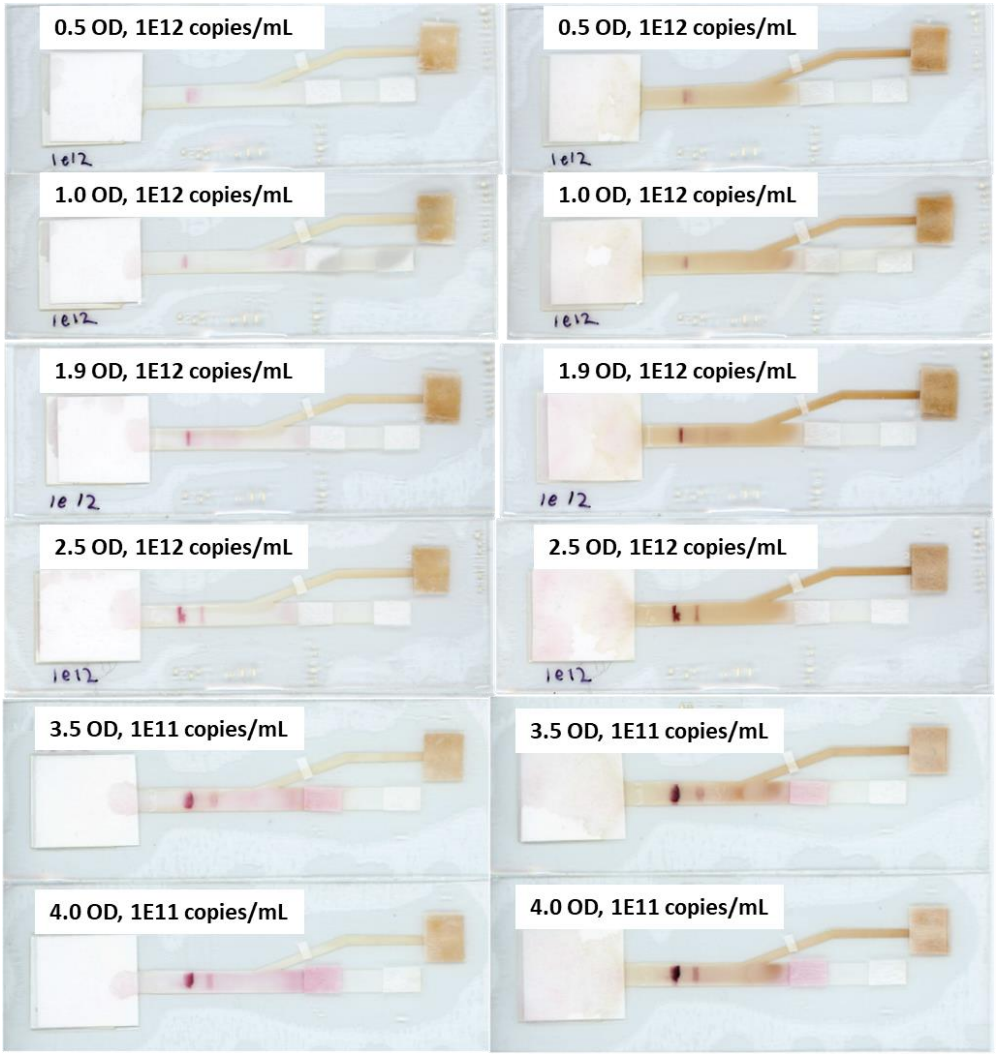

Figure 6.2 Representative samples from conjugated SA-HRP-AuNP Optimization. 20 minutes after flow initiation (left), 60 minutes after flow initiation (right). Other controlled variables: 1.4 mg/mL DAB and dried H2O2 salt. .

Table 3. Optimized 2DPN Parameters

Parameter	Tested	Criteria	Target Value	Optimized
AuNP conjugation method	N-hydroxy succinimide activated ($22.25/1 mL), passive adsorption ($1.95/1 mL)	No aggregation after drying	Aggregation indicated by a color change from pink to grey/purple	Passive adsorption
		Cost	Lowest cost	
AuNP optical density	0.5, 1, 1.5, 1.9, 2, 2.5, 3, 3.5, 4 OD	Signal-to-background ratio	> 0.02 test line intensity	1 OD (Above 1 OD, no improvement in the LOD)
		LOD	Lowest detectable concentration	
Main lateral flow body width	1, 2, 5 mm	Run time	< 1 hour	5 mm
Signal enhancement leg width	1, 2, 5 mm	No backflow from main lateral flow channel	Qualitative observation	2 mm
		Release of fluid from signal enhancement leg only after sample binding and wash	Qualitative observation	
SA-Poly-HRP concentration	0.005, 0.01, 0.02, 0.08, 0.16 mg/mL	LOD	Lowest detectable concentration	0.01 mg/mL (Below this, no improvement in LOD. Above this AuNPs are oversaturated and much is discarded as waste
DAB concentration	0.07, 1.4, 6 mg/mL	Signal-to-background ratio	> 0.02 test line intensity	1.4 mg/mL
Sample volume	25, 50 μL	Run time	< 1 hour	25 μL
Distance between sample pad and test line	5, 10, 15, mm	"Clean delivery"[116]	> 80% sample fluid coverage in main lateral flow channel	> 10 mm
Distance between sample pad and wash pad	10, 15, 20 mm	"Clean delivery"[116]	> 80% wash fluid coverage in main lateral flow channel downstream of sample pad	20 mm

6.3.2 Signal Enhancement Stability Over Time.

A previous study showed that the visible threshold for an untrained user without instruction would determine a LFA test line as positive at 0.02 grayscale intensity when normalized to background using a custom MATLAB program[111,123]. Based on this, we used the 0.02 greyscale intensity as the visible threshold for a positive result in our experiments. In Figure 6.3, Signal development over time, the test line signal is above the visible threshold and maintains steady contrast for consistent ease of reading at any time past the 40-minute mark, up to the final measurement at 90 minutes. 2DPNs also maintained this steady state contrast several hours after testing (not shown). Lathwall and Sikes have investigated a number of enzymatic colorimetric enhancement agents for the improvement of signal visualization on paper-based diagnostics[121]. They found that many common visualization agents did not retain distinguishable positive or negative signals after 40 minutes and that specifically timed reagent additions, wash steps, stop-solutions, and reading times would be necessary. This design, and our use of DAB resolves these cumbersome issues based on these results.

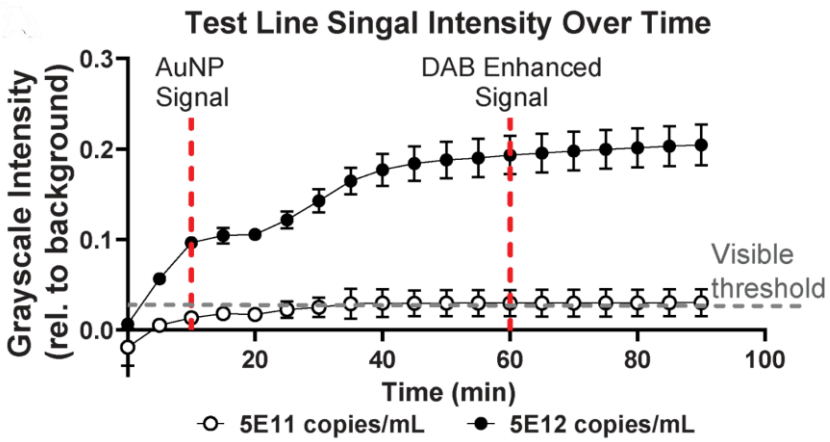

Figure 6.3 Signal development over time. (A) Signal intensity of test line over time for 5E12 and 5E11 copies of ssDNA/mL (n=3). Dashed lines indicate time points when AuNP signal and DAB enhanced signal data are compared.

6.3.3 ELISA Enhanced 2DPN Improves Limit of Detection.

In experiments where all components had been dried within the last seven days, DAB signal enhancement improved the LOD from 1E12 copies/mL to 5E11 copies/mL (Figure 6.4, replicates shown in Figure E.5). For 5E11 copies/mL, the average AuNP signal is 0.01 which is well below the 0.02 visible threshold, while the average DAB enhanced signal is 0.03. This LOD is comparable to that of RNA based assays in one-dimensional LFIAs with an enhancement solution, which was found to be ~1E11 copies/mL[126]. Figure 6.4 demonstrates the ability of this 2DPN enhancement solution to increase the intensity of the test line above the visible threshold, when the AuNP signal alone was not visible. Additionally, this visual enhancement does not increase the visibility of a negative sample test line and does not create false positives with negative (PBST only) samples.

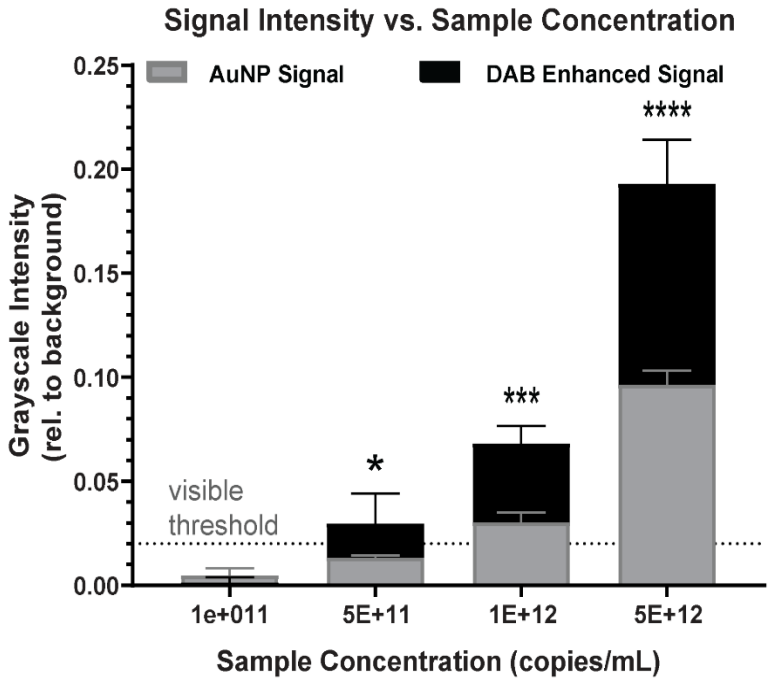

Figure 6.4. Normalized test line intensities at 10 minutes (AuNP Signal) and at 60 minutes (DAB Enhanced Signal) for varying ssDNA concentrations. Visible threshold at 0.02. (Dunnett's multiple comparison vs. 0 copies/mL, * p <0.05, ***p<0.001, ****p<0.0001, n=3, replicates shown in Figure E.5).

Others have presented improvements of signal intensity and visibility with viral detection platforms, but few have measured the true change in LOD in terms of copies/mL. For example, the Richards-Kortum group reports a visual signal increase of 15% with silver enhancement and 25% with gold enhancement[126]. We achieved an average 122% increase in signal intensity for the dried 2DPN with our LOD sample of 25µL containing 5E11 copies/ml ssDNA (Figure 6.5, **Table E. 2**). We detected an average signal enhancement of 116% for all samples above the LOD. Our device with signal enhancement can detect sample concentrations five times smaller than our device with AuNPs alone. Therefore, the signal enhancement translates to a five-fold reduction in the LOD.

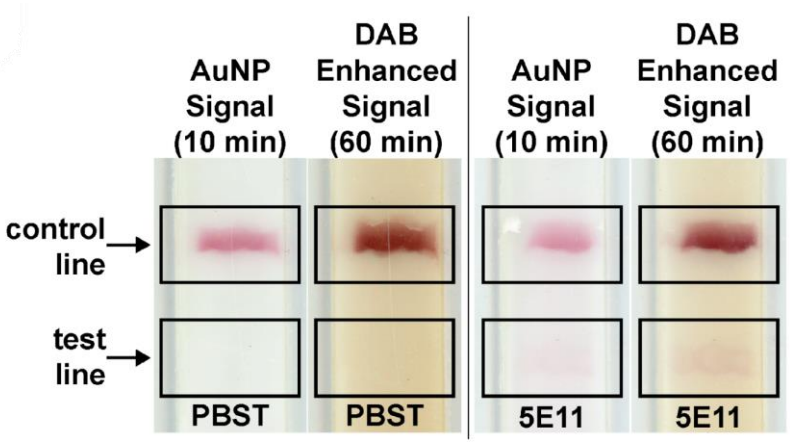

Figure 6.5 Detection region of 2DPN imaged at 10 minutes (AuNP signal) and at 60 minutes (DAB enhanced signal) with samples containing PBST (left) and NA amplicons at 5E11 copies/mL (right).

6.3.4 Signal Intensity Varies with Sample Concentration.

The signal output of the 2DPN showed test line intensity changes as a function of sample concentration. The fit of the ELISA (R^2=0.9771) from $y = \frac{a-d}{1+10^{(c-x)b}} + d$

Equation 9 with this data, indicates that our paper-based dried reagent ELISA assay can generate results like that of a traditional ELISA (Figure 6.6). This demonstrates the potential of this paper diagnostic to quantitatively determine sample loads, which is crucial for chronic disease monitoring applications. In order for this to be possible, much more investigation would be needed especially considering the exponential and highly variable nature of many NA amplification reactions. One additional control to enable this endeavor is the use of an additional amplification control line, or some other indicator showing that the NA amplification performed as expected. Quantification of LFAs and commercial differences will be discussed further later in this chapter when we compare commercial assays for detection of NA amplicons.

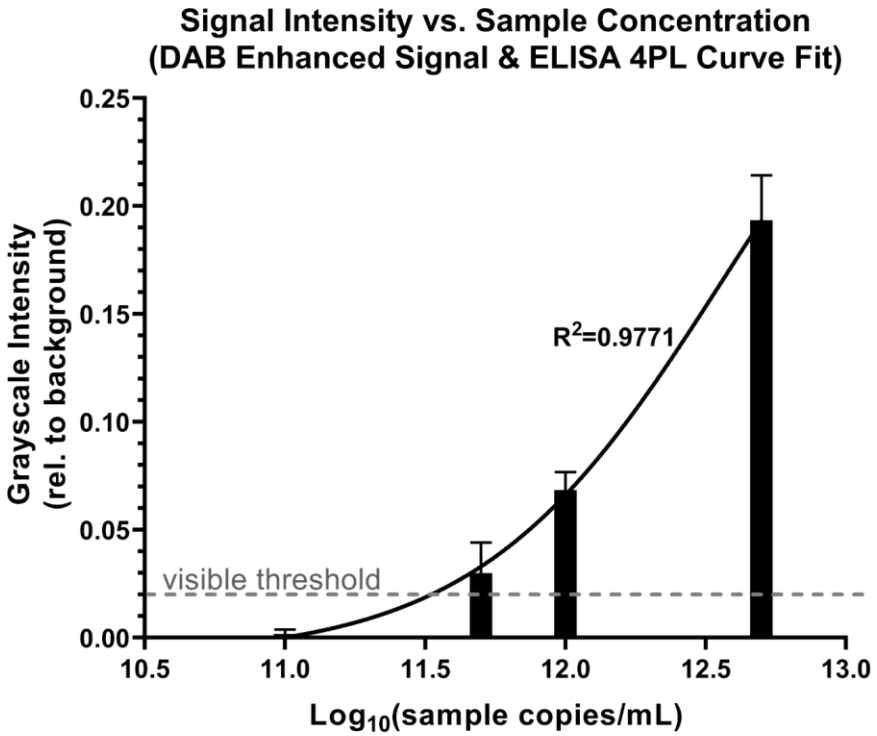

Figure 6.6 The DAB Enhances signal on our fully dried 2DPN produces a predictable signal increase in relation to sample concentration (ssDNA amplicon model) increases.

6.3.5 Reagents Retain Activity After 28 Days of Dry Storage.

Incorporating all necessary reagents pre-dried on the 2DPN improves ease-of-use by eliminating reagent preparation steps. It also simplifies storing, packing, and shipping of the devices, which is critical for the translation of 2DPNs into clinical use. Other researchers have dried different individual components of the DAB/HRP/H_2O_2 reaction for LFIAs and 2DPNs, but prior to this work, no one had successfully demonstrated and measured LOD improvements of all components in a dry-state[28,15].

We tested the ability to dry and store all reagents to determine the practicality of this device for real-world use. After drying, assembling, and storing all components of the 2DPN device for 1, 7, and 28 days, we still observed similarly detectable signals. There were no statistically significant decreases in the signal intensity after 7 or 28 days of dry storage for a sample concentration of 5E12 dsDNA copies/mL (hybridized Probes 1 & 2, **Table E. 1**). Although the high concentration sample of 1E14 copies/mL on the 2DPN did show a significant decrease in signal intensity after 28 days, the intensity remained well above the visible threshold (Figure 6.7). These results show that our dried SA-HRP-AuNPs, DAB, and H_2O_2 retained activity for at least 28 days of dry storage on a fully assembled device. Because signal intensity at lower sample concentrations did not significantly degrade, we conclude that the sensitivity of our device is the same before and after 28 days of storage. In the future, lower sample concentrations and devices older than 28 days can be tested to establish the LOD of dried 2DPNs after long-term storage.

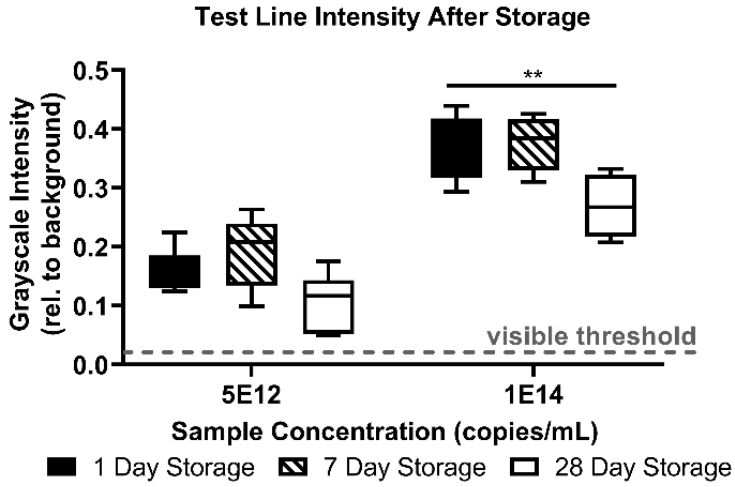

Figure 6.7. Quantification of test line intensity. Background-subtracted grayscale test line intensity for hybridized DNA samples run on fully dried and assembled 2DPNs imaged after 60 minutes. Visible threshold at 0.02 indicated by dashed line. (n=6, **indicates p <0.01 in Dunnett's multiple comparison with 1 Day Dried Storage 2DPN as control).

6.3.6 2DPN Detects Amplified MERS-CoV TARA Products.

To extend the application of our device beyond detection of a model probe, we tested diluted TARA product on our dried 2DPN (Figure 6.8A, replicates shown in Figure E.6). The TARA reaction can produce detectable PNA strands at a concentration ~100x higher than the initial target RNA concentration at room temperature in as little as 15 minutes[108]. The average background subtracted grayscale signal produced by the TARA-amplified sample (10X diluted) after 60 minutes on the dried 2DPN was 0.08 (Figure 6.8B). Based on the ELISA calibration curve, this translates to a sample concentration of 2.7E12 copies/mL (Eq. 2, **Figure E. 4**). Given that 2E11 copies/mL of target RNA was input into the TARA reaction, and the TARA reaction was diluted 1:10, the estimated concentration of the TARA-amplified sample was 2.7E13 copies/mL. This confirms that TARA amplifies concentrations ~100-fold.

Based on these results, combining TARA and 2DPN technologies could result in an LOD as low as 5E9 copies/mL for the assay as a whole. Clinical samples from lower respiratory samples (aspirate) of MERS-CoV infected patients had a mean virus concentration/ml of 5.0E6 (maximum 6.3E10)[24]. With a combination of TARA and our 2DPN, we could detect samples in the upper range of clinically relevant concentrations without the need for heating or multiple pipetting steps. Test results can be produced within as little as 1 hour (based on a 15-minute amplification, 5-minute sample and reagent application, and 40 minutes of signal enhancement on the 2DPN). Further optimization or increased amplification time of the TARA reaction and additional characterization of the AuNP-SA-HRP signal enhancement are feasible to further improve overall LOD. Specifically, the amount of signal enhancement on the 2DPN can be further improved by characterizing the HRP reagent, as the protein used in this assay was a pre-conjugated, proprietary SA-HRP product with an unspecified amount of HRP molecules attached.

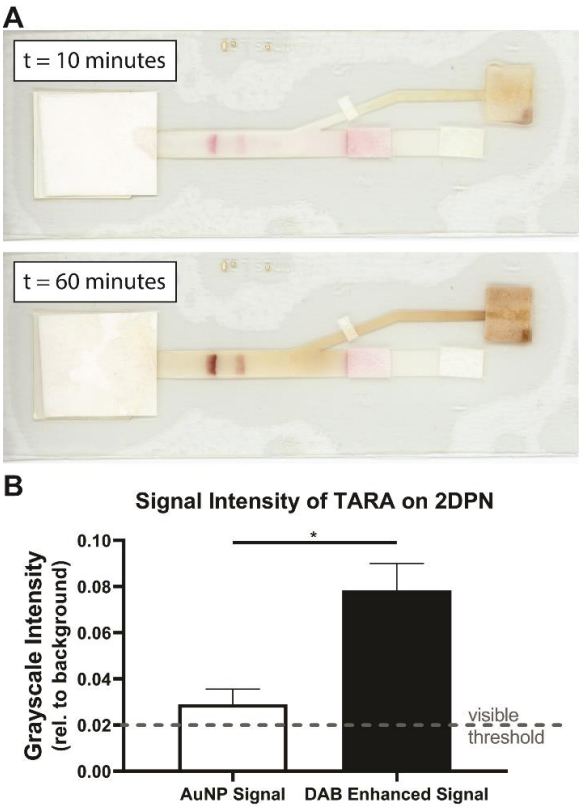

Figure 6.8. Results of TARA sample (1:10 dilution in PBST) on a dried 2DPN (A) Scans taken of a representative test at 10 and 60 min. (B) Test line signal intensity analysis of TARA sample on 2DPNs before and after signal enhancement (paired t-test, *p<0.05, n=3, replicates shown in Figure E.6).

The detailed cost of materials for this platform can be found in Table E.6, which shows that the total cost of goods for this 2DPN is approximately 1.82 USD. Commercially available one-dimensional LFIAs with an anti-FITC test line and a biotin control are available from 3.75 USD[127]. Reported cost estimate calculations for other lab based LFIAs for viral detection platforms range from 0.80[126] USD to 12.70[128] USD. While the general cost of materials for any platform should be considered for theoretical commercial translation, overreliance on cost reduction as a feature of POC designs without consideration of other cost factors is an issue we do not want to promote[129]. While this platform is considered low-cost from a materials perspective, we recognize

that significant manufacturing costs may be a barrier to commercialization. Although the assembly of 2DPNs is not as straightforward as that of one-dimensional LFIAs, we anticipate that robotic advancements such as pick-n-place, cut-sheet manufacturing, and roll-to-roll will enable scale up of devices.

6.3.7 Comparison to Commercial Assays for Detection of Amplified Nucleic Acid Samples

Imaging timing for LFAs is a critical factor for many commercial platforms including the Millenia "HybriDetect" which is often used for detection of amplified RPA samples (discussed in Chapter 7) and the USTAR Biotechnologies LFAs that have been used in previous work (Chapter 4.3.2 Microheater Incubation for the detection of *vibrio cholera* via LAMP). Specifically, these Lateral Flow Dipsticks (LFD) claim rapid results in as little as 5 minutes after sample and buffer initiation, however, these LFD are also known to eventually produce false-positive test lines if a user waits too long (15 minutes post-flow initiation) to look at or image the test. This is a concerning factor if developers hope to use LFA test line intensity for quantification of sample concentration at the point of care, where workflow timing may be highly variable depending on how many samples the practitioner is handling. For USTAR strips specifically, results read after 30 minutes are considered invalid[119] and for Milenia results read after 15 minutes are invalid and are typically read immediately after the 5-minute incubation mark due to high rates of false positive test line development over time.[120] Additionally, Milenia LFDs require storage temperatures between 2 and 8°C while USTAR strips are packaged in individually sealed aluminum pouches with desiccant and stored between 2 and 30 ℃.

Our desire for a commercial standard for which we could use as a benchmark for the 2DPN results led to larger questions about variability of LFA and LFD outcomes. While we found that the USTAR LFA LOD of 1E9 copies/mL was comparable to the 2DPN when using TARA model samples (Figure 6.9), we also found that USTAR Test Line intensity results could not be used as a quantitative indicator of sample concentration (not shown). Several studies have discussed the use of optical analysis with smartphones[130] and other commercial devices (such as Millenia® POCScan Reader for the Milenia LFDs)[131] to improve interpretation of LFA's but the majority of this work is on protein analytes, not isothermal NA assay amplicons. The use of optical readers reduces user-to-user variability when interpreting and standardizing a threshold for

positive/negative results. However, it is difficult corelate isothermal nucleic acid amplicon output with an estimated input without extremely thorough testing of that specific reaction setup, primer set, and chosen LFA readout. LAMP and RPA are both highly efficient assays which can produce large amounts of amplicons sometimes resulting in a LFA phenomenon known as the hook effect which is caused by excess target analytes binding to the test line in such large amounts that AuNPs used to visualize those analytes cannot bind – thus producing a reduced signal sometimes interpreted as a negative result. For this reason many NA amplicon samples are diluted prior to application on a LFA or LFD, but if the original efficiency of the amplification reaction is greatly impacted by poor storage conditions or agents commonly found in biological samples that inhibit or inactivate the enzymes responsible for amplification and AuNP binding, the overall sensitivity of the assay could be compromised by further dilution. Lyophilization, sample preparation steps, and internal amplification control mechanisms[132] mediate some of these concerns, but they can still prove difficult to control for outside of the lab. Because it is nonenzymatic and has highly stable components, Crosslife Technologies' TARA reaction might be more suitable for POC deployment if it can be proven efficacious at clinically relevant sample concentrations.

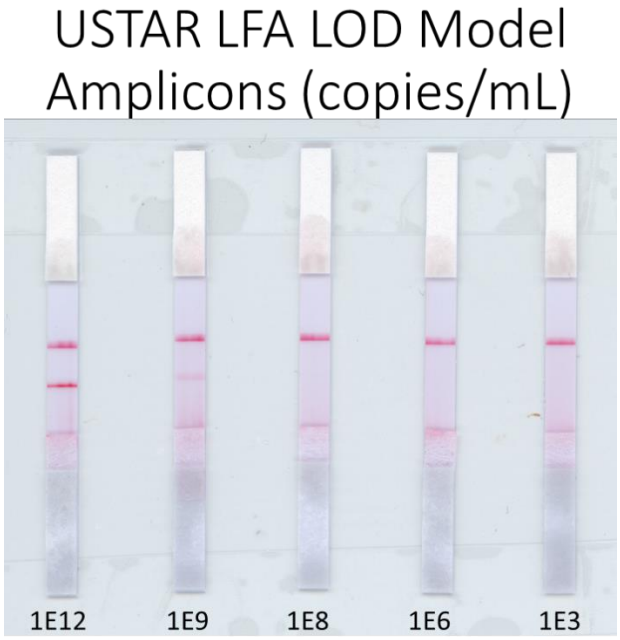

Figure 6.9 Limit of detection results on USTAR LFA with model (ssDNA) amplicons

6.4 Conclusions and Future Directions

This work demonstrates a fully dried 2DPN design that automates the flow of a signal enhancement solution to improve the LOD of nucleic acid samples labelled with FITC and biotin. We improved upon previous 2DPN designs that use DAB as a signal enhancer by reducing the number of fluidic inputs and detection time, and by incorporating dry storage of all necessary reagents, including a source for reactive hydrogen peroxide. Our fully dried device has shown versatility in the ability to detect multiple types of nucleic acid samples, including PNA products from a room temperature RNA amplification reaction, TARA. The applicability of this 2DPN can be extended to detect a variety of pathogens and incorporate other amplification reactions with FITC and biotin tagged products. The HRP signal enhancement retains activity after 28 days of dry storage on a fully assembled device. The fully dried and assembled device (after a total of 60 minutes run-time) achieved an LOD of 5E11 copies of ssDNA per mL, comparable to other hybridization-based nucleic acid detection devices. When combined with the current TARA reaction, the LOD can reach as low as 5E9 target copies/mL and can be further reduced by using other NA amplification methods with higher outputs. The signal in the detection zone is maintained well after the sample is run, reducing the need for strictly timed reading of results.

These critical advancements enable sample detection and enhancement of amplified NA products with an average signal enhancement of 116% for samples above the LOD. Our 2DPN produces a signal intensity increase much greater than commercially available gold or silver enhancement solutions and requires only simple rehydration of pads and folding to perform. We determined not only the increase in signal intensity, but also how that increase affects the true LOD (in copies/mL), a practice we believe should be applied to the design of all LFIAs incorporating signal enhancement agents. This proof of concept for a fully dried, deployable 2DPN shows promise for detecting many other pathogens beyond MERS-CoV and can be employed with other nucleic acid amplification techniques. This fully dried, automated viral detection platform has shown to be a successful proof of concept with multiple types of NA samples. These results are promising for the future applications of this technology at the POC.

7. DEVELOPMENT OF A STRAND-DISPLACEMENT PRIMER APPROACH TO REVERSE-TRANSCRIPTION RECOMBINASE POLYMERASE AMPLIFICATION FOR REDUCED FALSE-POSITIVES IN LFA'S

7.1 Rationale

As I described in 1.3.5 Recombinase Polymerase Amplification (RPA), RPA has been touted as a promising method for rapidly amplifying NAs at one consistently low temperature. A kit developed by the company Twist Dx designed specifically to allow RPA amplicons to be detected on LFAs, called the nfo kit, was discontinued in mid-2020. The RPA nfo kit design uses a combination of two primers (one forward and one reverse), and a probe which invades the median of the sequence and is then cut by Exonuclease III at THF residue on the prove to produce amplicons between 100 and 200 bp long with one molecular label on each end for detection on an LFA.[133] While this method proved successful in many publications, recent work by Wu et al. showed that even with the nfo kit/probe-cutting method there were difficulties with false-positives on their LFAs due to probe–primer complex formations.[134] Several scientists have modified this original design for their own needs with, and without access, to the nfo kit including Jauset-Rubio et al. who removed the molecularly tagged probe in favor of a oligo-tagged forward and reverse primer set with pleasing success[46], and J. Qian et al. who recently utilized a design similar to the nfo kit but removed the need for the Exonuclease III/THF cutting and produced excellent methods for utilizing reverse transcription for SARS-2-CoV detection.[45] This work applies the use of labeled primers described by Jauset-Rubio et al. and reverse transcription methods by J. Qian et al. (referred to as JR and JQ respectively for the remainder of this chapter).[45,46] From this and other literature described in 1.3.5, I aim to design and test a method which utilizes both the forward and reverse primers as molecularly labeled ends, and incorporates toehold-mediated strand-displacement probes (SD-probes) with the intent to reduce the probability of primer-dimer formation. The sequence of steps for this novel reaction design is detailed in Figure 7.1 below, where a reverse transcriptase enzyme first converts viral RNA into cDNA, which the molecularly labeled primers can then attach to via Recombinase. In order for the primers to fully anneal to the target strand, the strand-displacement probes must be dislocated. After each primer fully invades the template strand, having shed their displacement probes, a polymerase enzyme elongates each

strand to produce two separate duplexes, each with one of the original primer labels. This cycle repeats until duplexes with both molecular labels form over several cycles, the bulk of which are detected on an LFA via the molecular labels (Biotin and FAM).

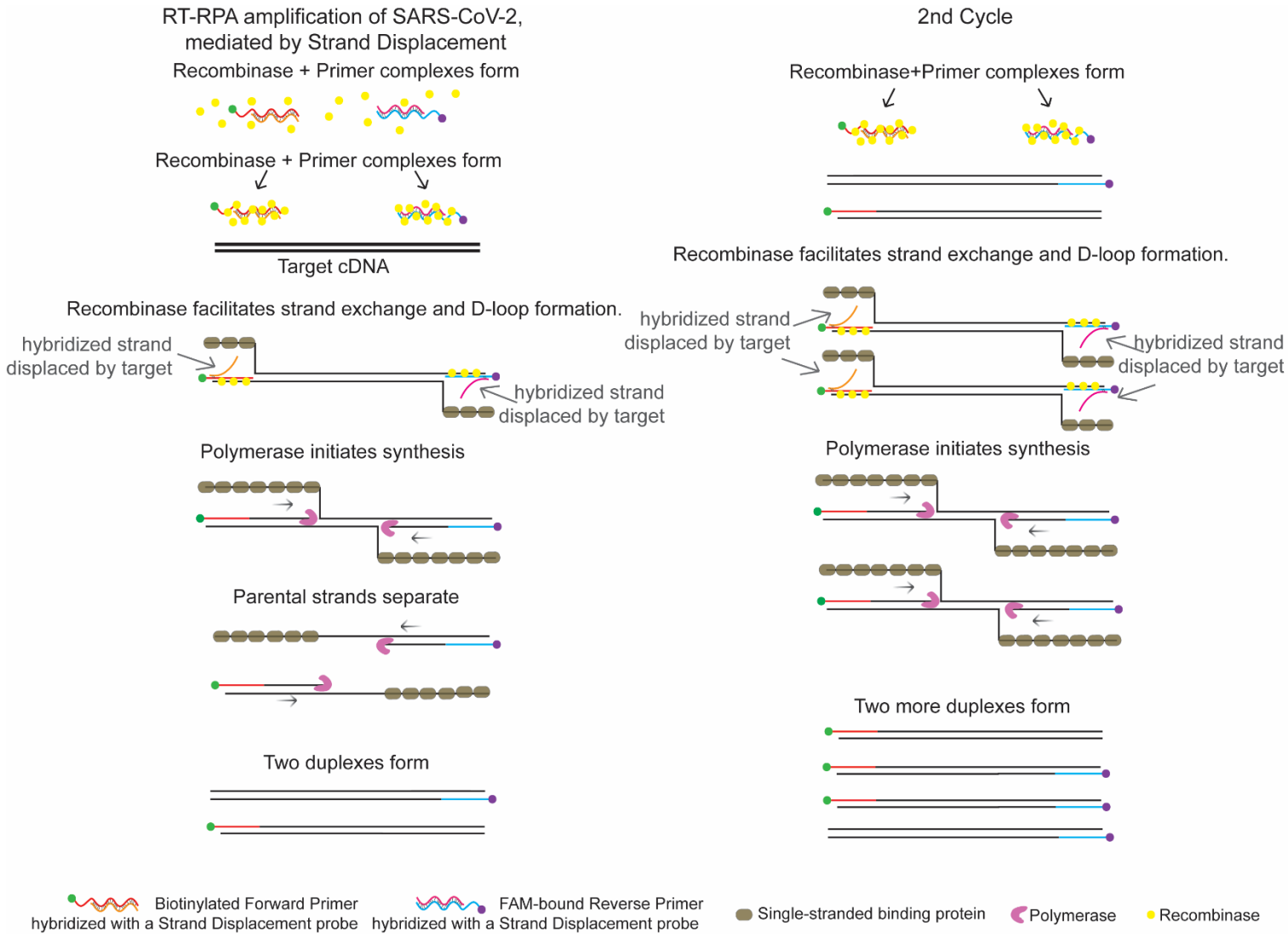

Figure 7.1 Schematic of Strand Displacement RPA.

As I described in Section 1.3.5, the toehold-mediated strand-displacement mechanism utilizes a short, single-stranded oligonucleotide sequence complementary to the median of the primer strand which is annealed to the primer prior to reaction initiation, leaving a partial duplex with an unbound 3' toehold on the primer. The displacement of the probe is initiated by the toehold hybridizing with the target strand, which then displaces the probe altogether. Other toehold mediated strand-displacement mechanisms applied to certain primers in other isothermal assays, like LAMP, have been shown to reduce false positive readouts with LFAs and real-time fluorescence systems,[123,135] and is a predictable and useful molecular tool in its own right.[47] From this background, it is possible that applying this method to reduce false positives resulting from primer-dimers produced by my labeled primer design with prove useful. Primer-dimers are a common concern in molecular diagnostics. Self-dimers (where a primer hybridizes to another primer of the same sequence) and cross-primer pairs (often call hetero-dimers where two primers, each of a different sequence, hybridize to each other) are the two primary primer artifacts which cause these issues. Any primer set can result in primer-dimers, but this is avoided by careful primer design and selective testing of primer pairs to find the best set. Energetically, combining a reverse transcription assay with a strand-displacement step is expected to cause a measurable reduction in efficiency of the reaction, if this is deemed a problem several reaction endpoints can be tested. Based on this reasoning and literature I endeavored to assess whether a highly efficient double labeled primer design incorporating toehold mediated strand displacement could be used for direct isothermal detection of SARS-CoV-2 using SD-RT-RPA.

7.2 Materials and Methods

Primers were designed using NCBI Primer-BLAST according to TwistDx recommendations targeting the 24139 to 2425nt region (part of the S protein section) of SARS-CoV-2.[133] Specifically, template gene sequence within the spike (S) region with few direct or inverted repeats and GC content between 40-60%, final amplicon length between 100-200 nucleotides, each primer is between 30 and 36 nucleotides long, GC content between 20-70%, melting temperature between 50-70 °C, maximum of 5 mononucleotide repeats. SD-probes were manually designed via OligoAnalyzer™ Tool (Integrated DNA Technologies, Inc.). Melting temperature, ΔG values, and secondary structure of hybridized and non-hybridized primers and their respective SD-probes were

analyzed using NUPACK analysis (nupack.org, ©Caltech) and OligoAnalyzer™ Tool (Integrated DNA Technologies, Inc.). Primers and SD-probes were ordered from idtna.com. Strand displacement probes were annealed to their respective primers by mixing equal volumes of probe and primer (each suspended at a concentration of 100μM in IDTE, pH 8.0), then incubated in a PCR machine at 95 °C for 3 minutes followed by 0.1 °C/s cooling to room temperature. The hybridized SD-primers were then diluted to 50 μM in nuclease free water and stored in aliquots of 10 μL at -20°C. All primers discussed in this work are listed in Table F.1 and all SD and other hybridization probes are listed in Table F.2.

7.2.1 10uL reactions in Real-Time PCR machine

50 uL reactions following TwistDx recommended protocol were performed in either an Axxin T16-ISO Machine(Axxin, Fairfield Australia) with a 2mm stainless steel ball bearing to each reaction mixture for mixing, or in a Real-Time PCR Machine with manual mixing occurring at 5 minutes. Reaction contents included 1 lyophilized 2.4 μl of 10 μM forward primer and 2.4 μl of 10μM reverse primer, 29.5 μl Primer Free Rehydration buffer, 1 μL EvaGreen (20X), 1 μL ROX™ (50x), template and water to 11.2 μl, resulting in a total volume of 47.5 μl which is then added to the TwistDx lyophilized reagent pellet. 2.5 μl of 280mM Magnesium Acetate (MgOAc) is added and mixed to start the reaction. Reactions were terminated with 2 μL of 0.5mM EDTA immediately after reaction completion. Samples were then analyzed via LFA and gel electrophoresis.

7.2.2 10uL reactions in Real-Time PCR machine

Isothermal amplification reactions were based on the TwistAmp Basic RPA Kit (TwistDx) and work published by JQ et al. with adjustments described below.[45] 0.5 μL of forward and revere primers at 10 μM were pipetted into each 200 μL PCR tube and mixed. Then a Master Mix containing 1 lyophilized pellet resuspended in a solution of 38 μL rehydration buffer (TwistDx), 1 μL RNase H (5U/μL) (NEB), 0.5 μL SuperScript IV RT (200 U/μL) (ThermoFisher Scientific), and 0.5 μL EvaGreen (20X), 0.5 μL ROX™ (50x), was activated with 1 μL 700 mM magnesium acetate followed by thorough mixing with a pipette. 8.2 μL of this master mix was dispensed into each tube, followed by an addition of 1 μL of input template (RNA, Accuplex virus, or nuclease

free water for negative controls), mixing the reaction by pipetting, and incubating at 42 °C for 25 min. For reactions with unlabeled forward primers, following JQ et al.'s protocol, a hybridization mix was prepared by combining 1 µL biotinylated probe at 5 µM (CCMS069) with 19 µL 10 mM Tris pH 8. 20 µL of hybridization mix was added to each reaction after amplification, and samples were heated at 94 °C for 3 min followed by a cooling step at room temperature for 3 min.[45]

7.2.3 LFA/LFD and gel electrophoresis analysis of amplicons

For 50 µL reactions (early experiments), 10 µL of the reaction mixture was mixed via pipetting before 40 µL of commercial LFIA wash buffer and pipetted onto a USTAR LFA (cat. no. D003-03, USTAR Biotechnologies, Hangzhou, China). LFAs were scanned with an Epson V850 Pro Scanner (Model J221B, Epson America Inc., Long Beach, CA).

For 10 µL reactions, 50-80 µL of Milenia GenLine Buffer (Milenia Biotec, Gießen, Germany) was added to each reaction well, equaling 100uL total, mixed by pipetting, and a Milenia HybriDetect strip (MGHD 1) was added to each tube standing upright. The LFD strip results were verified and imaged between 5 and 10 minutes after LFD insertion. Images were taken with a Samsung Galaxy S21 phone under consistent lighting and subsequently analyzed via a custom MATLAB script to establish background-corrected test line intensities.[111,123] The visible threshold (visual cutoff for interpreting a test line as positive) of the background normalized grayscale intensity was set to 0.02 for all signal analysis according to Phillips *et al.*[123]. The remaining fluid after LFD analysis was then used for gel electrophoresis.

After samples were processed with Monarch® PCR & DNA Cleanup Kit (T1030S, New England Biolabs Inc., Ipswich, MA), 2 µL of 6X GelRed Prestain Loading Buffer with Orange Tracking Dye (41010, Biotium, Fremont, CA) was added to each ~15 µL eluted sample. Samples were analyzed via gel electrophoresis on a 2% agarose gel containing ethidium bromide with 1X TAE buffer ran at 100 Volts for 50-55 minutes. 10 µL of Thermo Scientific™ GeneRuler 50 bp DNA Ladder (SM0373) was used as a standard and gels were imaged with a 15 second exposure (c400, Azure Biosystems, Dublin, CA).

7.3 Results and Discussion

7.3.1 Primer testing and early reactions without reverse transcriptase

Primer design is a key factor for RPA, I designed and tested several of my own primers targeting the 24139 to 2425nt region (part of the S protein section) of SARS-CoV-2 using NCBI BLAST and following the DNA Amplification Kits Assay Design Manual from TwistDx.[133] From my initial 5 primer pairs, which were analyzed in the Real-Time PCR Machine (Figure F.1), I selected F1 and R1 as the best pair to continue testing. Experiments following the exact kit instructions (Basic) with my own primers and a plasmid template showed early success with 50uL reactions using both the isothermal Axxin real-time machine and Real-Time PCR Machine analysis. As you can see in Figure 7.1, Gel and LFA (USTAR strips, used only in this experiment) outputs showed that the strand displacement reactions did not produce strong positive bands suggesting that either: (1) the toehold exchange could not occur due to high affinity of the primer-SD probe complex, or (2) the SD probes themselves were elongating via polymerase activity after displacement resulting in a large amount of *unlabeled* amplicon product. The gel analysis seemed to indicate that both of these options could be true based on the extremely small band (less than 100bp) in the positive SDF1/SDR1 column where both primers were annealed to a displacement probe. Direct verification of RPA products by gel electrophoresis is impeded by the presence of high molecular weight proteins thus a postamplification purification step is required which may ultimately reduce product available for visualization.[136]

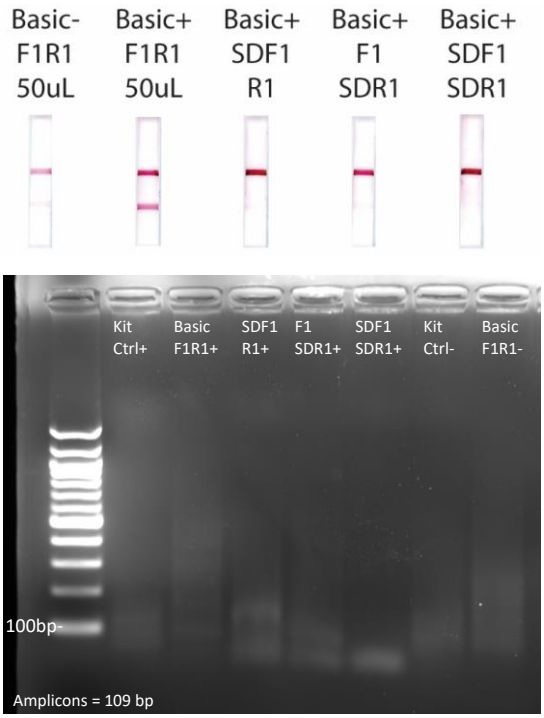

Figure 7.2 Testing molecularly labeled primers with various combinations of strand displacement toeholds in traditional 50uL RPA reaction using SARS-CoV-2 Plamsid provided by Raluca Ostafe as positive template.

These results suggest that a strand displacement mechanism may not be necessary to reduce false positives on LFA for this particular set of primers however upon trying to repeat these results the non-SD negative amplified consistently resulting in a false positive while the other SD-primer reactions continued to all show up as negative. After ruling out contamination and switching to the Millenia HybriDetect LFD's which are designed for RPA products, I tested new strand displacement probes (KB SD set 1.2) which shortened the length of the SD-probes from 22 bp to 16 bp and subsequently reduced the ΔG by -10 kcal/mole (details in Table F.2). These new SD primers also did not produce positive LFD results even when only one primer had a SD-toehold. This lack of positive test band on the LDFs suggests a lack of toehold displacement activity which inhibits all further amplification (Figure 7.3). The NUPACK analysis shown in **Figure F.2** supports this finding as it also shows there is no primer-dimer affinity because of the overwhelming affinity between the SD-primer pairs.

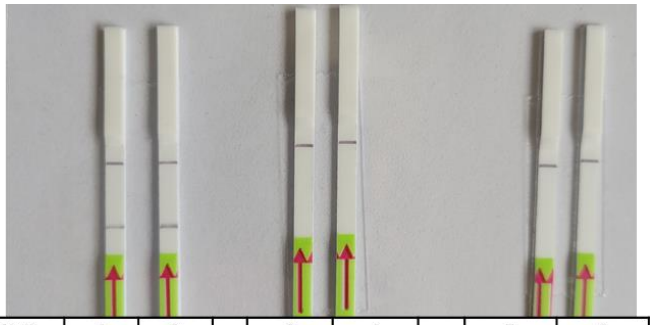

Well	1	2	3	4	5	6
Primers	KB FP1 RP1	KB FP1 RP1	KB SDFP1.2 RP1	KB SDFP1.2 RP1	KB FP1 SDRP1.2	KB FP1 SDRP1.2
Plasmid Template	+	-	+	-	+	-

Figure 7.3 LFD results of RPA primer pairs with and without annealed Strand Displacement probes in 50 µL reactions.

7.3.2 Modifying Primers from JQ et al.

At this time, we decided to begin testing with other primers from a recently published study by JQ et al. showing promising results with an approach similar to the traditional TwistDx design, but which separates the amplification and amplicon labeling into two separate reactions. The primer selection process they utilized was much more rigorous than ours in that they used high

and low template concentrations in their testing matrix. We were hopeful this new set of primers could prove more robust while we continued to investigate whether strand displacement activity could improve our reaction design. We were also hopeful that converting the reaction for a 10uL reverse transcriptase incorporated assay similar to their protocol would be more suitable for POC use and would take advantage of the fact that lower volume reactions do not need to be mixed to maintain sensitivity.[137] Upon switching to reverse-transcriptase with inactivated virus we encountered the opposite issue from our previous experiments – the strand displacement toehold-bound primers were now producing false positives on LFAs when they produced a signal at all (Figure 7.4 below). These SD-primer pairs were designed with mismatches near the 5' end of the SD-probe which reduced the ΔG of the duplexes closer to Jiang et al.'s recommended -18 kcal/mole for LAMP SD reactions and offered an opening at the 3' end of the primer for template recognition.[135] From these results we surmised that perhaps an even lower ΔG might be needed to allow a more favorable release of the SD-primer duplex. Though the false positive amplification in some of these samples is a concern, with LFD lines this faint (many were technically under the threshold considered to be positive) it is sometimes difficult to tell the difference between non-specific binding at the test line and low amounts of erroneous amplification.

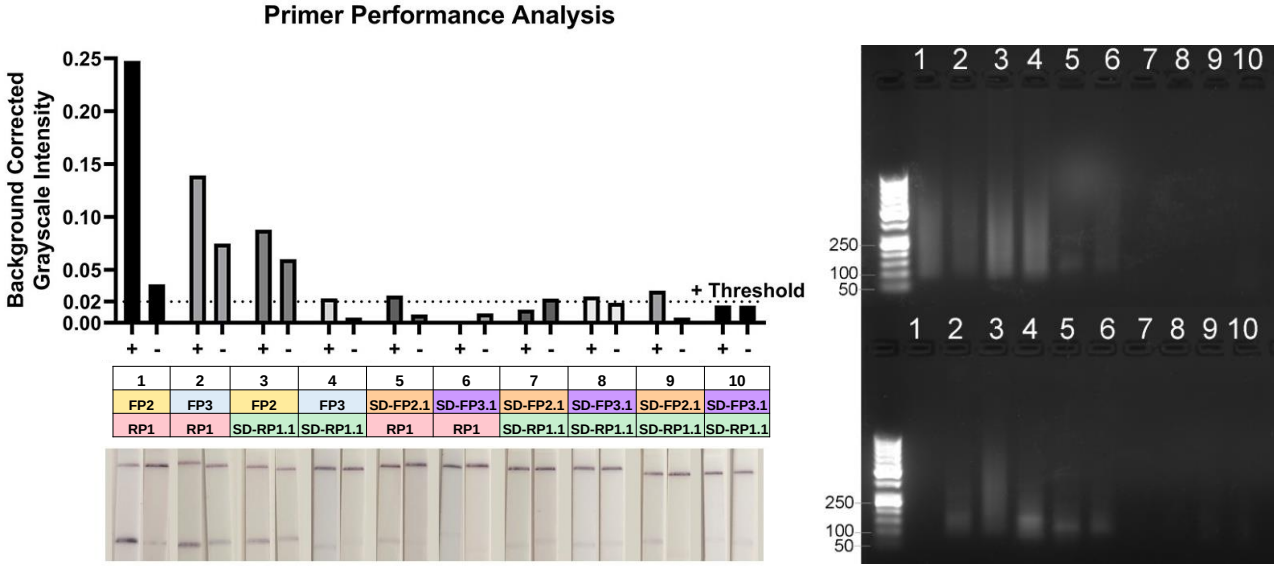

Figure 7.4 Testing of modified primers from JQ et al with SD-probes containing two mismatches near the 5' end. Left: LDF results and analysis of all samples. Right: Gel electrophoresis of all samples.

It is worth noting that due to this being a new technique in the Linnes Lab, there was a considerable amount of troubleshooting inconsistent results while also investigating protocol improvement, particularly in gel analysis of these RPA samples. In Figure 7.4 there does appear to be some sample loss in the gel lanes for samples 6-10. While it is clear that primer-dimers were reduced by the use of the SD-primers, there was also a general reduction in amplification. The LFD outcomes also still show very little difference between positive and negative controls. A deeper understanding of work improved strand displacement probe design for the new primers and while the use of SD-primers still reduces the intensity of the LFA test line for positive samples, there is also a reduction in false positives.

One particularly important aspect of this next experiment is the use of a 3'block on each of the Strand Displacement Probes. This is meant to inhibit the potential for these strands to act as primers for amplicifation after their initial displacement by the true template strand. Results from this experiment (Figure 7.5, below) are promising as there is in fact a reduction in false positive LFD intensities without a reduction in the positive LFD intensities, which suggests this modification improved the assay design considerably. The gel results also agree with the LFD outcomes where the addition of the 3' block on the SD toeholds did reduce overall amplification based on reduced banding for samples 8-10 in Figure 7.5 (C). This confirms that the toeholds were potentially acting as primers themselves once displaced by the template strand. This is easily mediated by the addition of the 3' block (a 5' block is not needed because polymerase activity is one-directional). If one wanted to exploit this SD-probe amplification activity instead of suppressing it, these SD-probes could also be labeled with their own unique molecular labels and be used as internal control indicators instead. This could prove to be a useful way to enhance the usefulness of this reaction design. Ideally, if the molecularly labeled strand displacement toeholds are *only* displaced in the presence of the true target template, you would then not only be initiating amplicon proliferation but would be releasing another set of somewhat unique primers (because of the length differences and mismatches) to be available for amplification. This could potentially be used as an internal amplification control mechanism which could be visualized on either an LFA or gel. More investigation would be necessary to back up this claim and ensure specificity is not lost.

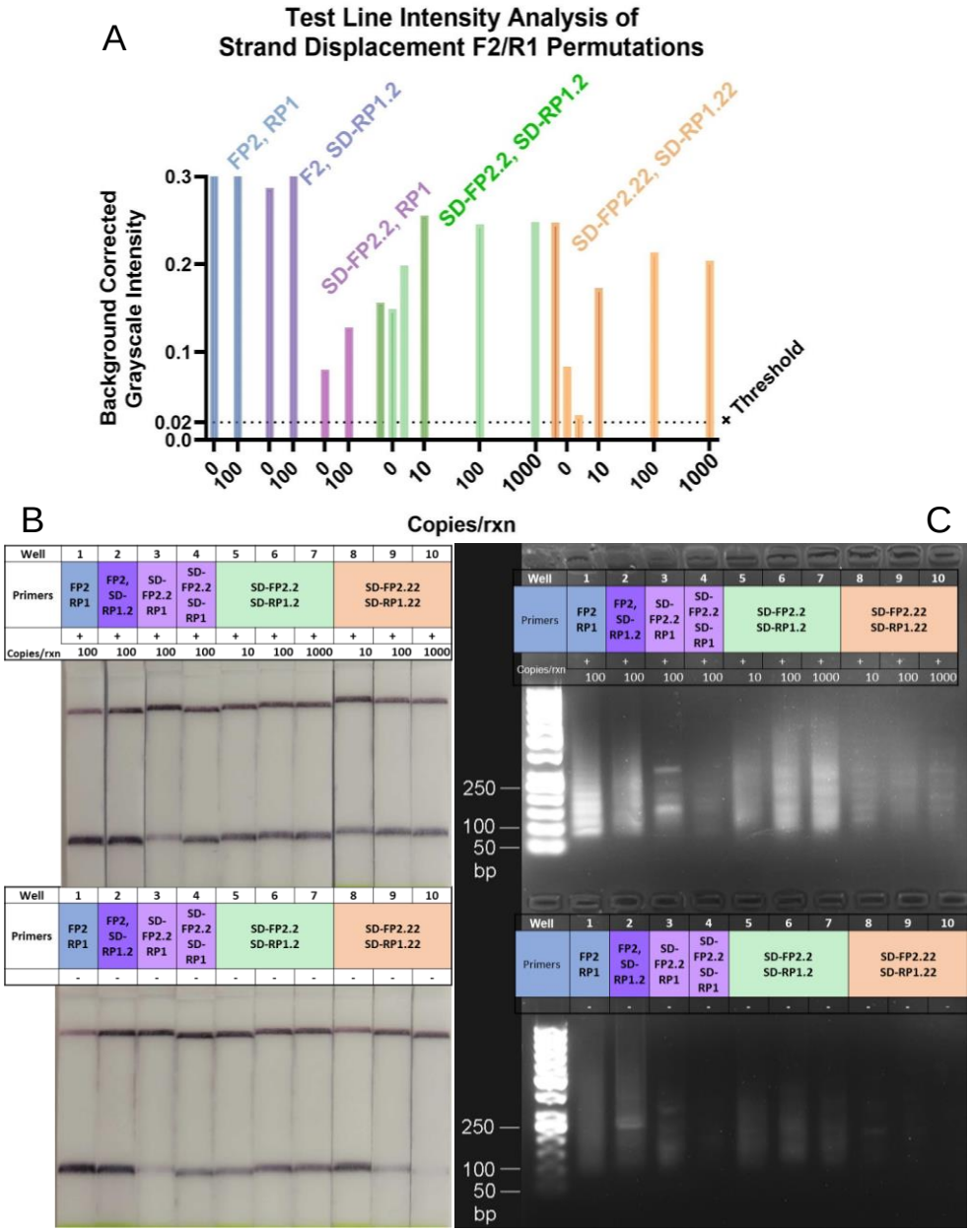

Figure 7.5 A direct comparison of strand displacement permutations using modified primers from JQ et al. (A) Test line intensity analysis of each LFD. (B) raw images of LFDs ~5 minutes after flow initiation. (C) Gel analysis of samples after PCR cleanup.

7.3.3 Replicating JQ et al.'s reaction as comparison

As a comparison to our reaction design I endeavored to replicate JQ et al.'s protocol and exact reaction. Unfortunately I struggled to replicate JQ et al's robust findings of 10 copies of input RNA required for consistent detection and was only able to detect 1000 copies/reaction after increaseing the biotinylated hybridization probe (CCMS069)[45] concentration from 5 µM to 10 µM. This is shown below in Figure 7.6, where there are imperceptible LFD lines for all samples treated with the 5 µM hybridization probe but as you can see in Figure 7.6 (C), there were clearly amplicons produced in that reaction that were for some reason not detected n the LFD. It is implied from these results that the hybridization probe was not able to bind to the amplicons for some reason.

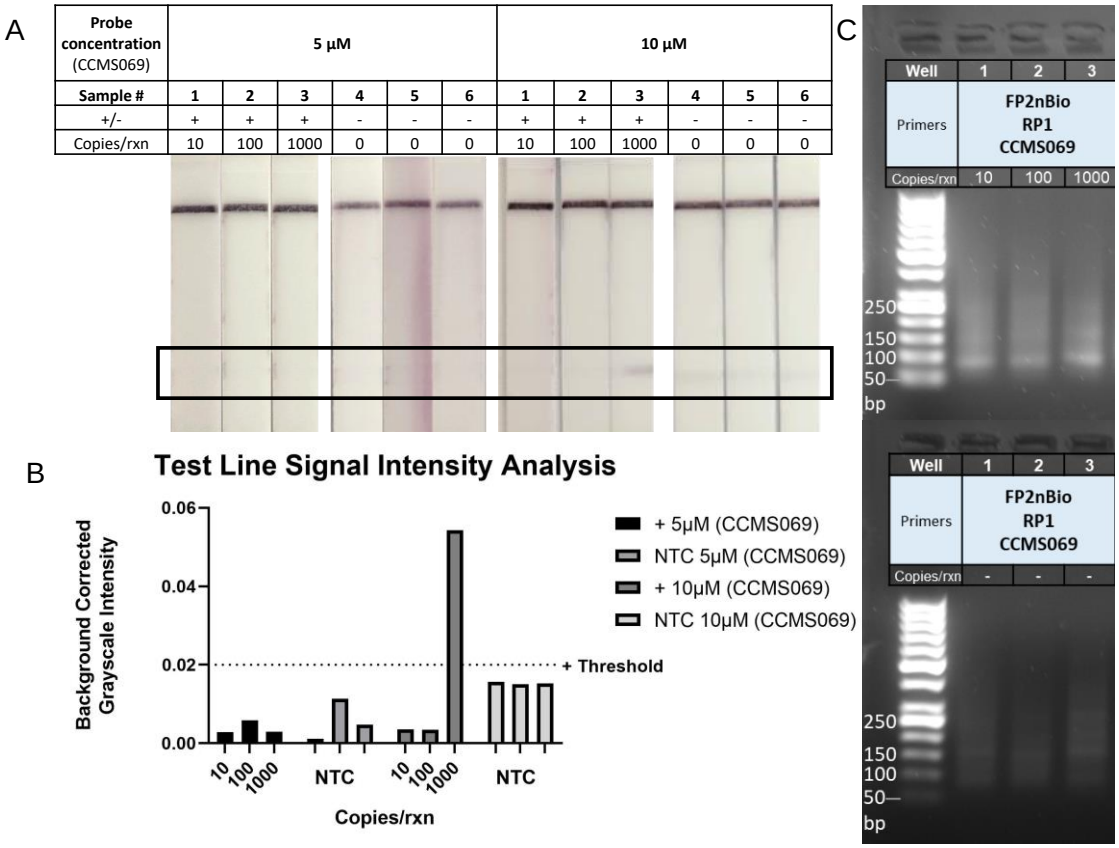

Figure 7.6 Replicating Qian et al.'s reaction as comparison. (A) Sample labeling and LFD outcomes. (B) Test line intensity analysis of all samples. (C) Gel Electrophoresis of the first six samples (5 µM hybridization probe used).

7.3.4 RPA is chronically prone to false positives with LFAs

It is difficult to explain why our results with this particular method (where both primers act as labeling units for the final amplicon) is so prone to false positive readings on LFAs and nonspecific amplification compared to work presented by JR et al. using 'tailed' primers (which seemed to show no such issue). It is worth noting that as LFA sensitivity has increased, the risk of primer-dimer induced false positive LFA outputs has also increased, especially considering this detection method cannot distinguish between different sizes of signal-creating molecules and shows every such molecule as a positive signal. RPA nfo kit compatibility with LFA's has generally been accepted, however there are other drawbacks where if the post-amplification sample is not adequately diluted, there will be false positives even on LFDs like Millenia Biotech's which is designed specifically for "compatibility with the TwistAmp® nfo kit".[133] It is also possible that the impacts imparted by enzymatic and crowding agent activity in TwistDx kits drastically changes the expected primer and strand displacement activity which could make primer artifacts more probable than in other reactions which may use less of these agents.[137–139] However it is most likely that secondary structures and primer-dimers are at play in our work purely due to primer affinity. I performed additional analysis of the Gibbs energy *G* on one set of primers from each study I've discussed so far (Figure 7.7 below) to estimate the probability of both self-dimers (where a primer hybridizes to another primer of the same sequence) and hetero-dimer pairs (where two primers, each of a different sequence, hybridize to each other). Interestingly, there were only two self-dimers to come out of this analysis with a ΔG greater than -9 or -10 kcal/mol, which is generally understood to be the value where primers begin to become likely to dimerize in PCR.[140, 141] The two concerning self-dimers occurred with KBFP1 where 8 base pairs overlap extremely well at the 5' end of the forward primer making for a favorable ΔG of -9.97 kcal/mol, and JRRP where 4 base pairs and other partial affinities contributed to a ΔG of -9.28 kcal/mol. If we are even more critical of the most probable hetero-dimer pairs, we also see that the JQ et al primers in this study could very well form a duplex detectable on a LFA with a ΔG of -8.14 kcal/mol. Although technically under the cut-off, this pairing is still likely and could explain why these primers consistently produced false positives throughout this study. It might be best to be excruciatingly critical of these primers if this labeled primer RPA system is tested again in the future and use an even more conservative cut off closer to -5 kcal/mol ΔG to ensure primer dimers are not probable.

Figure 7.7 Primer analysis using OligoAnalyzer™ Tool at idtdna.com of three sets of primers of interest.

Primer-dimers are a common design issue in highly sensitive molecular diagnostics and this issue with RPA has previously been mitigated primarily by the Probe method used in both the traditional nfo TwistDx kit and in JQ et al's work. These methods introduce a third sequence that binds to the RPA reaction in addition to the primers. Another recent work by Wu et al. showed that even with the nfo kit/probe method there were still difficulties with false-positives. [134] In Wu's work, the authors had to introduce carefully chosen base substitutions on the probe and the reverse primer to prevent probe–primer complex formation while maintaining amplification efficiency. While this mismatch method could reduce assay specificity if applied too liberally, the recommendations to avoid mismatches near the 3' end due to it being the elongation site, and to avoid substitution of distantly located bases on the probe and primer to maintain the template

recognition capacity were sound and eventually resulted in a robust assay. This approach could also be used to reduce hetero-dimers between the forward and reverse primer in my design. I've summarized the various approaches and results from these experiments in Table 4 below to simplify suggestions for future work.

Table 4 Summary of strand displacement toehold compatibility/results with molecularly labeled primers for improving RT-RPA false positive readouts on LFA's

Parameter	Method	Result	Conclusion	Recommendation
ΔG Adjustments	SD Probe Length	SD-probes over 15 bp are too complementary, no amplification occurs.	15 bp probes, when combined with bp mismatches to further reduce ΔG amplify well.	SD-probes between 10 and 15 bp are recommended.
	Perfect complement (probes homologous to primer)	Amplification inhibited when ΔG above -20	Toehold displacement energy should not exceed half hybridization energy of primer to target.	Do not use direct complements.
	Toehold mismatches at 5' end, middle, or 3' end of SD-probe	All mismatches effectively lower SD-primer duplex affinity (ΔG).	5' mismatch on SD-probe had greatest effect on displacement efficiency.	Use 5' mismatch on SD-probe first and add mismatches toward 3' end until ΔG is properly tuned. (Between -10 and -18 kcal/mole).
Tm Adjustments	Switching A/C mismatches to T/G	Increased SD-primer Tm did not appear to impact reaction efficiency or likelihood of false positives	Melting temperature is not a major factor so long as melting temp does not dip below 37°C	Aside from meeting basic recommendations this is not a major factor for future designs.
Toehold Blocks	3' Block (/3InvdT/) on SD-probe	Reduced nonspecific amplification shown in gel but did not improve LFA outcomes	3' blocks can be useful to maintain reaction sensitivity and efficiency	Use 3' blocks to ensure no erroneous amplification of SD-probes, unless they are acting as an internal amplification control mechanism.
Probe location on primer	3' end of primer	Strong inhibition of amplification resulting from unfavorable conditions for displacement	Toehold should not interfere with initial template recognition. Best placement is median of primer or at 3 end with mismatches there.	Adjust toehold location based on dimer analysis first and always leave several bp of toehold on 3' end to facilitate displacement likelihood. More data needed for toehold length tuning.
Primer Changes	Various Primer pairs	Primer pairs with lowest ΔG for self-dimer/hetero-dimer affinity perform best with and without SD probes.	Primer-dimer pair affinities should remain less than -9 kcal/mole but an even lower value is preferred.	Primer-dimer pair affinities should remain less than -9 kcal/mole but an even lower value is preferred.
	Primer mismatch on reverse primer	Wu et al. successfully reduced primer-probe dimers.[134]		

7.4 Conclusions and Future Directions

This work has shown that there is more investigation to be done in the realm of original RPA designs utilizing molecularly labeled primers with and without strand displacement toeholds in order to ensure robust translation of these assays from the lab into the POC. It is probable that many previously reported RPA assays in the literature were producing primer-dimers and that the nfo/THF nicking mechanism simply worked around that. This suggests a potential loss of efficiency and sensitivity that might be mediated by more rigorous primer design criteria and further investigation on that front. It is pleasing to think that the strand displacement toeholds could be useful for an internal control mechanism in future work where the strand displacement tuning is highly accurate. There is potential based on the summary matrix above to develop reliable approaches to this design and ultimately provide a unique yet robust and reliable assay. Future work could incorporate this low volume reaction into a paper membrane utilizing 8 μm PES as demonstrated by H. Ahn et al.[142] This would enable the reaction to be incorporated into another fully automated paper-based platform like Section 4.3.3'sReporting Results from Whole Platform Development Microfluidic Rapid and Autonomous Analytical Device (microRAAD) to Detect HIV from Whole Blood Samples.

8. CONCLUSION

This thesis provides several strategies for improving low-cost paper-based point-of-care diagnostics. Ranging from platform development and automated signal enhancement to novel nucleic acid amplification schemes, this work presents several key advancements necessary for the success of the next generation of infectious pathogen detection platforms. In Chapter 2, I described fabrication and characterization methods of custom designed inkjet-printed microheaters for sample incubation in low-cost paper-based POC diagnostic platforms. I also demonstrated resistance tuning with various printed designs, proving the versatility of these methods. These microheaters were further characterized in Chapter 3 with IR imaging and a COMSOL model which showed the resulting thermal consistency of the serpentine designs and confirmed adequate heat dissipation in the experimental paper chips. Chapter 4 results showed pleasing consistency of heat generation for several experimental sample types without the need for a microcontroller, and most notably showed comparable LAMP amplification results to the Real-Time PCR Machine controls for all samples incubated with a single AA battery. In Chapter 5 I detailed microfluidic fluid transport investigation and manipulation methods via 2-Dimensional Paper Networks and established a simple foldable automated 2DPN. The use of flow rate analysis of both modeled reagents (food coloring for visualization) and true samples enabled tuning of many facets critical to the flow consistency from each source pad throughout the platform. Chapter 6 demonstrates the fully dried 2DPN design that automates the flow of a signal enhancement solution to improve the LOD of nucleic acid samples labelled with FITC and biotin. We improved upon previous 2DPN designs that use DAB as a signal enhancer by reducing the number of fluidic inputs and detection time, and by incorporating and testing dry storage of all necessary reagents after 28 days, including a source for reactive hydrogen peroxide. Our fully dried device proved highly versatile in the ability to detect multiple types of nucleic acid samples and achieved an LOD of 5E11 copies of ssDNA per mL (5E9 target copies/mL with TARA reaction). Finally in Chapter 7 I demonstrate tuning a novel toehold mediated strand displacement mechanism incorporated into molecularly labeled primers for RT-RPA detection of SARS-CoV-2. This work provides insights and recommendations for future exploitation of toehold-mediated strand displacement for the mitigation of false positives on LFAs and primer-dimer proliferation in RPA reactions.

APPENDIX A. SUPPLEMENT TO CHAPTER 2

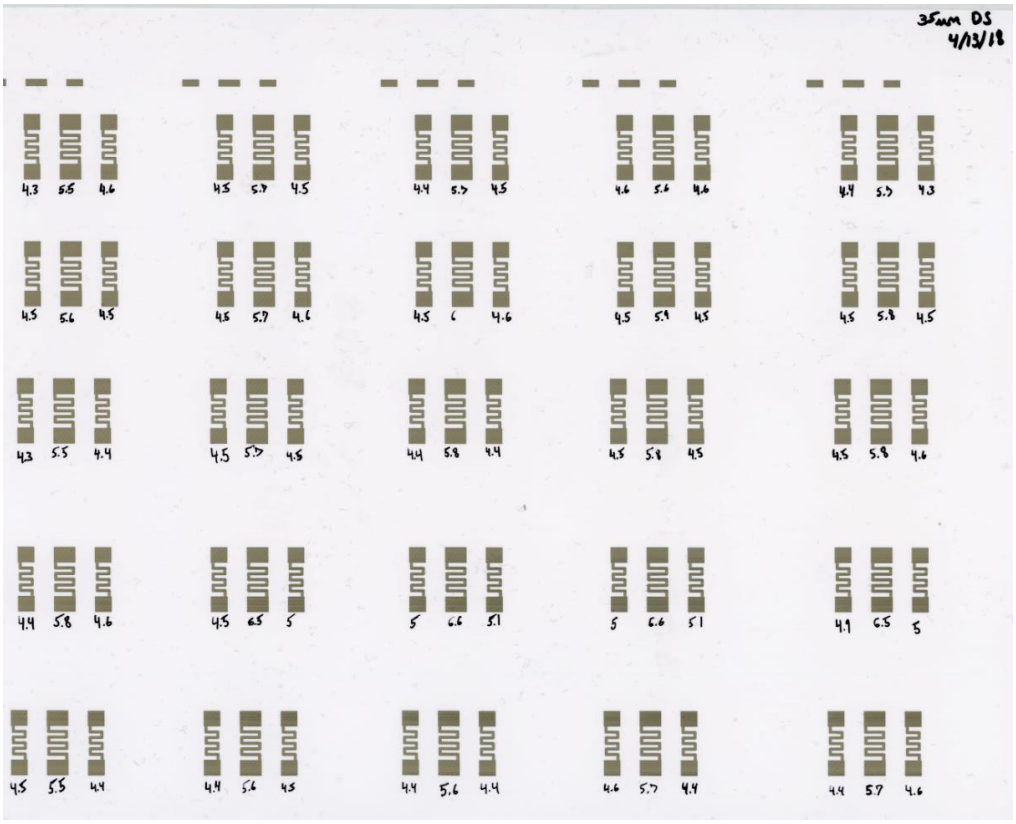

Figure A. 1. Early resistor printed on HP Glossy Photopaper

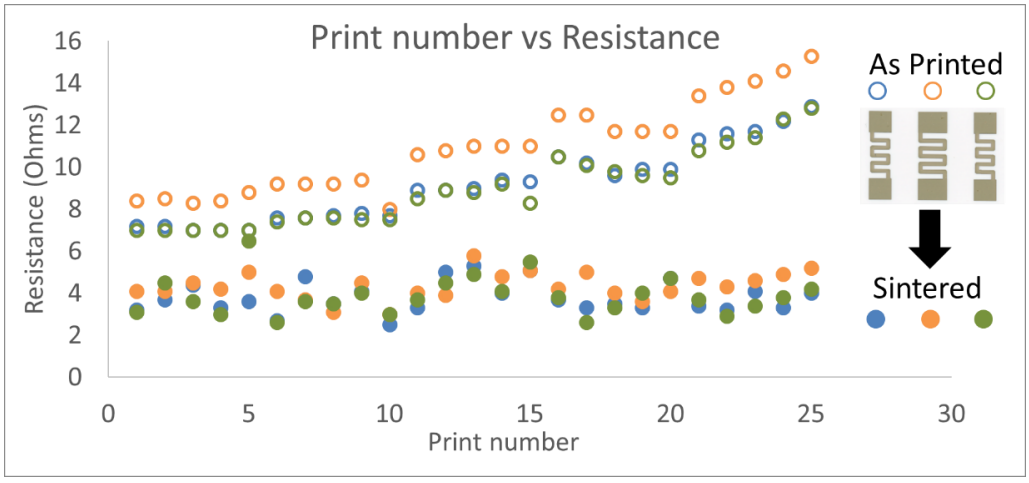

Figure A. 2. Resistance increases with the number of microheaters printed during a print job but can be reduced by sintering the resistor traces regardless of design. This early printing inaccuracy is managed by reducing total bulk printed microheaters per print job, and with improved nozzle selection and jetting optimization before printing.

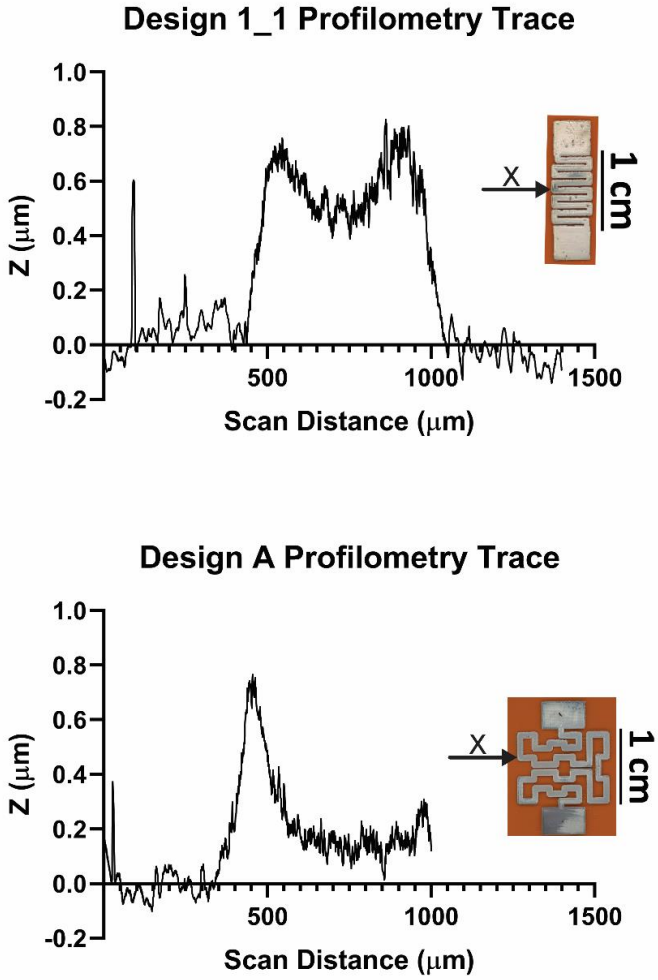

Figure A. 3. Representative graphs of profilometry data. The z height of the single layer nanosilver ink prints vary between the different designs and also appears to vary within a single print as well. There does appear to be some correlation between trace width and z height as thinner designs produced higher z height despite using the same print settings (35μm drop spacing etc.). Other sampling locations on different prints showed z heights between 1 and 1.3 μm.

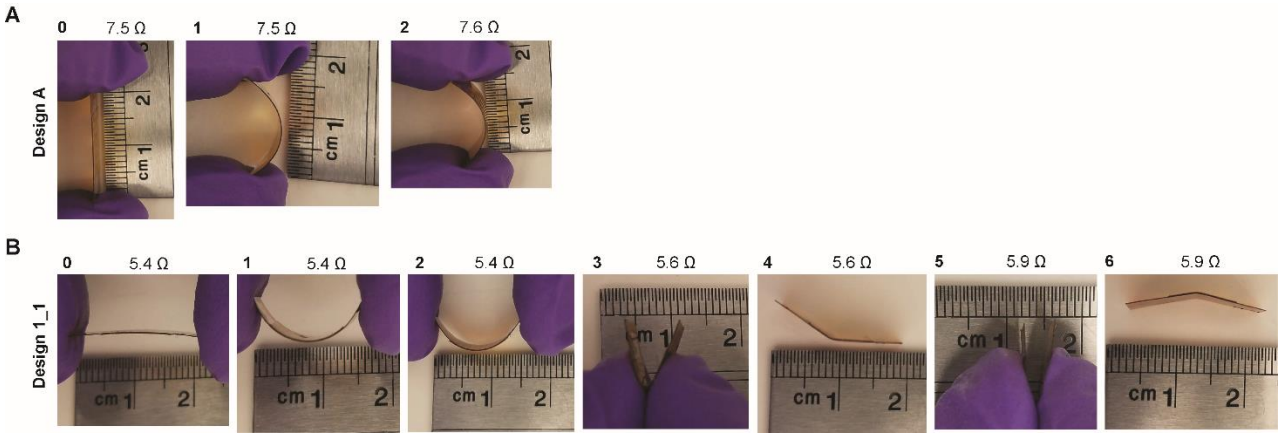

Figure A. 4. (A) Bending of Design A microheater for the durability test. Strain was calculated based on ΔL/L for the sample in each direction and resistance was measured after each deformation. Microheater traces for Design A tolerate bending resulting in a strain of Ɛ= 0.16 with only 0.1 Ohm change in resistance after bending in both the concave and convex directions. (B) A series of more aggressive bending on a single Design 1_1 microheater resulted in only minor resistance increases after each treatment. Strains for each bending treatment were Ɛ1=0.25, Ɛ2=0.25, Ɛ3=0.8, Ɛ4=0.7. The resistance was measured before and after each treatment using the two-point probe method (shown in Figure A.5).

Table A. 1. Material cost estimations per individual microheater for Design D and Design 1_1.

Item	**Cost (USD) per microheater (Design D)**	**Cost (USD) per microheater (Design 1_1)**
AgInk	0.035	0.01
Substrate	0.52	0.15
Filter	0.02	0.006
Total $	**0.58**	**0.17**

Figure A. 5. Low resistance microheaters are possible to create using the technique described in the main text. The design here has fewer serpentine turns resulting in a shorter path length. Specs: trace width: 0.529mm, path length: 24.264 mm, total heating area: 4 mm x 8.8 mm.

APPENDIX B. SUPPLEMENT TO CHAPTER 3

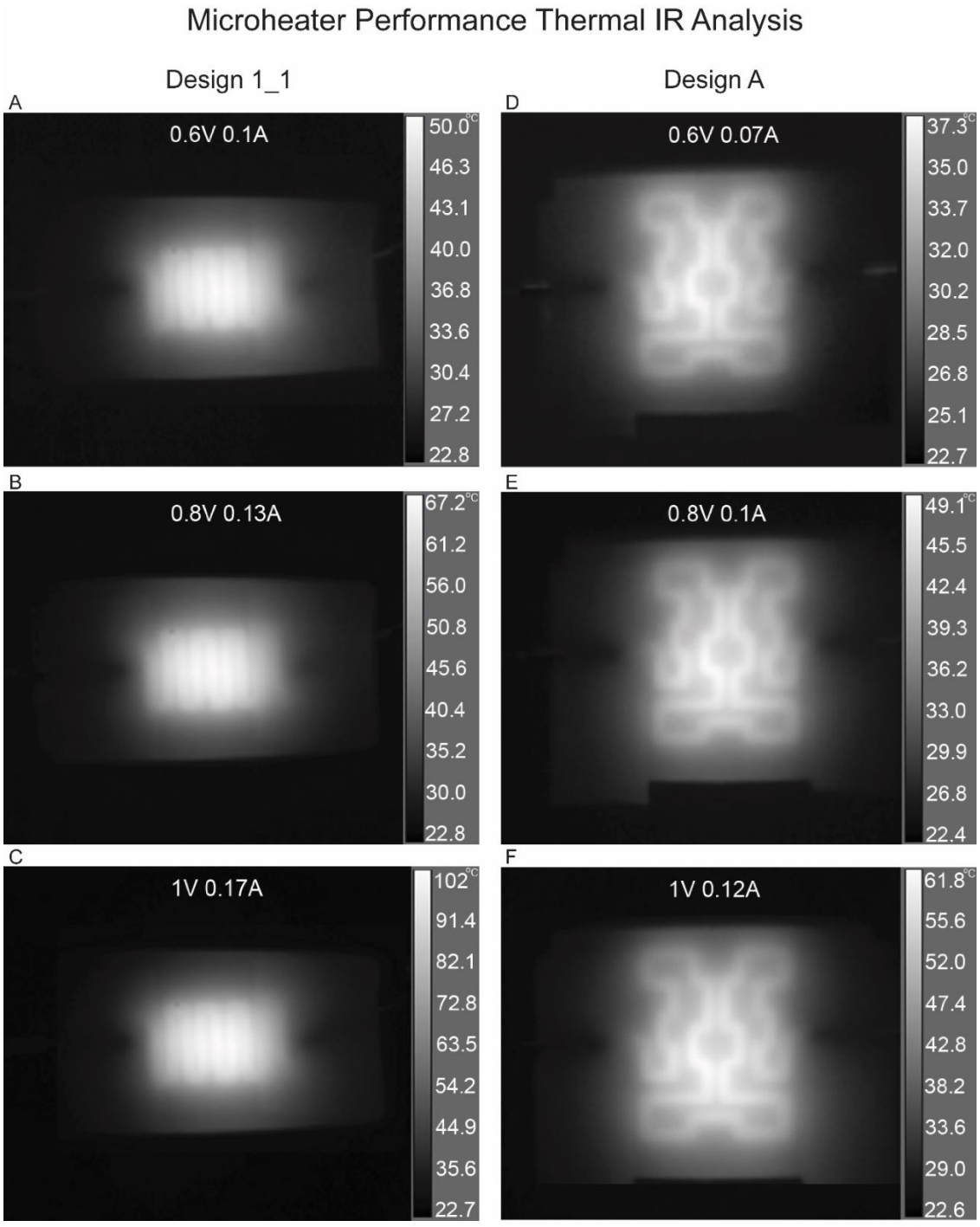

Figure B. 1. Microheater Performance Thermal IR Analysis Designs 1_1 and A. Voltages of 0.6V, 0.8V, 1V were applied to design 1_1 (A, B,C) and Design A (D, E, F) for five minutes each while under video recording with the IR camera.

Table B. 1. Microheater reusability repeated heating statistical summary

	Trial 1	Trial 2	Trial 3	Trial 4	Trial 5	Trial 6	Trial 7	Trial 8	Trial 9	Trial 10
Number of values	901	901	901	901	901	901	901	901	901	901
Minimum	25.00	24.10	24.20	25.90	25.10	26.70	24.80	24.70	24.40	24.80
25% Percentile	68.40	68.20	68.30	68.80	68.50	68.70	68.20	68.45	68.40	68.20
Median	69.20	69.30	69.30	69.60	69.40	69.50	69.00	69.30	69.30	69.20
75% Percentile	69.50	69.50	69.70	69.80	69.80	69.90	69.20	69.50	69.60	69.50
Maximum	69.60	69.70	69.80	70.00	69.90	70.00	69.70	69.50	69.70	69.50
Mean	67.87	67.74	67.90	68.27	68.08	68.28	67.75	67.88	67.88	67.76
Std. Deviation	4.52	4.89	4.71	4.55	4.59	4.31	4.68	4.70	4.87	4.67
Std. Error of Mean	0.15	0.16	0.16	0.15	0.15	0.14	0.16	0.16	0.16	0.16
Lower 95% CI	67.57	67.42	67.59	67.98	67.78	68.00	67.44	67.57	67.56	67.46
Upper 95% CI	68.17	68.06	68.21	68.57	68.39	68.56	68.05	68.19	68.20	68.07

Table B. 2. Tukey's multiple comparisons test for microheater repeated heating reusability

Test	Mean Diff.	95.00% CI of diff.	Significant?	Adjusted P Value	
Trial 1 vs. Trial 2	0.1326	-0.5614 to 0.8266	No	0.9999	A-B
Trial 1 vs. Trial 3	-0.03052	-0.7245 to 0.6635	No	>0.9999	A-C
Trial 1 vs. Trial 4	-0.4046	-1.099 to 0.2894	No	0.7065	A-D
Trial 1 vs. Trial 5	-0.2143	-0.9083 to 0.4797	No	0.9935	A-E
Trial 1 vs. Trial 6	-0.4075	-1.102 to 0.2864	No	0.6974	A-F
Trial 1 vs. Trial 7	0.1225	-0.5715 to 0.8165	No	>0.9999	A-G
Trial 1 vs. Trial 8	-0.01065	-0.7046 to 0.6833	No	>0.9999	A-H
Trial 1 vs. Trial 9	-0.01088	-0.7049 to 0.6831	No	>0.9999	A-I
Trial 1 vs. Trial 10	0.1084	-0.5856 to 0.8024	No	>0.9999	A-J
Trial 2 vs. Trial 3	-0.1632	-0.8571 to 0.5308	No	0.9992	B-C
Trial 2 vs. Trial 4	-0.5372	-1.231 to 0.1568	No	0.2966	B-D
Trial 2 vs. Trial 5	-0.3469	-1.041 to 0.3470	No	0.8572	B-E
Trial 2 vs. Trial 6	-0.5402	-1.234 to 0.1538	No	0.2888	B-F
Trial 2 vs. Trial 7	-0.01010	-0.7041 to 0.6839	No	>0.9999	B-G
Trial 2 vs. Trial 8	-0.1433	-0.8373 to 0.5507	No	0.9997	B-H
Trial 2 vs. Trial 9	-0.1435	-0.8375 to 0.5505	No	0.9997	B-I
Trial 2 vs. Trial 10	-0.02420	-0.7182 to 0.6698	No	>0.9999	B-J
Trial 3 vs. Trial 4	-0.3740	-1.068 to 0.3200	No	0.7927	C-D
Trial 3 vs. Trial 5	-0.1838	-0.8778 to 0.5102	No	0.9980	C-E
Trial 3 vs. Trial 6	-0.3770	-1.071 to 0.3170	No	0.7848	C-F
Trial 3 vs. Trial 7	0.1531	-0.5409 to 0.8470	No	0.9995	C-G
Trial 3 vs. Trial 8	0.01987	-0.6741 to 0.7139	No	>0.9999	C-H
Trial 3 vs. Trial 9	0.01964	-0.6743 to 0.7136	No	>0.9999	C-I
Trial 3 vs. Trial 10	0.1390	-0.5550 to 0.8329	No	0.9998	C-J
Trial 4 vs. Trial 5	0.1902	-0.5038 to 0.8842	No	0.9974	D-E
Trial 4 vs. Trial 6	-0.002997	-0.6970 to 0.6910	No	>0.9999	D-F
Trial 4 vs. Trial 7	0.5271	-0.1669 to 1.221	No	0.3237	D-G
Trial 4 vs. Trial 8	0.3939	-0.3001 to 1.088	No	0.7379	D-H
Trial 4 vs. Trial 9	0.3937	-0.3003 to 1.088	No	0.7386	D-I
Trial 4 vs. Trial 10	0.5130	-0.1810 to 1.207	No	0.3636	D-J
Trial 5 vs. Trial 6	-0.1932	-0.8872 to 0.5008	No	0.9970	E-F
Trial 5 vs. Trial 7	0.3368	-0.3571 to 1.031	No	0.8778	E-G
Trial 5 vs. Trial 8	0.2037	-0.4903 to 0.8977	No	0.9956	E-H
Trial 5 vs. Trial 9	0.2034	-0.4905 to 0.8974	No	0.9956	E-I
Trial 5 vs. Trial 10	0.3228	-0.3712 to 1.017	No	0.9034	E-J
Trial 6 vs. Trial 7	0.5301	-0.1639 to 1.224	No	0.3155	F-G
Trial 6 vs. Trial 8	0.3969	-0.2971 to 1.091	No	0.7292	F-H
Trial 6 vs. Trial 9	0.3967	-0.2973 to 1.091	No	0.7299	F-I
Trial 6 vs. Trial 10	0.5160	-0.1780 to 1.210	No	0.3549	F-J
Trial 7 vs. Trial 8	-0.1332	-0.8272 to 0.5608	No	0.9999	G-H
Trial 7 vs. Trial 9	-0.1334	-0.8274 to 0.5606	No	0.9998	G-I
Trial 7 vs. Trial 10	-0.01410	-0.7081 to 0.6799	No	>0.9999	G-J
Trial 8 vs. Trial 9	-0.0002220	-0.6942 to 0.6938	No	>0.9999	H-I
Trial 8 vs. Trial 10	0.1191	-0.5749 to 0.8131	No	>0.9999	H-J
Trial 9 vs. Trial 10	0.1193	-0.5747 to 0.8133	No	>0.9999	I-J

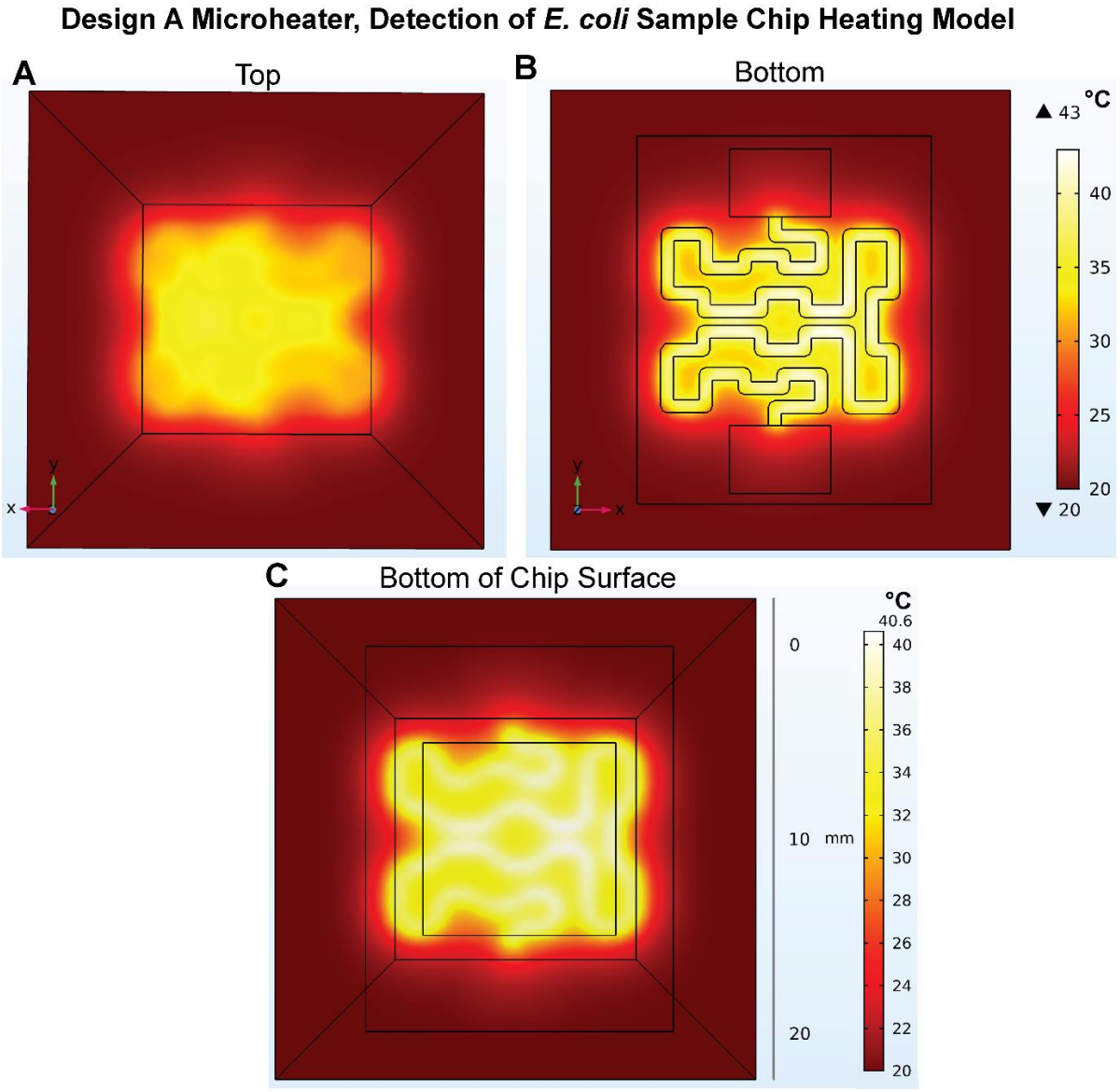

Figure B. 2. COMSOL Model of Design A microheater and *E. coli* sample chip, showing heat distributions for the entire outer surface (A and B), the bottom surface of the sample chip (in contact with the heater) (C). Each figure intensity (color gradient) is specific to the temperature scale to the right of each evaluation, please note that the scales are different for each.

APPENDIX C. SUPPLEMENT TO CHAPTER 4

Table C. 1. Nucleotide sequences of LAMP primers that target the *V. cholerae ctxA* gene.

Primer	Sequence (5' – 3')
B3	GTGGGCACTTCTCAAACT
F3	TCGGGCAGATTCTAGACC
BIP	TCAACCTTTATGATCATGCAAGAGGGGAAACATATCCATCATCGTG
FIP	TTGAGTACCTCGGTCAAAGTACTTCCTGATGAAATAAAGCAGTCA
LB-FITC	/56-FAM/AACTCAGACGGGATTTGTTAGG
LF-Biotin	/5-Biosg/CCTCTTGGCATAAGACCACC

Figure C. 1. Setup for incubations powered by AA battery. Temperature sensors were placed on the top and bottom surfaces of the sample chip and the box was closed after initiation.

Table C. 2. POC heating methods analysis

METHOD	SUITABILITY FOR POC USE	RAMP-UP TIME	TEMP. ACCURACY	POWER SOURCE	MAXIMUM INCUBATION TIME	HEATER COST (USD)	INTERFACE /POWER COSTS	REUSABLE	REF
HOT PLATE	Not suitable	~5 min.	Moderate (± 5 °C)	Electrical Grid	Grid dependent	$287 - $531	N/A	Yes	143
CHEMICAL HEATER	Moderate	5-10 min.	Poor, highly variable	None	19.0 ± 5.0 minutes	$0.41	$1.61 (foam housing)	No	62
PCB	Good	~3 min.	Highly accurate (± 1.5 °C)	Battery /Electrical Grid	Battery/Grid dependent	<$1/cm^2	Accompanying control units vary from simple boards to entire desktop computers.	Yes	144,145
OMEGA POLYIMIDE HEATER	Moderate	Unknown	Unknown	DC Power Source	Grid dependent	$52	$167 DC Power Supply	Yes	146
INKJET PRINTED MICROHEATER	Excellent	5-10 min.	Good (± 2.5 °C from median of desired Temp. window)	Battery or DC Power Source	Battery dependent (30 min. to 16 h)	max <$0.58/heater & even less with roll-to-roll printing	$1.45 for one NiMH AA rechargeable battery	Yes	N/A

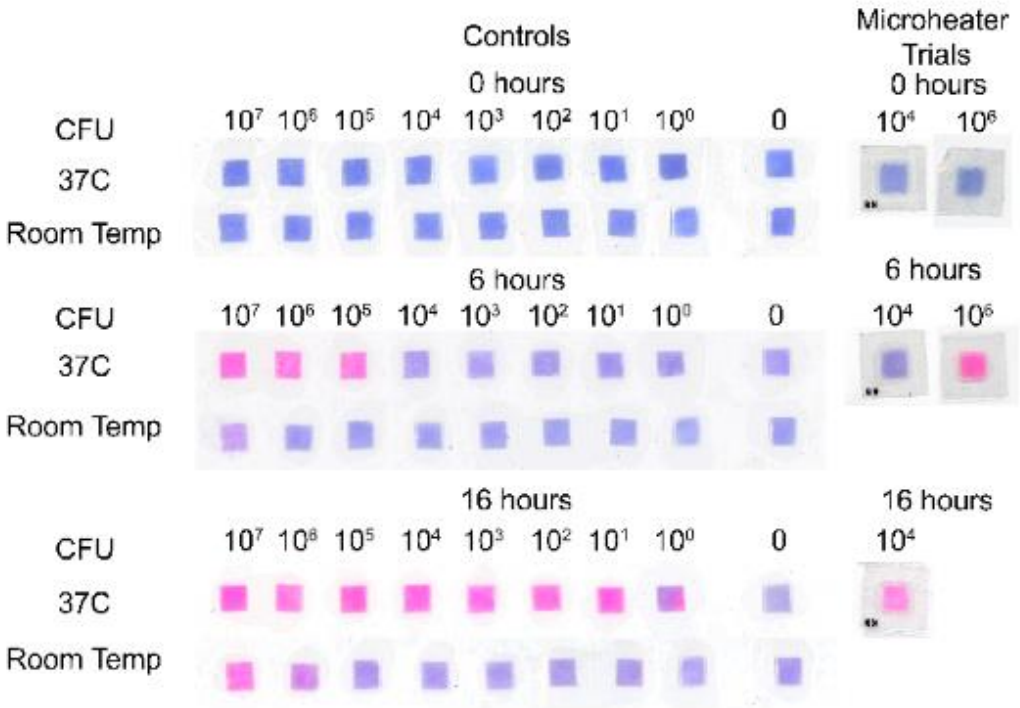

Figure C. 2. Detection of serial dilutions of *E. coli* using PrestoBlue™. LOD of 37°C after 6 hours is 10^5 colony-forming unit (CFU). After 16 hours limit of detection (LOD) of 37°C is 10^1 CFU. LOD of room temperature samples was 10^6 CFU after 16 hours. Design A microheater (8 Ohms) was used for these trials. Color change for microheater incubations closely match incubator results while room temperature samples did not. Incubator and microheater performance data suggest the microheater incubation could have a similarly low LOD of 10^1 CFU.

APPENDIX D. SUPPLEMENT TO CHAPTER 5

One-Dimensional Flow Characterization Results

Flow parameters for conjugated AuNP and DAB in nitrocellulose channels of varying widths were tested in one-dimensional flow studies (Table D.1, below). Further optimization studies were subsequently performed to decide the optimum reagent concentrations and the locations of the fluidic inputs (Table D.3).

$$\mathrm{V} = k\frac{2\cos(\theta)\,(w+h)}{6zC} \qquad (\mathrm{Eq.\,D1})$$

Table D. 1. Characterized LFA components. k refers to the parameter from Eq. 1 and R2 is the coefficient of determination for the fit of Eq. 1 to the data.

Characterized Parameters	**Value**
Nitrocellulose volume capacity	0.1 μL/mm^2
Glass fiber volume capacity	0.63 μL/mm^2
Volume released from glass fiber pad	> 95%
Conjugated 40 nm AuNP in 5 mm nitrocellulose channel	k=230.3, R^2=0.82
Conjugated 40 nm AuNP in 2 mm nitrocellulose channel	k=126.1, R^2=0.71
Conjugated 40 nm AuNP in 1 mm nitrocellulose channel	k=75.16, R^2=0.56
DAB in 5 mm nitrocellulose channel	k=326.4, R^2=0.85
DAB in 2 mm nitrocellulose channel	k=137.2, R^2=0.57
DAB in 1 mm nitrocellulose channel	k=52.76, R^2=0.16

Laser Settings ULS 3.5

Nitrocellulose:

Blue Vector cut Power:4.8% Speed: 24% PPI: 500

Adhesive Backing:

Blue Vector Cut: Power: 35% Speed 100% PPI: 500

Red Vector Cut, Power 70% Speed 100%, PPI:500

APPENDIX E. SUPPLEMENT TO CHAPTER 6

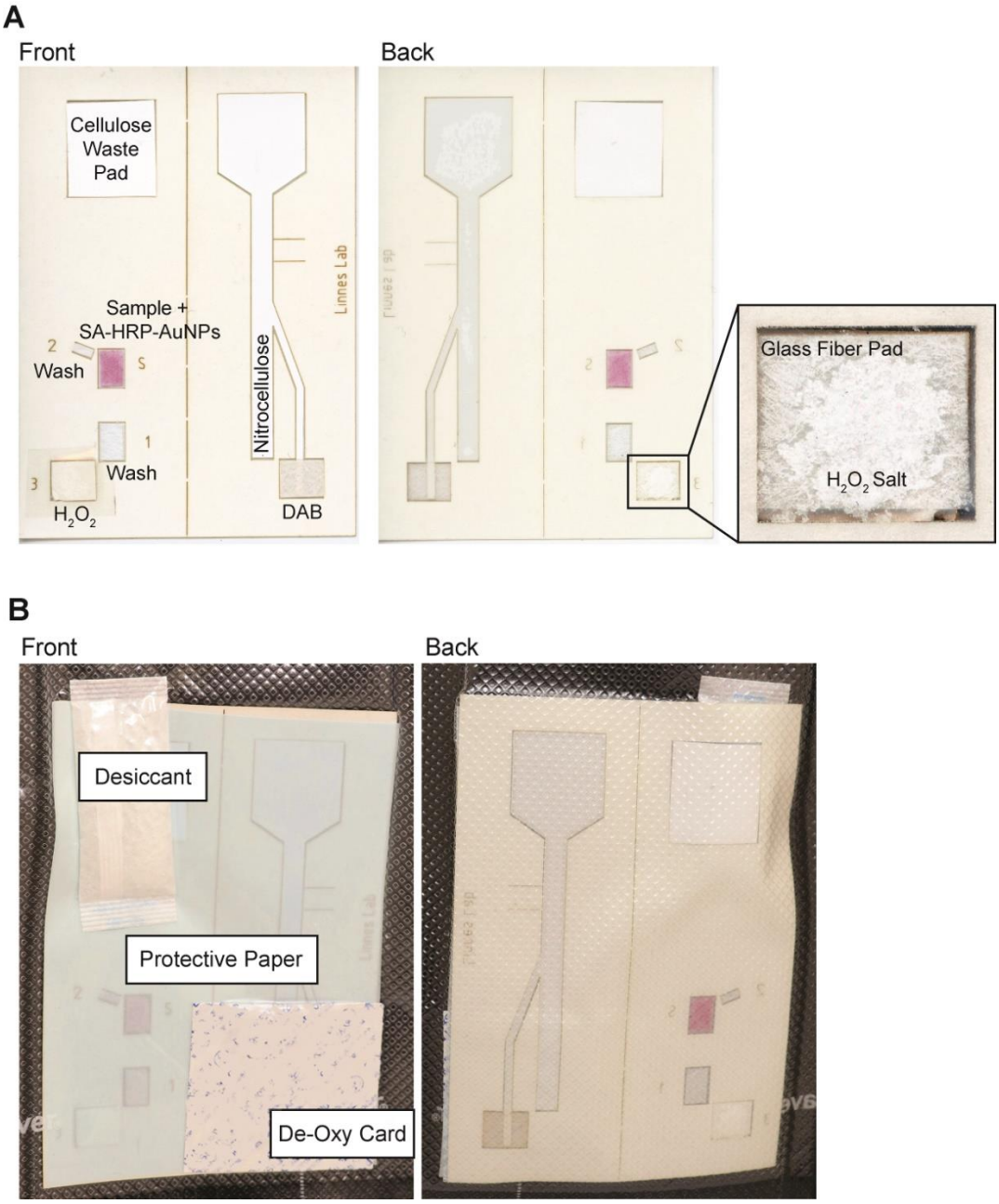

Figure E. 1. Dried 2DPN assembly. (A) Front and back scans of all components on adhesive backing. Enlarged image showing deposit of H2O2 salt on adhesive under glass fiber pad (right). Paper film is removed before use. (B) Front and back images of individually vacuum sealed 2DPN with desiccant, de-oxy card, and blue protective paper for long term storage. Devices were stored away from light.

Template Assisted Rapid Assay (TARA) According to USPTO Utility Patent Application Number 15/068371, CrossLife Technologies Inc.

TARA is a novel chemical transfer reaction that allows template-dependent molecular amplification directly from a biological sample with minimal sample preparation, and the detection of colorimetric signals with the eye on lateral flow paper strips[108]. TARA can rapidly amplify nucleic acid targets directly from blood, urine, saliva or nasopharyngeal swabs without nucleic acid purification without the use of PCR. (Fig. E.2). TARA offers significantly better sensitivity than simple hybridization-based detection because of its ability to repeatedly label one of the probe RNA strands (G probe, Fig. E.2) templated by the same target RNA.

As shown in Fig. E. 2(A), the reporter group (biotin, shown as a blue circle) is transferred from the A probe to the G probe through a thiol exchange reaction depicted in Fig. E. 2(B).[108] This reaction is dependent on the hybridization of the probes to adjacent sequences in the target DNA or the RNA. Importantly, the thiols in the PNA probes will not conjugate with the AuNP in the assay because they are protected with glycans.

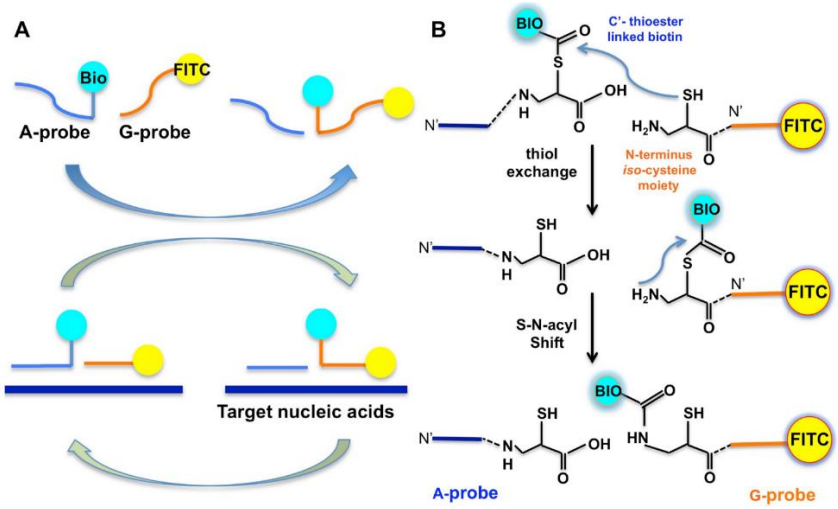

Figure E. 2. Schematic of TARA (A) General principle of TARA. Biotin is transferred from the A probe to the G probe due to a proximity effect. Dynamic turnovers lead to a production of a large number of dual labeled G probes. (B) Detailed chemistry reactions of TARA. [108] Figure reproduced from USPTO Utility Patent Application Number 15/068371 CrossLife Technologies Inc.

TARA Target and Probe Sequences

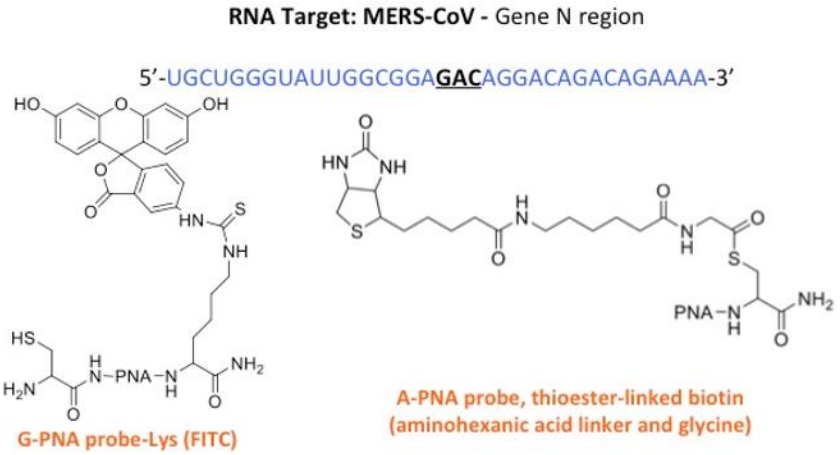

Figure E. 3. MERS-CoV RNA detection. The structure of the PNA A probe and G probe. The transfer reaction system involves two reactive oligonucleotide probes. A 3'-thiolated PNA (A probe) serves as a donor probe and is armed with a thioester-linked reporter group. Both probes were designed to be separated by three nucleotides when hybridized with target RNA.

Model Probes

To test the sensitivity of our 2DPN, we designed model DNA probes that would mimic sample behavior in our device. Samples need a FITC tag in order to bind to the test line, and they require a biotin tag in order to bind the SA-HRP-AuNP and produce a visual signal. ssDNA probes were purchased from IDT. To create a dsDNA sample, we hybridized a probe tagged with FITC, indicated by the IDT sequence label FAM, to a complementary probe labeled with biotin. For an ssDNA sample, we designed a single probe tagged with both FITC and biotin.

Table E. 1. Design of ssDNA sequences for NA model probes

Probe	Sequence
1	5'-/FAM/CTG CAG GTG GTC TTA TGC CAA GAG GAC AGA GTG/3lnvdT/-3'
2	5'-/biotin/CAC TCT GTC CTC TTG GCA TAA GAC CAC CTG CAG -3'
3	5'-/FAM/CTG CAG GTG GTC TTA TGC CAA CAG GAC AGA GTG/biotin/-3'

Images of 5E11 copies/mL ssDNA on 2DPN Replicate Results

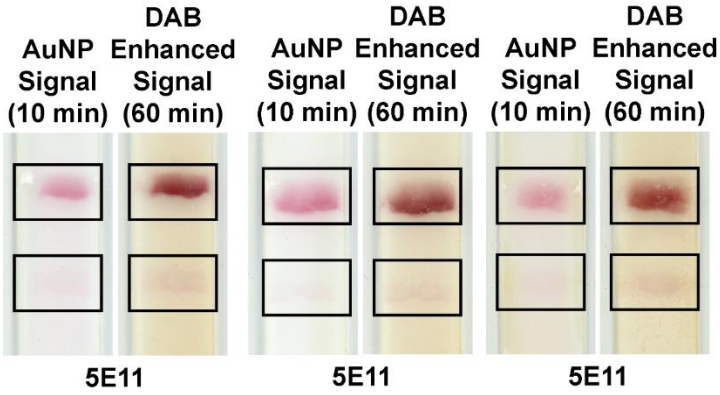

Figure E. 4. Replicates of ssDNA LOD tests at a concentration of 5E11 copies/mL. Detection region of 2DPN imaged at 10 minutes after sample binding (AuNP signal) and at 60 minutes after signal enhancement (DAB enhanced signal).

Images of TARA 2DPN Replicate Results

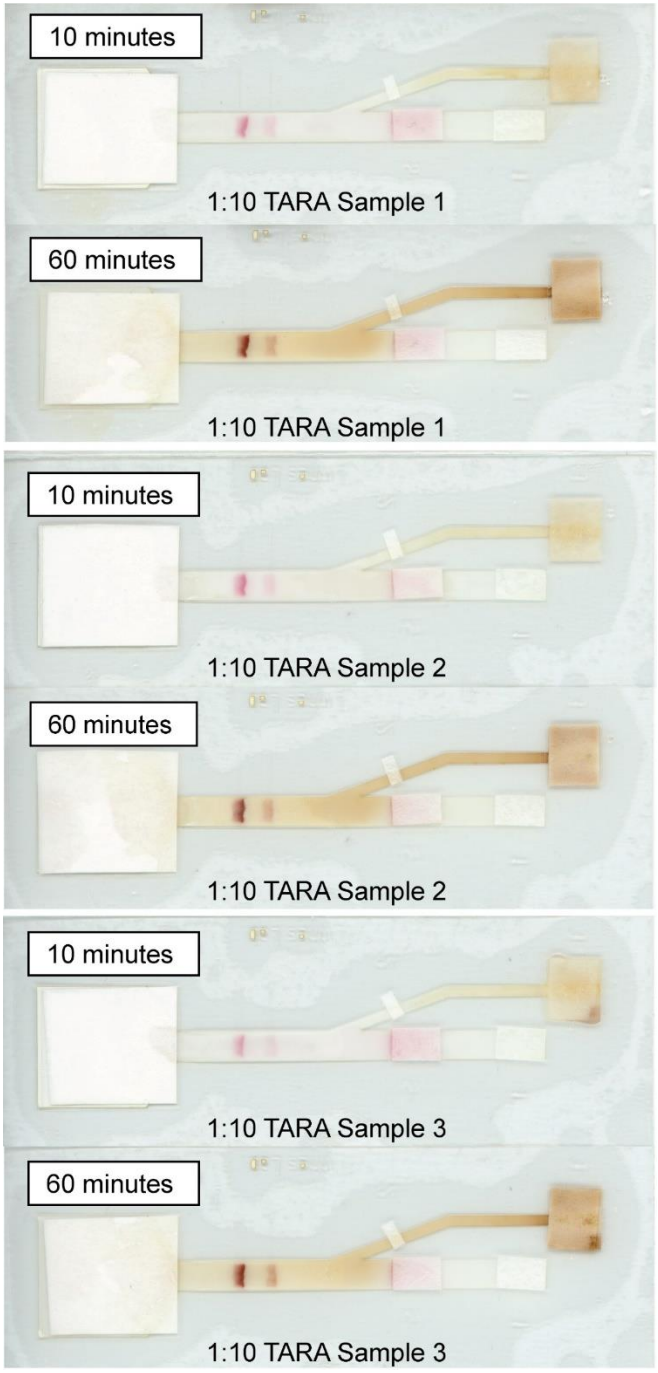

Figure E. 5. Replicates of TARA samples (1:10 dilution in PBST) on dried 2DPN. Imaged at 10 minutes after sample binding (AuNP signal) and at 60 minutes after signal enhancement (DAB enhanced signal).

Percent Increase in Visual Signal Calculations

Signal enhancement solutions have been used in one-dimensional and two-dimensional LFIAs to improve device sensitivity. The improvement in the signal intensity produced by these enhancement solutions is typical quantified as a percent increase or as a fold difference. In order to compare the performance our device to other literature, we calculated the percent difference of the enhanced signal intensity relative to the AuNPs signal intensity, shown below. From this data the average percent difference for all sample concentrations above the LOD (5E11 copies/mL) was 116%.

$$Percent\ Difference\ in\ Signal = \frac{|Average\ AuNP - Average\ DAB|}{Average\ AuNP} \times 100 \qquad (\text{Eq. S2})$$

Table E. 2. ssDNA Probe 3 LOD Percent increase calculations

Sample Concentration (copies/mL ssDNA Probe)	**Average DAB Enhanced Signal (n=3)**	**Average AuNP Signal (n=3)**	**Average % difference**
1E11	0.001	0.005	69
5E11	0.003	0.013	122
1E12	0.068	0.030	124
5E12	0.193	0.096	100

Cost Estimation

Providing easy-to-use diagnostics at an affordable price is crucial for successful translation of the device into clinical use. In academic research, low-cost design specifications are typically assessed by a bill of materials. For example, Richards-Kortum's paper reporting on the development of a paper-based HIV-1 drug resistance detection device included a bill of materials that summed $12.69[128]. However, the academic prototype cost estimation often varies widely from actual commercial prices. While a pregnancy test could be made in a lab from $0.22, commercially available pregnancy tests in the US start at a price of $3.50[129]. Although such a cost analysis does not take into account production costs and factory overhead, the bill of materials does provide some insight on whether or not the devices would be within a feasible cost range in low-income areas. We therefore still found it useful to assess our raw materials cost, although we acknowledge that commercial costs of this device after manufacturing would be higher. We estimate the total material cost of our 2DPN to be approximately $1.82.

Table E. 3. Raw materials cost estimation for 2DPN production

Item	**Cost per device (USD)**
40 nm AuNP	0.06
Streptavidin Poly-HRP	0.22
Biotin conjugated goat anti-rabbit IgG	0.38
FITC polyclonal antibody	0.22
Adhesive Backing	0.13
Nitrocellulose	0.33
Glass fiber sample pads	0.02
DAB and H_2O_2	0.30
Suspension and Blocking Buffers	0.16
Total	*$1.82*

APPENDIX F. SUPPLEMENT TO CHAPTER 7

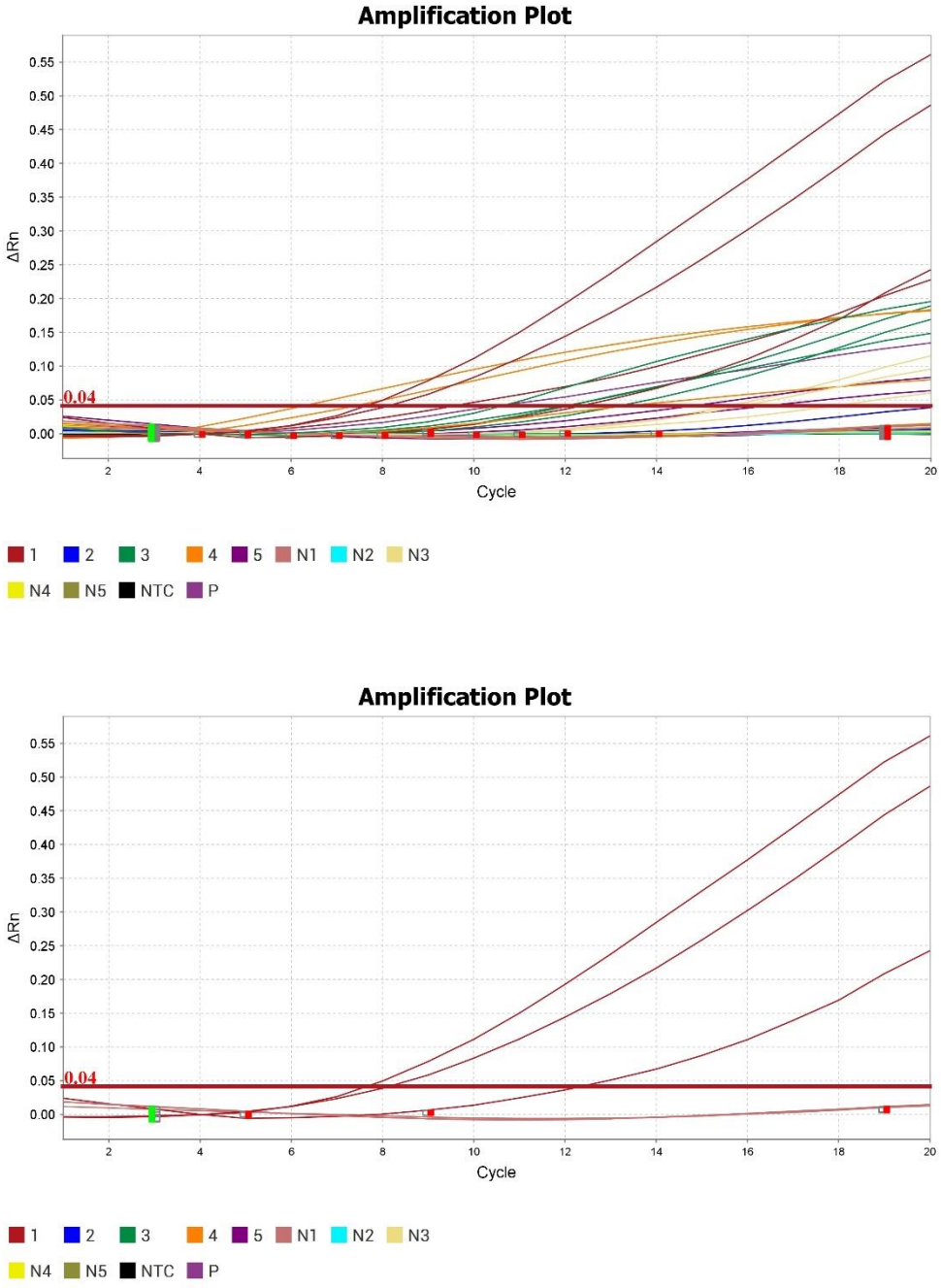

Figure F.1. Performance Analysis of initial primers via Real-Time PCR Machine. Top: All primer sets n=3. Bottom: Primer set 1 F1&R1 showing promising amplification while maintaining a negative for the NTC control.

Table F.1. Primers used in this work.

ID	Type	Sequence	Start	nt	Tm	GC%	Amplicon Length	ΔG complement to Template (kcal/mole)
KB FP1	Forward Primer	/5Biosg/GTTATAACACCAGGAACAAATACTTCTAACC	1789	31	64.2	35.5	109	-51.47
KB RP1	Reverse Primer	/56-FAM/AAGTAGGAGTAAGTTGATCTGCATGAATAG	1897	30	64.6	36.7		-49.02
KB FP2	Forward Primer	/5Biosg/CAAATACTTCTAACCAGGTTGCTGTTCTTTATC	1805	33	66.1	36.4	111	-56.57
KB RP2	Reverse Primer	/56-FAM/CTGTAGAATAAACACGCCAAGTAGGAGTAAG	1915	31	66.2	41.9		-53.24
KB FP3	Forward Primer	/5Biosg/CCATTGGTGCAGGTATATGCGCTAGTTATC	1994	30	60.1	46.7	105	-56.03
KB RP3	Reverse Primer	/56-FAM/CAAGTGACATAGTGTAGGCAATGATGGATTGA	2098	32	68.0	40.6		-55.02
KB FP4	Forward Primer	/5Biosg/TGCTTACTCTAATAACTCTATTGCCATACC	2115	30	56.1	36.7	104	-50.45
KB RP4	Reverse Primer	/56-FAM/TTGTACAATCTACTGATGTCTTGGTCATAG	2218	30	64.5	36.7		-47.34
KB FP5	Forward Primer	/5Biosg/CCACAAATCATTACTACAGACAACACATTT	3334	30	64.8	33.3	105	-49.16
KB RP5	Reverse Primer	/56-FAM/GTCTAATTCAGGTTGCAAAGGATCATAAAC	3438	30	64.8	36.7		-52.17
JQ FP2	Forward Primer	/5Biosg/TCTTGTTTTATTGCCACTAGTCTCTAGTCAGT	21574	32	58.7	37.5	138	- 52.3
JQ FP3	Forward Primer	/5Biosg/CTCTAGTCAGTGTGTTAATCTTACAACCAGAACT	21595	34	59	38.2	117	-53.8
JQ RP1	Reverse Primer	/56-FAM/GAATGTAAAACTGAGGATCTGAAAACTTTG	21711	30	60.	33.3		-50.59
JR FP	Forward Primer	5′-GTTTTCCCAGTCACGAC-C3-AGCTCCAGAAGATAAATTACAGG-3	-	23	52.2	39.1	94	-39.89
JR RP	Reverse Primer	5′-TGTAAAACGACGGCCAGT-C3-GGGGTCATAGTATCCTAGTTG-3	-	21	54.32	47.62		-35.93

Table F.2. Strand Displacement and other Hybridizing Probes (letters in red indicate mismatch locations)

ID	Sequence	Delta G to primer (kcal/mole)	Melt Temp.	GC%	Length	Notes
SD KB FP1	GGT TAG AAG TAT TTG TTC CTG G	-38.21	51 ºC	40.9	22	No amp
SD KB FP1.2	GGT TAG AAG TAT TTG T	-25	38.7 ºC	31.25	16	No amp
SD KB RP1	CTA TTC ATG CAG ATC AAC TTA	-34	47.6 ºC	33	21	No amp
SD KB RP1.2	CTA TTC ATG CAG ATC	-24.25	39.2 ºC	40	15	No amp
JQ SD-FP2.0	ACTGACTAGAGACTA	-20.62	39.7 ºC	40	15	No amp
JQ SD-FP2.1	TCAGACTAGAGACTA	-15.73	39.3 ºC	40	15	Some amp
JQ SD-FP2.2	GCA GAC TAG AGA GTA	-11.82	41.9 ºC	46	15	
JQ SD-FP2.22	GCA GAC TAG AGA GTA/3InvdT/	-11.82	41.9 ºC	46	15	
JQ SD-RP1.0	CAAAGTTTTCAGATC	-24.37	37.3 ºC	33.30%	15	
JQ SD-RP1.1	TATAGTTTTCAGATC	-18.53	33.3 ºC	26.70%	15	
JQ SD-RP1.2	GAGAGTTTTCAGAGC	-15.48	42.7 ºC	46.70%	15	
JQ SD-RP1.2	GAGAGTTTTCAGAGC3InvdT/	-15.48	42.7 ºC	46.70%	15	
JQ FP3.0	AGTTCTGGTTGTAAG	-24.17				
JQ SD-FP3.1	TGATCTGGTTGTAAG	-19.28				

KBFP1-SDFP1 VS KBFP1-SDFP1.2:

ID	Sequence	Delta G: (kcal/mole)	Melt Temp.	GC	Length
KBFP1	/5Biosg/GTTATAACACCAGGAACAAATACTTCTAACC	-51.47	64.2 ºC	35.50%	31
SD-FP1	GGT TAG AAG TAT TTG TTC CTG G	-38.21	51 ºC	40.9%	22
SD-FP1.2	GGT TAG AAG TAT TTG T	-25	38.7 ºC	31.25%	16

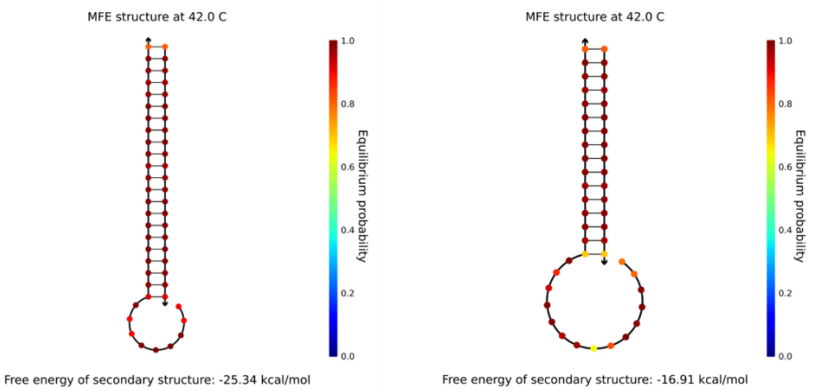

KBRP1-SDRP1 VS KBRP1-SDRP1.2:

ID	Sequence	Delta G: (kcal/mole)	Melt Temp.	GC	Length
KBRP1	/56-FAM/AAGTAGGAGTAAGTTGATCTGCATGAATAG	-49.02	64.6 ºC	36.7%	31
SD-RP1	CTA TTC ATG CAG ATC AAC TTA	-34	47.6 ºc	33%	21
SD-RP1.2	CTA TTC ATG CAG ATC	-24.25	39.2 ºC	40%	15

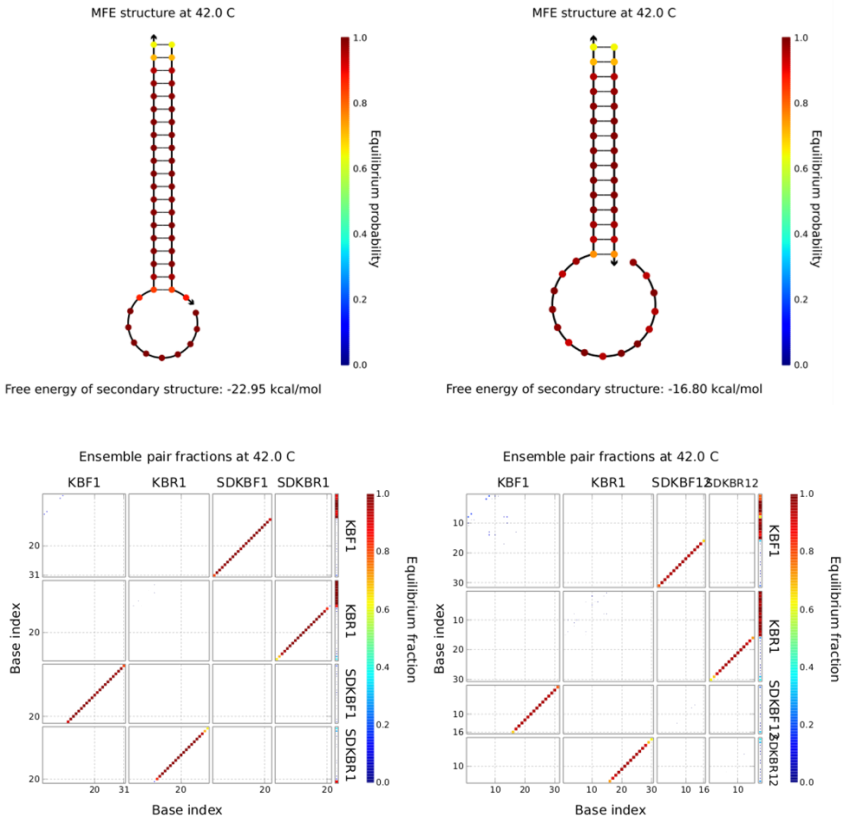

Figure F.2 NUPACK analysis summary of KB primers with SD probes

JQFP2-SDR0 VS JQFP2-SDRP1 VS JQFP2-SDRP1.2:

ID	Sequence	Delta G: (kcal/mole)	Melt Temp.	GC	Length
JQFP2	/5Biosg/TCTTGTTTTATTGCCACTAGTCTCTAGTCAGT	-52.3	58.7 ºC	37.5 %	30
FP2.0	ACTGACTAGAGACTA	-20.62	39.7 ºC	40%	15
SD-FP2.1	TCAGACTAGAGACTA	-15.73	39.3 ºC	40%	15
SD-FP2.2	GCA GAC TAG AGA GTA	-11.82	41.9 ºC	46.7%	15

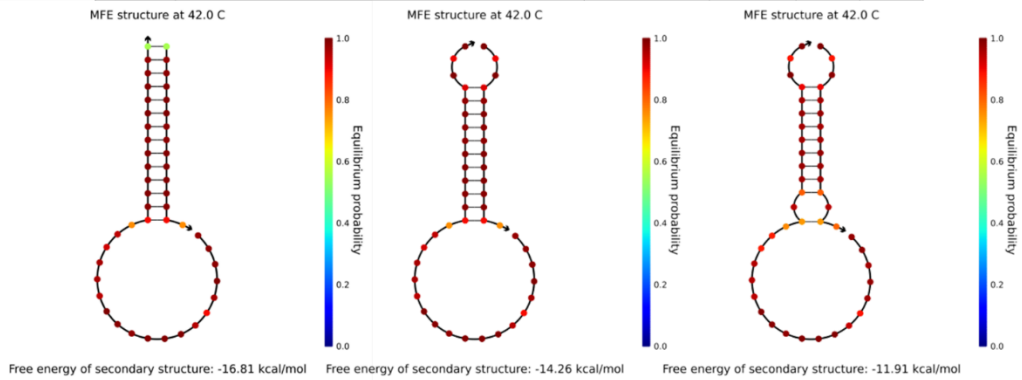

JQRP1-SDR0 VS JQRP1-SDRP1 VS JQRP1-SDRP1.2:

ID	Sequence	Delta G: (kcal/mole)	Melt Temp.	GC	Length
JQRP1	/56-FAM/GAATGTAAAACTGAGGATCTGAAAACTTTG	-50.59	55.1 ºC	33.30%	30
SD-RP1.0	CAAAGTTTTCAGATC	-24.37	37.3 ºC	33.30%	15
SD-RP1	TATAGTTTTCAGATC	-18.53	33.3 ºC	26.70%	15
SD-RP1.2	GAGAGTTTTCAGAGC	-15.48	42.7 ºC	46.70%	15

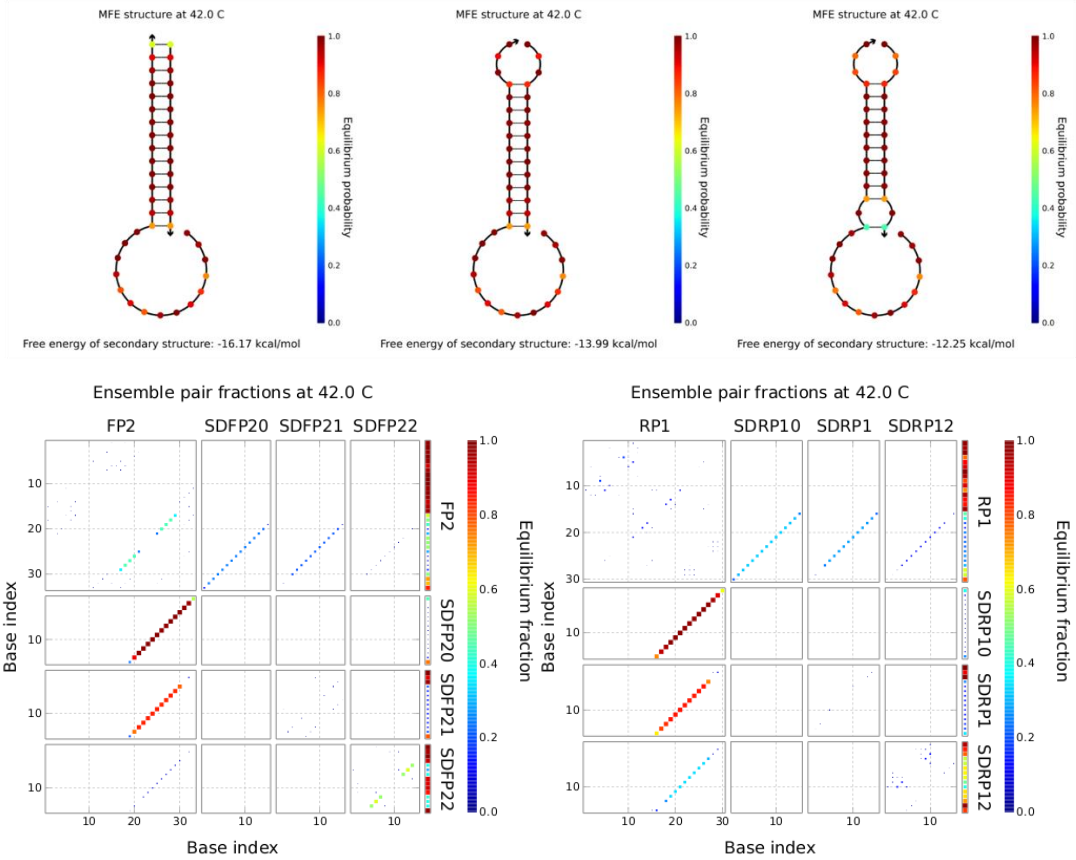

Figure F.3 NUPACK analysis of JQ primers and SD probes

REFERENCES

(1) WHO. *ACCELERATING PROGRESS on HIV, Tuberculosis, Malaria, Hepatitis and Neglected Tropical Diseases*; 2016.

(2) Love-Koh, J.; Griffin, S.; Kataika, E.; Revill, P.; Sibandze, S.; Walker, S. Methods to Promote Equity in Health Resource Allocation in Low- A Nd Middle-Income Countries: An Overview. *Globalization and Health*. BioMed Central Ltd. January 13, 2020, pp 1–12. https://doi.org/10.1186/s12992-019-0537-z.

(3) Dunn, A.; Rittmueller, L.; Whitmire, B. *Introducing the New BEA Health Care Satellite Account*; 2015.

(4) Martinez, A. W.; Phillips, S. T.; Whitesides, G. M.; Carrilho, E. Diagnostics for the Developing World: Microfluidic Paper-Based Analytical Devices. *Anal. Chem.* **2010**, *82* (1), 3–10. https://doi.org/10.1021/ac9013989.

(5) Kost, G. J.; Ferguson, W.; Truong, A. T.; Hoe, J.; Prom, D.; Banpavichit, A.; Kongpila, S. Molecular Detection and Point-of-Care Testing in Ebola Virus Disease and Other Threats: A New Global Public Health Framework to Stop Outbreaks. *Expert Rev. Mol. Diagn.* **2015**, *15* (10), 1245–1259. https://doi.org/10.1586/14737159.2015.1079776.

(6) Arin, K. Drive-Thru Clinics, Drones: Korea's New Weapons in Virus Fight. *The Korea Herald*. 2020.

(7) Rapid Influenza Diagnostic Tests | CDC https://www.cdc.gov/flu/professionals/diagnosis/clinician_guidance_ridt.htm (accessed Jan 30, 2020).

(8) Sperança, M. A.; Suzuki, R. B.; Cabral, A. D.; Carmo, A. M. dos S. Nucleic Acid-Based Diagnosis and Epidemiology of Infectious Diseases. In *Nucleic Acids - From Basic Aspects to Laboratory Tools*; InTech, 2016. https://doi.org/10.5772/61965.

(9) John, A. S.; Price, C. P. Economic Evidence and Point-of-Care Testing. *Clinical Biochemist Reviews*. Australasian Association of Clinical Biochemists 2013, pp 61–74.

(10) MarketsandMarkets. Market Research Report: Point of Care Diagnostics Market by Product (Glucose, Infectious Disease (Hepatitis C, Influenza, Respiratory), Coagulation), Platform (Microfluidics, Immunoassays), Mode (Prescription & OTC), End-User (Hospitals, Home Care) - Glob https://www.marketsandmarkets.com/Market-Reports/point-of-care-diagnostic-market-106829185.html (accessed Feb 25, 2020).

(11) Kosack, C. S.; Page, A. L.; Klatser, P. R. A Guide to Aid the Selection of Diagnostic Tests. *Bull. World Health Organ.* **2017**, *95* (9), 639–645. https://doi.org/10.2471/BLT.16.187468.

(12) Zhang, L.; Gu, C.; Ma, H.; Zhu, L.; Wen, J.; Xu, H.; Liu, H.; Li, L. Portable Glucose Meter: Trends in Techniques and Its Potential Application in Analysis. *Analytical and Bioanalytical Chemistry*. Springer Verlag January 1, 2019, pp 21–36. https://doi.org/10.1007/s00216-018-1361-7.

(13) Wang, Z.; Chen, Z.; Gao, N.; Ren, J.; Qu, X. Transmutation of Personal Glucose Meters into Portable and Highly Sensitive Microbial Pathogen Detection Platform. *Small* **2015**, *11* (37), 4970–4975. https://doi.org/10.1002/smll.201500944.

(14) Mei, Q.; Jing, H.; Li, Y.; Yisibashaer, W.; Chen, J.; Nan Li, B.; Zhang, Y. Smartphone Based Visual and Quantitative Assays on Upconversional Paper Sensor. *Biosens. Bioelectron.* **2016**, *75*, 427–432. https://doi.org/10.1016/j.bios.2015.08.054.

(15) Ramachandran, S.; Fu, E.; Lutz, B.; Yager, P. Long-Term Dry Storage of an Enzyme-Based Reagent System for ELISA in Point-of-Care Devices. *Analyst* **2014**, *139* (6), 1456–1462. https://doi.org/10.1039/C3AN02296J.

(16) Byers, K. M.; Bird, A. R.; Cho, H. D.; Linnes, J. C. Fully Dried Two-Dimensional Paper Network for Enzymatically Enhanced Detection of Nucleic Acid Amplicons. *ACS Omega* **2020**, acsomega.0c00115. https://doi.org/10.1021/acsomega.0c00115.

(17) Akyazi, T.; Basabe-Desmonts, L.; Benito-Lopez, F. Review on Microfluidic Paper-Based Analytical Devices towards Commercialisation. *Analytica Chimica Acta*. Elsevier B.V. February 25, 2018, pp 1–17. https://doi.org/10.1016/j.aca.2017.11.010.

(18) Ignatius, D.; Iii, W. Scalable Manufacturing Methods for Biomedical Microfluidics, Northeastern University Boston, 2016.

(19) Guo, T. W. Expanding Accessibility of Diagnostics through Miniaturized Technologies, Columbia University, 2016.

(20) Real-time COVID-19 testing | Cue https://www.cuehealth.com/what-is-cue/how-cue-detects-covid-19/ (accessed Jul 4, 2021).

(21) Fu, E.; Liang, T.; Spicar-Mihalic, P.; Houghtaling, J.; Ramachandran, S.; Yager, P. Two-Dimensional Paper Network Format That Enables Simple Multistep Assays for Use in Low-Resource Settings in the Context of Malaria Antigen Detection. *Anal. Chem.* **2012**, *84* (10), 4574–4579. https://doi.org/10.1021/ac300689s.

(22) Koczula, K. M.; Gallotta, A. Lateral Flow Assays. *Essays Biochem.* **2016**, *60* (1), 111–120. https://doi.org/10.1042/EBC20150012.

(23) MERS-CoV | Laboratory Testing for MERS-CoV | CDC https://www.cdc.gov/coronavirus/mers/lab/lab-testing.html (accessed Jun 1, 2018).

(24) Corman, V. M.; Albarrak, A. M.; Omrani, A. S.; Albarrak, M. M.; Farah, M. E.; Almasri, M.; Muth, D.; Sieberg, A.; Meyer, B.; Assiri, A. M.; et al. Viral Shedding and Antibody Response in 37 Patients With Middle East Respiratory Syndrome Coronavirus Infection. *Clin. Infect. Dis.* **2015**, civ951. https://doi.org/10.1093/cid/civ951.

(25) World Health Organization. Middle East respiratory syndrome coronavirus (MERS-CoV) https://www.who.int/news-room/fact-sheets/detail/middle-east-respiratory-syndrome-coronavirus-(mers-cov) (accessed Jun 7, 2019).

(26) Wang, Y.-D.; Li, Y.; Xu, G.-B.; Dong, X.-Y.; Yang, X.-A.; Feng, Z.-R.; Tian, C.; Chen, W. F. Detection of Antibodies against SARS-CoV in Serum from SARS-Infected Donors with ELISA and Western Blot. *Clin. Immunol.* **2004**, *113* (2), 145–150. https://doi.org/10.1016/J.CLIM.2004.07.003.

(27) Ko, J.-H.; Müller, M. A.; Seok, H.; Park, G. E.; Lee, J. Y.; Cho, S. Y.; Ha, Y. E.; Baek, J. Y.; Kim, S. H.; Kang, J.-M.; et al. Suggested New Breakpoints of Anti-MERS-CoV Antibody ELISA Titers: Performance Analysis of Serologic Tests. *Eur. J. Clin. Microbiol. Infect. Dis.* **2017**, *36* (11), 2179–2186. https://doi.org/10.1007/s10096-017-3043-3.

(28) Grant, B. D.; Smith, C. A.; Karvonen, K.; Richards-Kortum, R. Highly Sensitive Two-Dimensional Paper Network Incorporating Biotin–Streptavidin for the Detection of Malaria. *Anal. Chem.* **2016**, *88* (5), 2553–2557. https://doi.org/10.1021/acs.analchem.5b03999.

(29) Mahato, K.; Srivastava, A.; Chandra, P. Paper Based Diagnostics for Personalized Health Care: Emerging Technologies and Commercial Aspects. *Biosens. Bioelectron.* **2017**, *96*, 246–259. https://doi.org/10.1016/j.bios.2017.05.001.

(30) Pelton, R. Bioactive Paper Provides a Low-Cost Platform for Diagnostics. *TrAC Trends Anal. Chem.* **2009**, *28* (8), 925–942. https://doi.org/http://dx.doi.org/10.1016/j.trac.2009.05.005.

(31) Fu, E.; Kauffman, P.; Lutz, B.; Yager, P. Chemical Signal Amplification in Two-Dimensional Paper Networks. *Sensors Actuators B Chem.* **2010**, *149* (1), 325–328. https://doi.org/10.1016/j.snb.2010.06.024.

(32) Osborn, J. L. Novel Paper Networks for Point-of-Care Sample Preparation and Indirect IgM Detection. **2011**.

(33) Raphael Wong; Harley Tse. *Lateral Flow Immunoassay*, 1st ed.; Wong, R., Tse, H., Eds.; Humana Press: Totowa, NJ, 2009. https://doi.org/10.1007/978-1-59745-240-3.

(34) Niemz, A.; Ferguson, T. M.; Boyle, D. S. Point-of-Care Nucleic Acid Testing for Infectious Diseases. *Trends Biotechnol.* **2011**, *29* (5), 240–250. https://doi.org/10.1016/j.tibtech.2011.01.007.

(35) Gill, P.; Ghaemi, A. Nucleic Acid Isothermal Amplification Technologies: A Review. *Nucleosides. Nucleotides Nucleic Acids* **2008**, *27* (3), 224–243. https://doi.org/10.1080/15257770701845204.

(36) Notomi, T. Loop-Mediated Isothermal Amplification of DNA. *Nucleic Acids Res.* **2000**, *28* (12), 63e – 63. https://doi.org/10.1093/nar/28.12.e63.

(37) Zanoli, L.; Spoto, G. Isothermal Amplification Methods for the Detection of Nucleic Acids in Microfluidic Devices. *Biosensors* **2012**, *3* (1), 18–43. https://doi.org/10.3390/bios3010018.

(38) Linnes, J. C.; Rodriguez, N. M.; Liu, L.; Klapperich, C. M. Polyethersulfone Improves Isothermal Nucleic Acid Amplification Compared to Current Paper-Based Diagnostics. *Biomed. Microdevices* **2016**, *18* (2), 30. https://doi.org/10.1007/s10544-016-0057-z.

(39) Phillips, E. A.; Moehling, T. J.; Ejendal, K. F. K.; Hoilett, O. S.; Byers, K. M.; Basing, L. A.; Jankowski, L. A.; Bennett, J. B.; Lin, L.-K.; Stanciu, L. A.; et al. Microfluidic Rapid and Autonomous Analytical Device (MicroRAAD) to Detect HIV from Whole Blood Samples. *Lab Chip* **2019**, *19* (20), 3375–3386. https://doi.org/10.1039/C9LC00506D.

(40) Li, J.; Macdonald, J.; Von Stetten, F. Review: A Comprehensive Summary of a Decade Development of the Recombinase Polymerase Amplification. *Analyst* **2019**, *144* (1), 31–67. https://doi.org/10.1039/c8an01621f.

(41) Kunze, A.; Dilcher, M.; Abd El Wahed, A.; Hufert, F.; Niessner, R.; Seidel, M. On-Chip Isothermal Nucleic Acid Amplification on Flow-Based Chemiluminescence Microarray Analysis Platform for the Detection of Viruses and Bacteria. *Anal. Chem.* **2016**, *88* (1), 898–905. https://doi.org/10.1021/acs.analchem.5b03540.

(42) Lobato, I. M.; O'Sullivan, C. K. Recombinase Polymerase Amplification: Basics, Applications and Recent Advances. *TrAC - Trends Anal. Chem.* **2018**, *98*, 19–35. https://doi.org/10.1016/j.trac.2017.10.015.

(43) Kersting, S.; Rausch, V.; Bier, F. F.; Nickisch-rosenegk, M. Von. Rapid Detection of Plasmodium Falciparum with Isothermal Recombinase Polymerase Amplification and Lateral Flow Analysis. *Malar. J.* **2014**, *13* (1), 1–9. https://doi.org/10.1186/1475-2875-13-99.

(44) Macdonald, J.; Von Stetten, F.; Li, J. Review: A Comprehensive Summary of a Decade Development of the Recombinase Polymerase Amplifi Cation Analyst CRITICAL REVIEW Review: A Comprehensive Summary of a Decade Development of the Recombinase Polymerase Amplification. *Analyst* **2018**, *144*, 31. https://doi.org/10.1039/c8an01621f.

(45) Qian, J.; Boswell, S. A.; Chidley, C.; Lu, Z. xiang; Pettit, M. E.; Gaudio, B. L.; Fajnzylber, J. M.; Ingram, R. T.; Ward, R. H.; Li, J. Z.; et al. An Enhanced Isothermal Amplification Assay for Viral Detection. *Nat. Commun.* **2020**, *11* (1), 1–10. https://doi.org/10.1038/s41467-020-19258-y.

(46) Jauset-Rubio, M.; Svobodová, M.; Mairal, T.; McNeil, C.; Keegan, N.; Saeed, A.; Abbas, M. N.; El-Shahawi, M. S.; Bashammakh, A. S.; Alyoubi, A. O.; et al. Ultrasensitive, Rapid and Inexpensive Detection of DNA Using Paper Based Lateral Flow Assay. *Sci. Rep.* **2016**, *6* (1), 37732. https://doi.org/10.1038/srep37732.

(47) Simmel, F. C.; Yurke, B.; Singh, H. R. Principles and Applications of Nucleic Acid Strand Displacement Reactions. *Chem. Rev.* **2019**, acs.chemrev.8b00580. https://doi.org/10.1021/acs.chemrev.8b00580.

(48) Cook, J.; Aydin-Schmidt, B.; González, I. J.; Bell, D.; Edlund, E.; Nassor, M. H.; Msellem, M.; Ali, A.; Abass, A. K.; Mårtensson, A.; et al. Loop-Mediated Isothermal Amplification (LAMP) for Point-of-Care Detection of Asymptomatic Low-Density Malaria Parasite Carriers in Zanzibar. *Malar. J.* **2015**, *14* (1), 43. https://doi.org/10.1186/s12936-015-0573-y.

(49) Lafleur, L. K.; Bishop, J. D.; Heiniger, E. K.; Gallagher, R. P.; Wheeler, M. D.; Kauffman, P.; Zhang, X.; Kline, E. C.; Buser, J. R.; Kumar, S.; et al. A Rapid, Instrument-Free, Sample-to-Result Nucleic Acid Amplification Test. *Lab Chip* **2016**, *16* (19), 3777–3787. https://doi.org/10.1039/C6LC00677A.

(50) Jiang, X.; Loeb, J. C.; Manzanas, C.; Lednicky, J. A.; Fan, Z. H. Valve-Enabled Sample Preparation and RNA Amplification in a Coffee Mug for Zika Virus Detection. *Angew. Chemie Int. Ed.* **2018**, *57* (52), 17211–17214. https://doi.org/10.1002/anie.201809993.

(51) Song, J.; Mauk, M. G.; Hackett, B. A.; Cherry, S.; Bau, H. H.; Liu, C. Instrument-Free Point-of-Care Molecular Detection of Zika Virus. *Anal. Chem.* **2016**, *88* (14), 7289–7294. https://doi.org/10.1021/acs.analchem.6b01632.

(52) Sema, M.; Alemu, A.; Bayih, A. G.; Getie, S.; Getnet, G.; Guelig, D.; Burton, R.; LaBarre, P.; Pillai, D. R. Evaluation of Non-Instrumented Nucleic Acid Amplification by Loop-Mediated Isothermal Amplification (NINA-LAMP) for the Diagnosis of Malaria in Northwest Ethiopia. *Malar. J.* **2015**, *14*, 44. https://doi.org/10.1186/s12936-015-0559-9.

(53) Linnes, J. C.; Fan, A.; Rodriguez, N. M.; Lemieux, B.; Kong, H.; Klapperich, C. M. Paper-Based Molecular Diagnostic for Chlamydia Trachomatis. *RSC Adv.* **2014**, *4* (80), 42245–42251. https://doi.org/10.1039/C4RA07911F.

(54) Packard, M.; Wheeler, E.; Alocilja, E.; Shusteff, M. Performance Evaluation of Fast Microfluidic Thermal Lysis of Bacteria for Diagnostic Sample Preparation. *Diagnostics* **2013**, *3* (1), 105–116. https://doi.org/10.3390/diagnostics3010105.

(55) Phillips, E. A.; Shen, R.; Zhao, S.; Linnes, J. C. Thermally Actuated Wax Valves for Paper-Fluidic Diagnostics. *Lab Chip* **2016**, *16* (21), 4230–4236. https://doi.org/10.1039/C6LC00945J.

(56) Deiss, F.; Funes-Huacca, M. E.; Bal, J.; Tjhung, K. F.; Derda, R. Antimicrobial Susceptibility Assays in Paper-Based Portable Culture Devices. *Lab Chip* **2014**, *14* (1), 167–171. https://doi.org/10.1039/C3LC50887K.

(57) Byrnes, S.; Thiessen, G.; Fu, E. Progress in the Development of Paper-Based Diagnostics for Low-Resource Point-of-Care Settings. *Bioanalysis* **2013**, *5* (22), 2821–2836. https://doi.org/10.4155/bio.13.243.

(58) Chin, C. D.; Chin, S. Y.; Laksanasopin, T.; Sia, S. K. *Point-of-Care Diagnostics on a Chip*; Issadore, D., Westervelt, R. M., Eds.; Biological and Medical Physics, Biomedical Engineering; Springer Berlin Heidelberg: Berlin, Heidelberg, 2013. https://doi.org/10.1007/978-3-642-29268-2.

(59) Southwest Science Incubators http://www.southwestscience.com/Incubators.html (accessed Mar 2, 2019).

(60) Pardy, T.; Rang, T.; Tulp, I. Development of Temperature Control Solutions for Non-Instrumented Nucleic Acid Amplification Tests (NINAAT). *Micromachines* **2017**, *8* (6), 180. https://doi.org/10.3390/mi8060180.

(61) Huang, S.; Do, J.; Mahalanabis, M.; Fan, A.; Zhao, L.; Jepeal, L.; Singh, S. K.; Klapperich, C. M. Low Cost Extraction and Isothermal Amplification of DNA for Infectious Diarrhea Diagnosis. *PLoS One* **2013**, *8* (3), e60059. https://doi.org/10.1371/journal.pone.0060059.

(62) Shah, K. G.; Guelig, D.; Diesburg, S.; Buser, J.; Burton, R.; LaBarre, P.; Richards-Kortum, R.; Weigl, B. Design of a New Type of Compact Chemical Heater for Isothermal Nucleic Acid Amplification. *PLoS One* **2015**, *10* (10), e0139449. https://doi.org/10.1371/journal.pone.0139449.

(63) Wu, J.-T.; Lien-Chung Hsu, S.; Tsai, M.-H.; Liu, Y.-F.; Hwang, W.-S. Direct Ink-Jet Printing of Silver Nitrate–Silver Nanowire Hybrid Inks to Fabricate Silver Conductive Lines. *J. Mater. Chem.* **2012**, *22* (31), 15599. https://doi.org/10.1039/c2jm31761c.

(64) Gasperino, D.; Baughman, T.; Hsieh, H. V.; Bell, D.; Weigl, B. H. Improving Lateral Flow Assay Performance Using Computational Modeling. *Annu. Rev. Anal. Chem.* **2018**, *11* (1), 219–244. https://doi.org/10.1146/annurev-anchem-061417-125737.

(65) Lutz, B. R.; Trinh, P.; Ball, C.; Fu, E.; Yager, P. Two-Dimensional Paper Networks: Programmable Fluidic Disconnects for Multi-Step Processes in Shaped Paper. *Lab Chip* **2011**, *11* (24), 4274. https://doi.org/10.1039/c1lc20758j.

(66) Gosselin, D.; Berthier, J.; Chaussy, D.; Belgacem, N. Capillary Flows: Dynamics and Geometry Effects. **2015**.

(67) *NCoV Genetics*; 2020.

(68) Zhou, P.; Yang, X.-L.; Wang, X.-G.; Hu, B.; Zhang, L.; Zhang, W.; Si, H.-R.; Zhu, Y.; Li, B.; Huang, C.-L.; et al. A Pneumonia Outbreak Associated with a New Coronavirus of Probable Bat Origin. *Nature* **2020**, *579* (7798), 270–273. https://doi.org/10.1038/s41586-020-2012-7.

(69) Kenna, J. G.; Major, G. N.; Williams, R. S. Methods for Reducing Non-Specific Antibody Binding in Enzyme-Linked Immunosorbent Assays. *J. Immunol. Methods* **1985**, *85* (2), 409–419. https://doi.org/10.1016/0022-1759(85)90150-4.

(70) Byers, K. M.; Lin, L.-K.; Moehling, T. J.; Stanciu, L.; Linnes, J. C. Versatile Printed Microheaters to Enable Low-Power Thermal Control in Paper Diagnostics. *Analyst* **2020**. https://doi.org/10.1039/C9AN01546A.

(71) Gosselin, D.; Chaussy, D.; Belgacem, N.; Navarro, F.; Berthier, J. *Transducers Heat Transfer Correlations for Free Convection from Suspended Microheaters*; Toronto, 2016; Vol. 203.

(72) Siegel, A. C.; Phillips, S. T.; Wiley, B. J.; Whitesides, G. M. Thin, Lightweight, Foldable Thermochromic Displays on Paper. *Lab Chip* **2009**, *9* (19), 2775–2781. https://doi.org/10.1039/b905832j.

(73) Botau, A.; Bonfert, D.; Negrea, C.; Svasta, P.; Ionescu, C. Electro-Thermal Analysis of Flexible Micro-Heater. In *2015 38th International Spring Seminar on Electronics Technology (ISSE)*; IEEE, 2015; Vol. 2015-Septe, pp 358–363. https://doi.org/10.1109/ISSE.2015.7248022.

(74) Park, J.; Shin, K.; Lee, C. Roll-to-Roll Coating Technology and Its Applications: A Review. *Int. J. Precis. Eng. Manuf.* **2016**, *17* (4), 537–550. https://doi.org/10.1007/s12541-016-0067-z.

(75) Perelaer, J.; Schubert, U. S. Novel Approaches for Low Temperature Sintering of Inkjet-Printed Inorganic Nanoparticles for Roll-to-Roll (R2R) Applications. *J. Mater. Res.* **2013**, *28* (04), 564–573. https://doi.org/10.1557/jmr.2012.419.

(76) Park, S.-H.; Lee, S.-M.; Ko, E.-H.; Kim, T.-H.; Nah, Y.-C.; Lee, S.-J.; Lee, J. H.; Kim, H.-K. Roll-to-Roll Sputtered ITO/Cu/ITO Multilayer Electrode for Flexible, Transparent Thin Film Heaters and Electrochromic Applications. *Sci. Rep.* **2016**, *6* (1), 33868. https://doi.org/10.1038/srep33868.

(77) Roberson, D. A.; Wicker, R. B.; Murr, L. E.; Church, K.; MacDonald, E.; Roberson, D. A.; Wicker, R. B.; Murr, L. E.; Church, K.; MacDonald, E. Microstructural and Process Characterization of Conductive Traces Printed from Ag Particulate Inks. *Materials (Basel).* **2011**, *4* (6), 963–979. https://doi.org/10.3390/ma4060963.

(78) Cordill, M. J.; Glushko, O.; Kreith, J.; Marx, V. M.; Kirchlechner, C. Measuring Electro-Mechanical Properties of Thin Films on Polymer Substrates. *Microelectron. Eng.* **2015**, *137* (1), 96–100. https://doi.org/10.1016/j.mee.2014.08.002.

(79) Kang, J. S.; Ryu, J.; Kim, H. S.; Hahn, H. T. Sintering of Inkjet-Printed Silver Nanoparticles at Room Temperature Using Intense Pulsed Light. *J. Electron. Mater.* **2011**, *40* (11), 2268–2277. https://doi.org/10.1007/s11664-011-1711-0.

(80) Perelaer, J.; Abbel, R.; Wünscher, S.; Jani, R.; Van Lammeren, T.; Schubert, U. S. Roll-to-Roll Compatible Sintering of Inkjet Printed Features by Photonic and Microwave Exposure: From Non-Conductive Ink to 40% Bulk Silver Conductivity in Less than 15 Seconds. *Adv. Mater.* **2012**, *24* (19), 2620–2625. https://doi.org/10.1002/adma.201104417.

(81) Shen, W.; Zhang, X.; Huang, Q.; Xu, Q.; Song, W. Preparation of Solid Silver Nanoparticles for Inkjet Printed Flexible Electronics with High Conductivity. *Nanoscale* **2014**, *6* (3), 1622–1628. https://doi.org/10.1039/c3nr05479a.

(82) NovaCentrix. Metalon® JS-B40G Conductive Ink Aqueous Dispersion for Dimatix Printheads. 2015.

(83) Saraf, R. F.; Roldan, J. M.; Jagannathan, R.; Sambucetti, C.; Marino, J.; Jahnes, C. Polymer/Metal Composite for Interconnection Technology. In *1995 Proceedings. 45th Electronic Components and Technology Conference*; IEEE; pp 1051–1053. https://doi.org/10.1109/ECTC.1995.517820.

(84) Wang, J.; Duan, H. . L.; Huang, Z. . P.; Karihaloo, B. . L. A Scaling Law for Properties of Nano-Structured Materials. *Proc. R. Soc. A Math. Phys. Eng. Sci.* **2006**, *462* (2069), 1355–1363. https://doi.org/10.1098/rspa.2005.1637.

(85) Jung, S.; Sou, A.; Gili, E.; Sirringhaus, H. Inkjet-Printed Resistors with a Wide Resistance Range for Printed Read-Only Memory Applications. *Org. Electron. physics, Mater. Appl.* **2013**, *14* (3), 699–702. https://doi.org/10.1016/j.orgel.2012.12.034.

(86) Cao, M.; Jochem, K.; Hyun, W. J.; Francis, L. F.; Frisbie, C. D. Self-Aligned Inkjet Printing of Resistors and Low-Pass Resistor–Capacitor Filters on Roll-to-Roll Imprinted Plastics with Resistances Ranging from 10 to 10^{6} Ω. *Flex. Print. Electron.* **2018**, *3* (4), 045003. https://doi.org/10.1088/2058-8585/aaeb6c.

(87) Nguyen, H. A. D.; Shin, K.; Lee, C. Effect of Nip Force on Ink Transfer in High Resolution Roll-to-Roll Printing. *Int. J. Precis. Eng. Manuf.* **2015**, *16* (3), 517–523. https://doi.org/10.1007/s12541-015-0070-9.

(88) Omega Engineering Inc. High Temp Polymide Flexible Heater, 1 in x 1 in https://www.omega.com/en-us/industrial-heaters/surface-heaters/flexible-heaters/p/HTPFH-Series.

(89) Yeh, H. Y.; Shoemaker, C. A.; Klesius, P. H. Evaluation of a Loop-Mediated Isothermal Amplification Method for Rapid Detection of Channel Catfish Ictalurus Punctatus Important Bacterial Pathogen Edwardsiella Ictaluri. *J. Microbiol. Methods* **2005**, *63* (1), 36–44. https://doi.org/10.1016/j.mimet.2005.02.015.

(90) Ma, B.; Fang, J.; Lin, W.; Yu, X.; Sun, C.; Zhang, M. A Simple and Efficient Method for Potential Point-of-Care Diagnosis of Human Papillomavirus Genotypes: Combination of Isothermal Recombinase Polymerase Amplification with Lateral Flow Dipstick and Reverse Dot Blot. *Anal. Bioanal. Chem.* **2019**, *411* (28), 7451–7460. https://doi.org/10.1007/s00216-019-02113-5.

(91) NEB Inc. Can Bst 2.0 DNA Polymerase be used at temperatures other than 65°C? | NEB https://www.neb.com/faqs/2012/08/28/can-bst-2-0-dna-polymerase-be-used-at-temperatures-other-than-65-c (accessed Jul 11, 2019).

(92) How active is Bst 3.0 at other temperatures? | NEB https://www.neb.com/faqs/2015/08/05/how-active-is-bst-3-0-at-other-temperatures (accessed Mar 31, 2021).

(93) Newsham, E. I. CHARACTERIZATION AND DEVELOPMENT OF LATERAL FLOW ASSAYS FOR AUTOMATED MULTI-STEP PROCESSES AND POINT-OF-CARE CERVICAL CANCER DETECTION, Purdue University Graduate School, 2020. https://doi.org/10.25394/PGS.12265043.V1.

(94) Kapton®, D. *DUPONT ™ KAPTON ® HN POLYIMIDE FILM*.

(95) Drain, P. K.; Hyle, E. P.; Noubary, F.; Freedberg, K. A.; Wilson, D.; Bishai, W. R.; Rodriguez, W.; Bassett, I. V. Evaluating Diagnostic Point-of-Care Tests in Resource-Limited Settings. *Lancet Infect. Dis.* **2014**, *14* (3), 239–249. https://doi.org/10.1016/S1473-3099(13)70250-0.

(96) Phillips, E. A. STIMULI-RESPONSIVE VALVING MECHANISMS FOR PAPER-BASED DIAGNOSTICS, Purdue University Graduate School, 2020. https://doi.org/10.25394/PGS.11949231.V1.

(97) Holstein, C. A. Development of a Novel Paper-Based Flu Test for Improved Diagnosis at the Point of Care, University of Washington, 2015.

(98) Candeias, L. P.; Macfarlane, D. P. S.; Mcwhinnie, S. L. W.; Maidwell, N. L.; Roeschlaub, C. A.; Sammes, P. G.; Whittlesey, R. *The Catalysed NADH Reduction of Resazurin to Resorufin*; 1998.

(99) Elavarasan, T.; Chhina, S. K.; Parameswaran (Ash), M.; Sankaran, K. Resazurin Reduction Based Colorimetric Antibiogram in Microfluidic Plastic Chip. *Sensors Actuators B Chem.* **2013**, *176*, 174–180. https://doi.org/10.1016/j.snb.2012.10.011.

(100) Yoo, M. S.; Noh, J. H.; Yoon, B. S.; Reddy, K. E.; Kweon, C. H.; Jung, S. C.; Kang, S. W. Reverse Transcription Loop-Mediated Isothermal Amplification for Sensitive and Rapid Detection of Korean Sacbrood Virus. *J. Virol. Methods* **2012**, *186* (1–2), 147–151. https://doi.org/10.1016/j.jviromet.2012.08.009.

(101) Rolando, J. C.; Jue, E.; Schoepp, N. G.; Ismagilov, R. F. Real-Time, Digital LAMP with Commercial Microfluidic Chips Reveals the Interplay of Efficiency, Speed, and Background Amplification as a Function of Reaction Temperature and Time. *Anal. Chem.* **2019**, *91* (1), 1034–1042. https://doi.org/10.1021/acs.analchem.8b04324.

(102) Linnes, J. C.; Byers, K. M.; Phillips, E. A.; Bird, A. R.; Jamicich, L. M. FLUIDIC CONTROL ELEMENTS FOR SIGNAL READOUT ENHANCEMENT IN TWO-DIMENSIONAL PAPER NETWORKS (2DPN). 15/875,016, 2018.

(103) Rouet, F.; Rouzioux, C. HIV-1 Viral Load Testing Cost in Developing Countries: What's New? *Expert Rev. Mol. Diagn.* **2007**, *7* (6), 703–707. https://doi.org/10.1586/14737159.7.6.703.

(104) Liu, H.; Crooks, R. M. Paper-Based Electrochemical Sensing Platform with Integral Battery and Electrochromic Read-Out. *Anal. Chem.* **2012**, *84* (5), 2528–2532. https://doi.org/10.1021/ac203457h.

(105) Tang, R.; Yang, H.; Gong, Y.; You, M. L.; Liu, Z.; Choi, J. R.; Wen, T.; Qu, Z.; Mei, Q.; Xu, F. A Fully Disposable and Integrated Paper-Based Device for Nucleic Acid Extraction, Amplification and Detection. *Lab Chip* **2017**, *17* (7), 1270–1279. https://doi.org/10.1039/C6LC01586G.

(106) Pardy, T.; Tulp, I.; Kremer, C.; Rang, T.; Stewart, R. Integrated Self-Regulating Resistive Heating for Isothermal Nucleic Acid Amplification Tests (NAAT) in Lab-on-a-Chip (LoC) Devices. *PLoS One* **2017**, *12* (12), e0189968. https://doi.org/10.1371/journal.pone.0189968.

(107) (No Title) https://data.energizer.com/pdfs/nickelmetalhydride_appman.pdf (accessed Nov 7, 2019).

(108) Cho, H.; Kim, C. H. Methods and Compositions of Non-Enzymatic Amplification and Direct Detection of Nucleic Acids. US20160266118A1, September 15, 2016.

(109) UNRUH, T. R.; WOOLLEY, J. B. Molecular Methods in Classical Biological Control. In *Handbook of Biological Control*; Elsevier, 1999; pp 57–85. https://doi.org/10.1016/b978-012257305-7/50051-5.

(110) Delamarche, E.; Bernard, A.; Schmid, H.; Bietsch, A.; Michel, B.; Biebuyck, H. Microfluidic Networks for Chemical Patterning of Substrates: Design and Application to Bioassays. **1998**. https://doi.org/10.1021/ja973071f.

(111) Holstein, C. A. Development of a Novel Paper-Based Flu Test for Improved Diagnosis at the Point of Care. **2015**.

(112) Lateral Flow Membranes | IVD/OEM Materials and Reagents | MilliporeSigma.

(113) Zhdanov, S. .; Starov, V. .; Sobolev, V. .; Velarde, M. . Spreading of Aqueous SDS Solutions over Nitrocellulose Membranes. *J. Colloid Interface Sci.* **2003**, *264* (2), 481–489. https://doi.org/10.1016/S0021-9797(03)00520-4.

(114) Fu, E.; Ramsey, S. A.; Kauffman, P.; Lutz, B.; Yager, P. Transport in Two-Dimensional Paper Networks. *Microfluid. Nanofluidics* **2011**, *10* (1), 29–35. https://doi.org/10.1007/s10404-010-0643-y.

(115) Guo, Y.-R.; Liu, S.-Y.; Gui, W.-J.; Zhu, G.-N. Gold Immunochromatographic Assay for Simultaneous Detection of Carbofuran and Triazophos in Water Samples. *Anal. Biochem.* **2009**, *389* (1), 32–39. https://doi.org/10.1016/J.AB.2009.03.020.

(116) Dharmaraja, S.; Lafleur, L.; Byrnes, S.; Kauffman, P.; Buser, J.; Toley, B.; Fu, E.; Yager, P.; Lutz, B. Programming Paper Networks for Point of Care Diagnostics. In *Microfluidics, Biomems, and Medical Microsystems Xi*; Becker, H., Gray, B. L., Eds.; International Society for Optics and Photonics, 2013; Vol. 8615, p 86150X. https://doi.org/10.1117/12.2006138.

(117) Berthier, J.; Gosselin, D.; Pham, A.; Delapierre, G.; Belgacem, N.; Chaussy, D. Capillary Flow Resistors: Local and Global Resistors. *Langmuir* **2016**, *32* (3), 915–921. https://doi.org/10.1021/acs.langmuir.5b02090.

(118) GE Healthcare Bio-Sciences Corp. Helping You Build a Smarter Diagnostic Assay WhatmanSampleCollection. *29045102 Ab* **2016**, 13.

(119) Ustar Biotechnologies (Hangzhou) Ltd. Disposable Nucleic Acid Detection Device.

(120) Milenia Biotec GmbH. *Universal Lateral Flow Dipstick for the Detection of Biotin-and FITC-Labeled Analytes (Proteins, Genomic Amplificates); REF*; 2019.

(121) Lathwal, S.; Sikes, H. D. Assessment of Colorimetric Amplification Methods in a Paper-Based Immunoassay for Diagnosis of Malaria. *Lab Chip* **2016**, *16* (8), 1374–1382. https://doi.org/10.1039/C6LC00058D.

(122) Jasiński, M.; Miszkiewicz, J.; Feig, M.; Trylska, J. Thermal Stability of Peptide Nucleic Acid Complexes. *J. Phys. Chem. B* **2019**, *123* (39), 8168–8177. https://doi.org/10.1021/acs.jpcb.9b05168.

(123) Phillips, E. A.; Moehling, T. J.; Bhadra, S.; Ellington, A. D.; Linnes, J. C. Strand Displacement Probes Combined with Isothermal Nucleic Acid Amplification for Instrument-Free Detection from Complex Samples. *Anal. Chem.* **2018**, *90* (11), 6580–6586. https://doi.org/10.1021/acs.analchem.8b00269.

(124) Little, J. A. Comparison of Curve Fitting Models for Ligand Binding Assays. https://doi.org/10.1365/s10337-003-0182-8.

(125) Lindsey, C. Y.; Pace-Templeton, J. G.; Millard, C. B.; Wannemacher, R. W.; Hewetson, J. F. Validation of ELISA for the Determination of Anti-Ricin Immunoglobulin G Concentration in Mouse Sera. *Biologicals* **2006**, *34* (1), 33–41.

(126) Rohrman, B. A.; Leautaud, V.; Molyneux, E.; Richards-Kortum, R. R. A Lateral Flow Assay for Quantitative Detection of Amplified HIV-1 RNA. *PLoS One* **2012**, *7* (9), e45611. https://doi.org/10.1371/journal.pone.0045611.

(127) U-Star Disposable Nucleic Acid Lateral Flow Detection Units (pack of 20) https://www.twistdx.co.uk/en/products/product/u-star-disposable-nucleic-acid-detection-device (accessed Jul 25, 2019).

(128) Natoli, M. E.; Rohrman, B. A.; De Santiago, C.; van Zyl, G. U.; Richards-Kortum, R. R. Paper-Based Detection of HIV-1 Drug Resistance Using Isothermal Amplification and an Oligonucleotide Ligation Assay. *Anal. Biochem.* **2018**, *544*, 64–71. https://doi.org/10.1016/j.ab.2017.12.008.

(129) Wilson, D. J.; Kumar, A. A.; Mace, C. R. Overreliance on Cost Reduction as a Featured Element of Sensor Design. *ACS Sensors* **2019**, *4* (5), 1120–1125. https://doi.org/10.1021/acssensors.9b00260.

(130) Foysal, K. H.; Seo, S. E.; Kim, M. J.; Kwon, O. S.; Chong, J. W. Analyte Quantity Detection from Lateral Flow Assay Using a Smartphone. **2019**, *19* (21).

(131) Musilova, I.; Bestvina, T.; Hudeckova, M.; Michalec, I.; Cobo, T.; Jacobsson, B.; Kacerovsky, M. Vaginal Fluid Interleukin-6 Concentrations as a Point-of-Care Test Is of Value in Women with Preterm Prelabor Rupture of Membranes. *Am. J. Obstet. Gynecol.* **2016**, *215* (5), 619.e1-619.e12. https://doi.org/10.1016/J.AJOG.2016.07.001.

(132) Hoorfar, J.; Malorny, B.; Abdulmawjood, A.; Cook, N.; Wagner, M.; Fach, P. Practical Considerations in Design of Internal Amplification Controls for Diagnostic PCR Assays. *J. Clin. Microbiol.* **2004**, *42* (5), 1863. https://doi.org/10.1128/JCM.42.5.1863-1868.2004.

(133) TwistDX. *TwistAmp ® DNA Amplification Kits Assay Design Manual*; 2018.

(134) Wu, H.; Zhao, P.; Yang, X.; Li, J.; Zhang, J.; Zhang, X.; Zeng, Z.; Dong, J.; Gao, S.; Lu, C. A Recombinase Polymerase Amplification and Lateral Flow Strip Combined Method That Detects Salmonella Enterica Serotype Typhimurium With No Worry of Primer-Dependent Artifacts. *Front. Microbiol.* **2020**, *11*, 1015. https://doi.org/10.3389/fmicb.2020.01015.

(135) Jiang, Y. S.; Bhadra, S.; Li, B.; Wu, Y. R.; Milligan, J. N.; Ellington, A. D. Robust Strand Exchange Reactions for the Sequence-Specific, Real-Time Detection of Nucleic Acid Amplicons. *Anal. Chem.* **2015**, *87* (6), 3314–3320. https://doi.org/10.1021/ac504387c.

(136) Londoño, M. A.; Harmon, C. L.; Polston, J. E. Evaluation of Recombinase Polymerase Amplification for Detection of Begomoviruses by Plant Diagnostic Clinics. **2016**. https://doi.org/10.1186/s12985-016-0504-8.

(137) Lillis, L.; Siverson, J.; Lee, A.; Cantera, J.; Parker, M.; Piepenburg, O.; Lehman, D. A.; Boyle, D. S. Factors Influencing Recombinase Polymerase Amplification (RPA) Assay Outcomes at Point of Care. *Mol. Cell. Probes* **2016**, *30* (2), 74–78. https://doi.org/10.1016/j.mcp.2016.01.009.

(138) Akabayov, B.; Akabayov, S. R.; Lee, S. J.; Wagner, G.; Richardson, C. C. Impact of Macromolecular Crowding on DNA Replication. *Nat. Commun.* **2013**, *4* (1), 1–10. https://doi.org/10.1038/ncomms2620.

(139) Sasaki, Y.; Miyoshi, D.; Sugimoto, N. Effect of Molecular Crowding on DNA Polymerase Activity. *Biotechnol. J.* **2006**, *1* (4), 440–446. https://doi.org/10.1002/biot.200500032.

(140) Using OligoAnalyzer Tool to Analyze Hairpins and Dimers | IDT https://www.idtdna.com/pages/support/faqs/how-do-i-use-the-oligoanalyzer-tool-to-analyze-possible-hairpins-and-dimers-formed-by-my-oligo (accessed Jun 30, 2021).

(141) Mann, T.; Humbert, R.; Dorschner, M.; Stamatoyannopoulos, J.; Noble, W. S. A Thermodynamic Approach to PCR Primer Design. *Nucleic Acids Res.* **2009**, *37* (13), e95. https://doi.org/10.1093/nar/gkp443.

(142) Ahn, H.; Batule, B. S.; Seok, Y.; Kim, M.-G. Single-Step Recombinase Polymerase Amplification Assay Based on a Paper Chip for Simultaneous Detection of Multiple Foodborne Pathogens. *Anal. Chem.* **2018**, *90* (17), 10211–10216. https://doi.org/10.1021/ACS.ANALCHEM.8B01309.

(143) Thermo Scientific Cimarec+ Hotplate Series:Incubators, Hot Plates, Baths | Fisher Scientific https://www.fishersci.com/shop/products/cimarec-hotplate-series/p-6367014 (accessed Sep 25, 2019).

(144) Moschou, D.; Tserepi, A. The Lab-on-PCB Approach: Tackling the MTAS Commercial Upscaling Bottleneck. *Lab Chip* **2017**, *17* (8), 1388–1405. https://doi.org/10.1039/C7LC00121E.

(145) Hwang, J.-S.; Kim, J.-D.; Kim, Y.-S.; Song, H.-J.; Park, C.-Y. Performance Evaluation of Optimal Real-Time Polymerase Chain Reaction Achieved with Reduced Voltage. *Biomed. Eng. Online* **2018**, *17* (S2), 156. https://doi.org/10.1186/s12938-018-0579-0.

(146) Polyimide Insulated Flexible Heaters | Omega Engineering https://www.omega.com/en-us/industrial-heaters/flexible-heaters/khra-khlva-kha-series/p/KHLVA-101-5-P (accessed Sep 25, 2019).

PUBLICATIONS

K Byers, A Bird, HD Cho, J Linnes, *Fully Dried 2DPN ELISA for Detection of Amplified Nucleic Acids*, ACS Omega, 2020, DOI: 10.1021/acsomega.0c00115

K Byers, LK Lin, T Moehling, L Stanciu and J Linnes, *Versatile Printed Microheaters to Enable Low-Power Thermal Control in Paper Diagnostics*, Analyst, 2019, DOI: 10.1039/c9an01546a

E Phillips*, T Moehling*, K Ejendal, O Hoilett, **K Byers**, et al. *Microfluidic Rapid and Autonomous Analytical Device (MicroRAAD) to Detect HIV from Whole Blood Samples*. Lab Chip 2019, DIO:10.1039/C9LC00506D. *indicates co-first author

INTELLECTUAL PROPERTY

1. "Temperature Controlled Phase-change Valves for Disposable Nucleic Acid Amplification on Paper" US Patent Application. US20190126270A1. JC Linnes, R Shen[UG], M Chiu[UG], **K Byers**[G], O Hoilett[G], E Phillips[G]. Filed 10/26/2017. Published 05/02/2019

2. "Temperature Controlled Phase-change Valves for Disposable Nucleic Acid Amplification on Paper" PCT Patent Application. WO2017184665A1. JC Linnes, R Shen[UG], M Chiu[UG], **K Byers**[G], O Hoilett[G], E Phillips[G]. Filed 04/19/2017. Published 05/02/2019

3. "Fluidic Control Elements for Signal Readout Enhancement In Two Dimensional Paper Networks" US Patent Application 15/875,016. JC Linnes, LM Jamicich[UG], EA Phillips[G], **KM Byers**[G], AR Bird[UG]. Filed 01/19/18. Published 07/19/2018